

https://dspace.org/

The robustness of spatial modes of light for long distance free-space propagation

Mphuthi, Nokwazi Purity

2020

https://hdl.handle.net/10539/31517

Mphuthi, Nokwazi Purity (2020) The robustness of spatial modes of light for long distance free-space propagation, University of the Witwatersrand, Johannesburg, <http://hdl.handle.net/10539/31517>

Downloaded from a DSpace repository. https://dspace.org/



UNIVERSITY OF THE
WITWATERSRAND,
JOHANNESBURG

Doctoral Thesis

THE ROBUSTNESS OF SPATIAL MODES OF LIGHT FOR LONG DISTANCE FREE-SPACE PROPAGATION

Author:
Nokwazi Purity Mphuthi

Supervisors:
Prof. Andrew Forbes
Dr. Roelf Botha

A thesis submitted to the Faculty of Science, University of the Witwatersrand, Johannesburg, in fulfilment of the requirements for the degree of Doctor of Philosophy

November 2020

Declaration

I declare that this thesis is my own, unaided work. It is being submitted for the Degree of Doctor of Philosophy at the University of the Witwatersrand, Johannesburg. It has not been submitted before for any degree or examination at any other University.



(Signature of candidate)

_____ day of _____ 20 _____ at _____

Abstract

Turbulence remains a major challenge for applications that rely on laser beam transmission through the atmosphere. The properties of laser beams are susceptible to degradation due to variations in the refractive index structure mostly as a result of temperature fluctuations. Spatial fluctuations in the refractive index induce phase distortions, which subsequently modify the propagation of the laser beam through the atmosphere. The modification can be ascribed to three detrimental effects; beam wander, spreading and scintillation. Beam wander causes deflections in the beam's centroid and can result in the beam missing the target. It occurs primarily due to large-scale fluctuations such as atmospheric tip-tilt aberrations. Beam spreading, on the other hand, results from small-scale fluctuations, which causes the beam power to distribute over a large surface area. This spread reduces the intensity and power that is received by optical systems. Finally, scintillation causes temporal and spatial fluctuations in the beam's intensity. It is therefore imperative to constantly look for ways to optimize the performance of beams as they traverse through inhomogeneous media.

In this work, we investigate the feasibility of using spatial modes of light as alternative optical beam sources for use in long distance laser propagation applications. We exploit novel properties of various spatial mode sets such as Hermite-Gaussian, Laguerre-Gaussian and Bessel-Gaussian modes to determine the robustness of each mode in improving the performance of free-space laser propagation systems. We show that Hermite-Gaussian modes are more resilient to lateral displacements such as tip/tilt aberrations in optical systems when compared to modes carrying orbital angular momentum due to their Cartesian symmetry. It is also shown that over a normal distribution of lateral displacements, the Hermite-Gaussian modes experience less mode-crosstalk and less mode-dependent losses.

We also study the self-healing behaviour of Bessel beams by propagating them through aberrated obstacles and show that the self-healing is not guaranteed, but rather a function of the severity of the aberration. The modes are then passed through laboratory simulated turbulence determined by combination of appropriately weighted Zernike aberrations to show that the modes are not resilient to such perturbations as previously claimed. Finally, we develop a real-world turbulence link and propagate modified Bessel beams which preserve the Bessel structure for much longer distance compared to the traditional Bessel beams. These modes show comparable performance to Gaussian modes with the added benefit of self-healing associated with Bessel beams. From this research, we can deduce that various properties of spatial modes can be meticulously tailored to mitigate some of the detrimental effects associated with laser beam transmission through

turbulence. This can pave way for efficient transmission to much longer distances which remain challenging to this day such as ranging to satellites and the Moon.

Acknowledgements

I wish to express my sincere gratitude and appreciation to everyone who assisted and supported me throughout my PhD journey. Specifically, I would like to thank the following people:

My supervisor, Prof. Andrew Forbes - Thank you for the effort and time you dedicated into mentoring me. Your stern approach of conducting research has made me a better researcher who is less afraid of tackling new challenges. Thank you for the constant motivation and pushing me to the best that I can be.

My co-supervisor, Dr. Roelf Botha - You have always believed in me even when I did not believe in myself. I am truly grateful of all the academic, financial and moral support you have always given me.

To my fellow colleagues at the Structured light laboratory - Thank you for all your help in the laboratory and taking time out of your busy work schedules to assist me whenever I needed help. I am also grateful for the social interactions we had outside of the laboratory which made my PhD journey more enjoyable.

Finally,to my husband, Siphiwe Mphuthi, thank you for your patience and understanding throughout this journey. I truly appreciate the support and encouragement you have given me.

Contents

Declaration i

Abstract ii

Acknowledgements iv

Contents v

List of Figures vii

List of Tables x

List of Publications xi

1 Introduction 1
- 1.1 Background and Motivation . . . 1
- 1.2 Outline . . . 4

2 Spatial modes of light 6
- 2.1 Introduction . . . 6
- 2.2 Hermite-Gaussian modes . . . 7
- 2.3 Laguerre-Gaussian modes . . . 8
- 2.4 Bessel-Gaussian modes . . . 8
- 2.5 Creation and detection of spatial modes . . . 10
  - 2.5.1 Digital holography . . . 10
  - 2.5.2 Hologram generation . . . 11
  - 2.5.3 Mode characterisation by modal decomposition . . . 13
- 2.6 Conclusion . . . 15

3 Laser beam propagation through atmospheric turbulence 16
- 3.1 Introduction . . . 16
- 3.2 Atmospheric effects of turbulence . . . 16
  - 3.2.1 Beam spreading . . . 17
  - 3.2.2 Beam wander . . . 18
  - 3.2.3 Scintillation . . . 18
- 3.3 Simulating turbulence in the laboratory . . . 19
- 3.4 Real-world turbulence . . . 24

3.5 Conclusion 26

4 The resilience of orbital angular momentum and Hermite–Gaussian modes to tip/tilt aberrations 28
4.1 Introduction 28
4.2 Theoretical concept 29
4.3 Experimental implementation 32
4.3.1 Experimental setup 32
4.3.2 Results and discussion 32
4.4 Conclusion 36

5 Investigating the self-healing of Bessel beams through aberrations and turbulence 37
5.1 Introduction 37
5.2 Theory 38
5.2.1 Self-healing property of Bessel beams 38
5.3 Experimental implementation 40
5.3.1 Experimental setup 40
5.3.2 Aberration results 42
5.3.3 Turbulence results 46
5.4 Discussion 46
5.5 Conclusion 48

6 Propagation of shape-invariant Bessel beams through real world turbulence 49
6.1 Introduction 49
6.2 Shape-invariant Bessel beams 50
6.3 Experimental implementation 52
6.3.1 Experimental setup 52
6.3.2 Link Characterisation 53
6.3.3 Crosstalk Results 57
6.4 Discussion and Conclusion 59

7 Conclusion 61

Bibliography 64

List of Figures

2.1 Intensity patterns with inset phase of Laguerre-Gaussian, Hermite-Gaussian and Bessel-Gaussian modes of various orders. The first row depicts LG (ℓ, p) modes, the second row depicts HG (m, n) modes and the third row depicts BG (ℓ). 9

2.2 The formation of Bessel beams by superposition of plane waves propagating on a cone. 10

2.3 Examples of holograms generated by a) phase-only and b) complex amplitude modulation. The first column generates $HG_{2,2}$, second column $LG_{2,2}$ and third column BG_2. 13

3.1 Random phase screens of varying turbulence strength represented by Strehl ratio. Rows from top to bottom are for the inverse power spectrum approach (a), the sub-harmonic method (b) and the Noll (Zernike) method (c). The last row illustrates the individual Zernike phase screens which make up the Noll method with indices ranging from $j = 1$ to $j = 6$ (d), although in reality up to 60 screens are required for a physically accurate result. 21

3.2 (a) Typical set-up for creating a mode and then aberrating it with turbulence (FL: Fourier Lens; SLM: Spatial Light Modulator). (b) Holograms for strong (top, SLM) and weak (bottom, DMD) turbulence with (right) and without (left) gratings. (c) Phase (left) and intensity (right) of $\ell = 3$ beams through the setup with the turbulence to the left. 22

3.3 Experimental measurement of Strehl Ratio using turbulence screens generated using the spectrum inversion (FT) and Zernike (Noll) methods showing a close match to theory. 24

4.1 Intensities ($|HG_{m,n}|^2$) and phase profiles (arg$[HG_{m,n}]$) of (a) $LG_{0,-2}$, $LG_{0,-1}$, $LG_{0,+1}$, $LG_{0,+2}$ (b) $HG_{2,0}$, $HG_{1,0}$, $HG_{0,1}$ and $HG_{0,2}$. 30

4.2 (a) Schematic illustration of lateral displacement along x-direction of phase profile of $HG_{1,0}$ (b) Schematic illustration of lateral displacement along x-direction of phase profile of $LG_{0,+1}$ (c) Schematic illustration of emulation of lateral displacement of reference frame of CGH at Rx. Lateral displacement along HG modes' axes of symmetry modes are indicated by white arrows. 31

4.3 Experimental setup as described in the text. A collimated green laser source was expanded and illuminated on half of the SLM (Tx) to generate the HG and LG modes. A 4 f imaging system is then used to image the generated modes to the other half of the SLM (Rx) to allow detection measurements. 33

4.4 (a) Experimentally measured mode-dependent loss of HG_{10} and HG_{01} and, $LG_{0,-1}$ and $LG_{0,+1}$ as a function of lateral displacement along the x-direction (X-offset) in units of waist size (ω) (b) Experimentally measured mode-crosstalk between HG_{10} and HG_{01} and, between $LG_{0,-1}$ and $LG_{0,+1}$ as a function of lateral displacement along the x-direction (X-offset) in units of waist size (ω). 34

4.5 (a) Random lateral displacements of OAM and HG modes as denoted by blue points. Sizes of OAM and HG modes denoted by green circle (b) Experimentally measured mode-dependent loss (c) Experimentally measured mode-crosstalk averaged over 50 random lateral displacements for each pair of spatial modes as a function of σ. 35

5.1 Self-healing principle of Bessel-Gaussian (BG) beams. Plane waves incident on an axicon of apex angle α are refracted to form conical waves which interfere to form a BG beam in the region $z_{\max}$. An opaque obstruction placed at $\frac{1}{2}z_{\max}$ blocks the waves while allowing unblocked waves to interfere at a short distance behind the obstruction, i.e., after $z_{\min}$. The inset depicts the theoretical profiles (a-e) of the beam at different distances before and after the obstruction together with corresponding experimental images (d-h). The images a and e illustrates the beam just after formation while images b and f illustrates the beam at the obstruction region. The region immediately after the obstruction is illustrated by images c and g while the self-healing region is illustrated by images e and f. The plane z_0 is the region where the beam is expected to self-heal completely. 39

5.2 (a) Schematic of the experimental setup used to study the self-healing of BG beams after encountering a phase-changing obstruction. A collimated Argon-ion laser source is used to generate a BG from an axicon encoded on one half of the SLM screen (labelled as 1) while the second half (labelled as 2) was encoded with the obstruction. The distance between SLM1 and SLM2 was $\frac{1}{2}z_{max}$, thereby placing the obstruction in the middle of z_{max}. (b) A conceptual illustration of the core optical planes, showing the position of the two phase screens of the SLM. 41

5.3 Theoretical and experimental images depicting the evolution of the BG beam after encountering different aberrations.The columns (a-g) represent different obstructions while the rows represent different observation planes within zmax. Column (a) depicts the reference case of an opaque disk obstruction, while columns (b,c,d,e,f and g) depict tilt, defocus, astigmatism, coma, trefoil and spherical aberrations with a magnitude coefficient of unity ($a_{n,m} = 1$) respectively. Rows 1 (theoretical) and 2 (experimental) illustrates the influence of the obstruction at the shadow region(zmin),while row 3 (theoretical) and 4 (experimental) illustrates how the beam has evolved at the self-healing region(z_0). 42

5.4 Correlation of the perturbed beam against a reference unperturbed beam at the plane $z = z_0$, plotted as a function of aberration strength, for odd and even aberrations as well as aberrations with no azimuthal dependence(ie m=0). 43

5.5 Relationship between beam energy and aberration strength. The measurements are shown for astigmatism, trefoil and spherical aberrations for the same aberration strengths as Figure. 5.4. It is clear that energy decreases with an increase in aberration strength for all the displayed aberrations. The dotted lines are estimated based on a least-squared fit on the measurements. 44
5.6 Theoretical and experimental(insets) images of Bessel beams at the self-healing plane after encountering trefoil of magnitude, $a_{3,3}$, of (a) 1, (b) 5, (c) 10 and (d) 20. The circles indicate the region of the beam visible to the detector. self-healing is seen to improve with increasing aberration strength around the centre of the beam. 45
5.7 Experimental images of the BG beams after encountering turbulence. (a) - (c) shows the BG beam immediately behind the turbulence screen while (d) - (f) shows the BG beam at $z = z_0$. In all plots the turbulence increases from left to right with D/r_0 values of 3, 10 and 20. 46

6.1 Holograms for generating zero and high-order shape-invariant Bessel beams with their respective intensity profiles at the near and far-field planes. . . 52
6.2 Experimental setup of the 150 m free-space link used to generate and measure shape-invariant Bessel beams. a) An expanded HeNe laser source illuminates an SLM encoded with a phase-only element to generate the beam. The beam is propagated through real turbulence, reflected off a retro-reflector back to a measuring SLM encoded with de-multiplexing holograms. The intensity profile of the beam before it leaves and when it returns are depicted in b) and c) respectively. 54
6.3 Strehl ratio at different times of the day. The turbulence strength is strongest at midday, and this is where the image quality is mostly deteriorated. Rainy weather conditions further degrade the image quality when compared to non-rainy weather. 56
6.4 Experimental results showing inter-modal crosstalk. Shape-invariant BB modes (a) are compared with Gaussian modes (b) under difference turbulence conditions(depicted as rows). (c) illustrates the normalized power spectrum for mode $l = 2$. The turbulence strength during the day and night was estimated to be 3.21×10^{-14} $\mathrm{m}^{-2/3}$ and 1.35×10^{-13} $\mathrm{m}^{-2/3}$ respectively. 58
6.5 Power spectrum for radial modes of different cone angles. The mode at the centre of the spectrum represents the mode with a cone angle corresponding to a measurement distance of $z = 210$ cm. 59

List of Tables

6.1 Solutions for calculating particular cone angles for given n and m values. The cone angles are dependent on the propagation distance z and element parameters a and r_1. 51
6.2 Free-space link parameters. 57

List of Publications

Peer-reviewed journals:

1. Cox, M.A., **Mphuthi, N.**, Nape, I., Mashaba, N.P., Cheng, L. and Forbes, A., 2020. Structured Light in Turbulence. arXiv:2005.14586.

2. **Mphuthi, N.**, Gailele, L., Litvin, I., Dudley, A., Botha, R. and Forbes, A., 2019. Free-space optical communication link with shape-invariant orbital angular momentum Bessel beams. Applied Optics, 58(16), pp.4258-4264.

3. **Mphuthi, N.**, Botha, R. and Forbes, A., 2018. Are Bessel beams resilient to aberrations and turbulence?. JOSA A, 35(6), pp.1021-1027.

4. Ndagano, B.,**Mphuthi, N.**, Milione, G. and Forbes, A., 2017. Comparing mode-crosstalk and mode-dependent loss of laterally displaced orbital angular momentum and Hermite–Gaussian modes for free-space optical communication. Optics Letters, 42(20), pp.4175-4178.

Conference Proceedings:

1. **Mphuthi, N.** and Forbes, A., 2019, September. Bessel beams through turbulence. In Laser Science (pp. JTu3A-33). Optical Society of America..

2. Milione, G., Ndagano, B., **Mphuthi, N.** and Forbes, A., 2018. Using Hermite-Gaussian Modes for Free-Space Optical Communication. In Complex Light and Optical Forces XII (Vol. 10549, p. 105490C). International Society for Optics and Photonics.

3. Milione, G., Ndagano, B., **Mphuthi, N.** and Forbes, A., 2018, March. Using Hermite-Gaussian modes for free-space optical communication (Conference Presentation). In Complex Light and Optical Forces XII (Vol. 10549, p. 105490C). International Society for Optics and Photonics.

Chapter 1

Introduction

1.1 Background and Motivation

The last five decades has seen coherent propagation of light beams to remarkable distances ranging from a few kilometres to approximately 400 000 km to the surface of the Moon. Although common in military applications, long range laser propagation has found useful applications for civilian uses such as geodesy, remote sensing and optical communications. In optical communications, free-space optics technology has gained popularity due to its tremendous speed, high security and cost effectiveness when compared to radio frequency and optical fibre technology [1–6]. This has seen a significant increase in the much-needed data capacity and bandwidth in modern telecommunication systems. This is a line of sight technique used to transmit information from one point to another using a narrow optical beam. Free-Space Optics (FSO) links, which can range from inter-building to inter-satellite distances, can transmit data, voice and video communications through air at rates of up to 2.5 Gbps [7]. A technique somewhat similar to this is laser ranging, which measures the round-trip travel time of short pulses sent from terrestrial telescopes to the retro-reflectors on satellites [8] or the surface of the Moon [9] to accurately estimate distance within millimetre accuracy. The obtained range data has provided insight towards a myriad of scientific research areas such as gravitational and planetary physics [10–16], lunar science [17–19], geodynamics [20, 21], terrestrial and celestial reference frames [22, 23] as well as astronomy [24].

The performance of these techniques is limited by atmospheric effects through which the laser is transmitted. In optical communication links, absorption and scattering of large weather particles such as clouds, rain and fog substantially attenuates the laser beam thereby reducing the received signal power [25–32]. This effect is known as fading and usually occurs when the optical signal falls below the sensitivity of the receiver.

Studies have shown that weather related attenuation may be as high as 300 dB/km [26]. Furthermore, FSO links are also severely affected by atmospheric turbulence [33]. Variations in the refractive index of air induce distortions in the transmitted signal in the form of scintillation, beam wander and spreading. Scintillation results in fluctuations in the beam's intensity which reduce the bit error rate of the system while the beam wander will result in a deflection of the optical beam from a straight-line trajectory, thereby missing the receiver plane altogether. Beam spreading, on the other hand, occurs when the optical beam spreads beyond vacuum diffraction, thereby losing focus and reducing the transmitted power density. All these effects severely impair the quality of the link resulting in the loss of information.

The effects of spreading are more severe for long-haul applications such as satellite communication systems and laser ranging. Since the signal strength of the received pulse depends on the inverse fourth power of the distance, Lunar laser ranging remains the most challenging due to the overall signal loss as a result of the large distance between the Earth and the Moon. As a result, only five stations in the world have been successful in ranging to the Moon. These stations are located in Texas, USA [34], Grasse, France [35], Hawaii, USA [36], Matera, Italy [37] and New Mexico, USA [38]. All the stations are located in the Northern Hemisphere leading to a weak geometry of the network. The major limiting factor of LLR stems from poor detection rates, mostly due to divergence on both the outgoing and return pulse. The outgoing pulse, even for perfectly collimated systems, is limited by atmospheric turbulence which can cause beam wandering and spreading of between one to few arcseconds at best. A divergence of 1 arcsecond or 5 μrad, for instance, translates to about 2 km on the surface of the Moon, illuminating corner cubes retro-reflectors which have a diameter of about 3.8 cm. This translates into a one-in-25-million chance of a photon launched from Earth hitting the retro-reflectors. The return journey is even more challenging since the retro-reflectors are not diffraction-limited and are subject to velocity aberrations caused by the relative motion of the Earth with respect to the Earth [39]. This result in a divergence of approximately 10 arcseconds, which translates to about 20 km on the surface of the Earth, received by a collecting telescope of a few metres in diameter. This means that a 1 m telescope on Earth can collect approximately 10^{-9} of the returning photons on the reflector at a wavelength of 532 nm. In addition to this is the challenge of pointing and steering the telescope, which is expected to acquire sub-arcsecond precision to the Moon. All these factors together with the optical performance of the system and the detector efficiencies affect the accuracy of the laser ranging technique.

To improve the performance of these systems, one would have to mitigate the effects of turbulence. This can be done by increasing the laser shoot rate in the case of laser ranging, using adaptive optics to compensate for turbulence effects or changing the laser

wavelength to improve the quantum efficiency of the return detector. While the green wavelength (λ = 532 nm has been used as the standard wavelength for atmospheric transmission, recent experiments have demonstrated that there might be benefits in using infrared wavelength due to better transmission through atmospheric turbulence and improved signal to noise ratio [40]. In addition, one study suggested that the use of 1550 nm wavelength is more beneficial for FSO communications than the 785 nm wavelength under severe weather conditions [28]. It was also demonstrated in [41] that more quality observations were taken using IR than green laser for ranging. IR laser sources can improve the rate of detection especially during new and full Moon when temperature gradients affect the refractive index of the corner cube retroreflectors, thereby leading to wavefront distortions.

Most FSO links use Gaussian beams to transfer information by collecting light in 'buckets' with no spatial mode discrimination while other information is encoded through modulation schemes such as on/off keying, phase modulation and so on. In contrast to this, channel capacity can be further increased by exploiting different properties of light such as polarisation [42–46], wavelength [47–50] and spatial phase [51–54]. These properties serve as independent data channels through which information can be encoded, greatly increasing the capacity to up to terabit levels [55]. Polarisation and wavelength are robust in air because the atmosphere in neither birefringent nor nonlinear and therefore cannot influence them directly. Spatial phase on the other hand is directly affected by atmospheric turbulence which manifests optically as random phase aberrations. Nevertheless, there has been significant progress and several impressive demonstrations in using spatial modes of light for multiplexing [54, 56–61]. To date, the fastest MDM demonstration has sustained a data rate of 1.036 Pbps over a lab-bench using 26 OAM modes together with wavelength and polarisation [62]. The farthest MDM FSO communication demonstration in turbulence has been 80 Gbps over a mere 260 m [59] - turbulence is clearly a significant challenge. A recent numerical study investigated the application of these OAM modes for Ground to Satellite communications [63]. The study demonstrated that it is quite feasible to employ spatial modes with OAM in such long-distance applications under the conditions that the ground station is placed at a high altitude to limit the effect of atmospheric seeing, choosing a suitable wavelength and using adaptive optics techniques. These conditions will minimize the degradation of the spatial mode due to atmospheric turbulence. In addition, it was demonstrated that vortex modes can significantly increase the performance of obscurated optical receivers by bypassing the central secondary mirror, thereby improving the total light received by the telescope [64–66]. Recent literature has also started to explore the feasibility of spatial modes carrying orbital angular momentum in Light Detection and Ranging (LIDAR) applications (typically with of range less than 350 km) [64, 67–69]. While no

definite conclusions have been determined yet, it is suspected that these modes might be able to improve the performance of LIDAR systems by spatially filtering background light during the day and allow Rayleigh-Mie scattering to be uniquely distinguished from multiple scattering from rough surfaces.

From the aforementioned studies, it is evident that long range laser applications can benefit from the different properties that different spatial modes exhibit. Since different sets of spatial modes have different characteristics and symmetries, it is reasonable to question their respective basis dependent performances in turbulence. This work explores various characteristics of different spatial modes of light and accessing their resilience and therefore range for free-space propagation. We study their propagation both in the laboratory setting and through real word turbulence. We not only compare the spatial modes with the traditional Gaussian mode, but we also compare different spatial modes in attempt to determine the one most suitable for certain conditions, such as aperture size or turbulence strength. This PhD work provides a crucial first step towards understanding of the dynamics of structured light as a possible alternative to the fundamental Gaussian mode for purposes of laser ranging.

1.2 Outline

In the following chapters, we will introduce the theoretical background and experimental tools that were used to study the impact of different disturbances on various spatial modes. In Chapter 2 we provide the theory of these spatial modes along with their novel properties. We also provide a theoretical framework of how to generate and measure the modes using Spatial Light Modulators. The holograms are calculated by phase only and complex amplitude modulation techniques. The measurement process works in reverse by measuring coefficients of modes that make up an arbitrary optical field, a process known as modal decomposition.

In Chapter 3, we provide the background of laser beam propagation through atmospheric turbulence. Particularly, we outline the wavefront distortions such as beam wander, beam spread and scintillation effect laser beam and their respective mathematical descriptions based on the Kolomogorov turbulence theory. We also provide theoretical and experimental tools on how to simulate turbulence in the laboratory using the power spectrum and Zernike expansion approaches. Lastly, we explain how to characterise turbulence in real world links from beam wandering effects.

In Chapter 4 we apply the tools developed in Chapter 2 to compare the resilience of Hermite-Gaussian and Laguerre-Gaussian modes to displacements in different directions. By performing a modal decomposition after applying the displacements, we show the Hermite-Gaussian modes experience less crosstalk and mode dependent losses compared to the Laguerre-Gaussian modes when subjected to lateral displacements. It was also shown, over a normal distribution of lateral displacements that Hermite-Gaussian modes experience significantly less crosstalk and mode dependent losses than the Orbital Angular Momentum modes (OAM). This shows how the rectangular symmetry of Hermite-Gaussian modes can be exploited to reduce modal power losses in free-space optical communication systems.

In Chapter 5 we address the controversial issue of self-healing of Bessel-Gaussian modes through phase disturbances. By disturbing Bessel-Gaussian modes through Zernike aberrations, we show geometrically and experimentally that the modes do not completely self-heal as would be expected with an opaque obstructions. Contradictory, we explain why strong aberrations may show self-healing while weak aberrations will not, and highlight the parameters that influence this. Finally, we combine aberrations to pass the Bessel beam through turbulence, and debunk the myth that Bessel beams are resilient to such perturbations. This is based on the premise that all the conical waves become discussed, therefore eliminating all chances of self-healing.

In Chapter 6 we explore the feasibility of shape-invariant Bessel modes for long-range propagation. The modes, which counter the depth of focus limitation of traditional Bessel modes, are propagated through a 150 m real-world outdoor free-space link to study the effect of turbulence on modal crosstalk. The link was characterised using the techniques discussed in Chapter 3. We demonstrate not only the successful generation and measurement of these modes through the link but show that the modal crosstalk is comparable to that of helical Orbital Angular Momentum modes. Finally, we conclude by summarising the findings of our research and outline the potential applications in free-space long range propagation in chapter 7.

Chapter 2

Spatial modes of light

2.1 Introduction

The Gaussian mode is the fundamental mode of most laser resonators, and has the highest possible mode quality factor ($M^2 = 1$) compared to higher-order modes, optimising the radiance or brightness of the laser beam. However, the Gaussian profile is not always ideal for some applications which, for instance, require a uniform intensity profile. In such cases, it becomes necessary to redistribute the Gaussian profile into different spatial modes which might carry interesting properties. In this section, we discuss some of the most common higher-order spatial modes and the methods used to generate them.

Laser beams are electromagnetic fields that satisfy the Helmholtz equation [70]. In the case of scalar fields with a uniform polarisation, we can treat the electric field as a scalar field, U, a solution to the scalar Helmholtz equation:

$$[\nabla^2 + n^2 k^2] U(\mathbf{s}, z) = 0, \tag{2.1}$$

where $\mathbf{s}$ refers to the transverse coordinates which can be Cartesian where $\mathbf{s} \triangleq (x, y)$ or cylindrical where $\mathbf{s} \triangleq (r, \phi)$ and z refers to the propagation direction of the field. Here, $k = (2\pi)/\lambda$ is the wave number in vacuum and n is the refractive index of the medium in which the field propagates, where $n = 1$ in a vacuum. The wavelength is given by λ and for visible and near-infrared wavelengths (for example between 400 and 1600 nm) is on the order of hundreds of terahertz. Solutions to the Helmholtz equation are referred to as modes, and depend on the transverse coordinates on which U is solved, in conjunction with specific boundary conditions. The various modes are described by their respective mode indices and form a complete set of orthogonal basis which allow decomposition of

arbitrary spatial modes into the fundamental mode sets. The following sections outlines some special solutions in Cartesian and cylindrical coordinate systems.

2.2 Hermite-Gaussian modes

A solution to the Helmholtz equation in Cartesian coordinates results in Hermite-Gaussian modes [71–73]. This is made possible by the separability of the Helmholtz equation in x and y variables. The solution can be described mathematically as

$$U(x,y,z) = E_0 H_m\left(\sqrt{2}\frac{x}{w(z)}\right) H_n\left(\sqrt{2}\frac{y}{w(z)}\right)\frac{w_0}{w(z)} \times \exp\left[-i\psi_{mn}(z)\right]\exp\left[i\frac{k}{2q(z)}r^2\right]. \tag{2.2}$$

Here $H_m(\cdot)$ denotes the Hermite polynomials of order m and n. E_0 is a constant electric field amplitude, $w(z)$ is the beam size at propagation distance z, w_0 is the beam size at the beam waist, $z_0 = \pi {w_0}^2/\lambda$ is the Rayleigh range, $\psi_{mn}(z) = (m+n+1)\tan^{-1}(z/z_0)$ is the Gouy phase shift and $q(z) = z - iz_0$ is the complex beam parameter. The solution reduces to the fundamental Gaussian beam when $m = n = 0$. Intensity patterns of various Hermite-Gaussian modes of various orders are displayed in Fig. 2.1. The modes exhibit a rectangular structure synonymous with rectangular resonators from which they originate.

There are several methods of generating Hermite-Gaussian modes in the laboratory. These include intra-cavity techniques utilising various excitation techniques [74–79], astigmatic mode converters [80] and digital generation using Spatial Light Modulators (SLM) [81] and Digital micro-mirror (DMD) devices [82–84]. Due to their unique phase and amplitude structure, as well as their rectangular symmetry, these modes have found useful applications in optical trapping [85–89] and optical communications [90–97].

2.3 Laguerre-Gaussian modes

Another special case of spatial modes are the Laguerre-Gaussian modes, which are solutions to the scalar Helmholtz equation in cylindrical coordinates. These modes can be mathematically described as [73, 98]:

$$U(r,\phi,z) = E_0 \left(\sqrt{2}\frac{r}{\omega}\right)^{|\ell|} {L_p}^{\ell}\left(2\frac{r^2}{\omega^2}\right) \frac{w_0}{w(z)} \exp\left[-i\psi_{p\ell}(z)\right] \times \exp\left[i\frac{k}{2q(z)}r^2\right] \exp(i\ell\phi), \tag{2.3}$$

where $L_p^{\ell}(\cdot)$ is the associated Laguerre polynomial characterised by indices ℓ and p which denote the topological charge and the radial factor respectively. When $\ell = p = 0$, the solution also reduces to the well-known Gaussian beam. The factor $\exp(i\ell\phi)$ describes the helical phase front associated with the mode, which imparts Orbital Angular Momentum (OAM) of ℓh per photon [98]. Fig 2.1 displays examples of Laguerre-Gaussian modes, $LG_{p,\ell}$ of various azimuthal (ℓ) and radial orders (p). The orthogonality of the modes have been seen to increase the channel capacity of optical communication channels [51, 52, 55, 99–104]. These modes can be generated by static diffractive optical elements such as spiral phase plates [105–107] and versatile digital holograms encoded on SLMs [108–113] and DMDs [113, 114].

2.4 Bessel-Gaussian modes

Bessel modes are another type of spatial modes which have been topical in the optics community due to their self-healing and non-diffracting nature. These modes, first discovered by Durnin, are exact solutions to the paraxial wave equation [115, 116]. These modes have infinite energy and therefore cannot be realised physically in the laboratory. It is possible to create approximations of these modes by incorporating a Gaussian envelope, which limits the transverse and longitudinal extent of the modes. These approximations, illustrated on the third row of Fig. 2.1 are called Bessel-Gaussian modes which are solutions to the Helmholtz equation in cylindrical coordinates, characterised by a transverse intensity profile based on the family of Bessel functions. They are mathematical described as [117]:

$$U(r,\phi,z) = E_0 \frac{w}{w(z)} \exp[i\psi(z)] \exp\left[i\frac{k}{2q(z)}r^2\right] \times J_\ell\left(\frac{\beta r}{1+iz/z_0}\right) \exp\left[\frac{\beta^2 z/(2k)}{1+iz/z_0}\right] \exp[i\ell\phi], \tag{2.4}$$

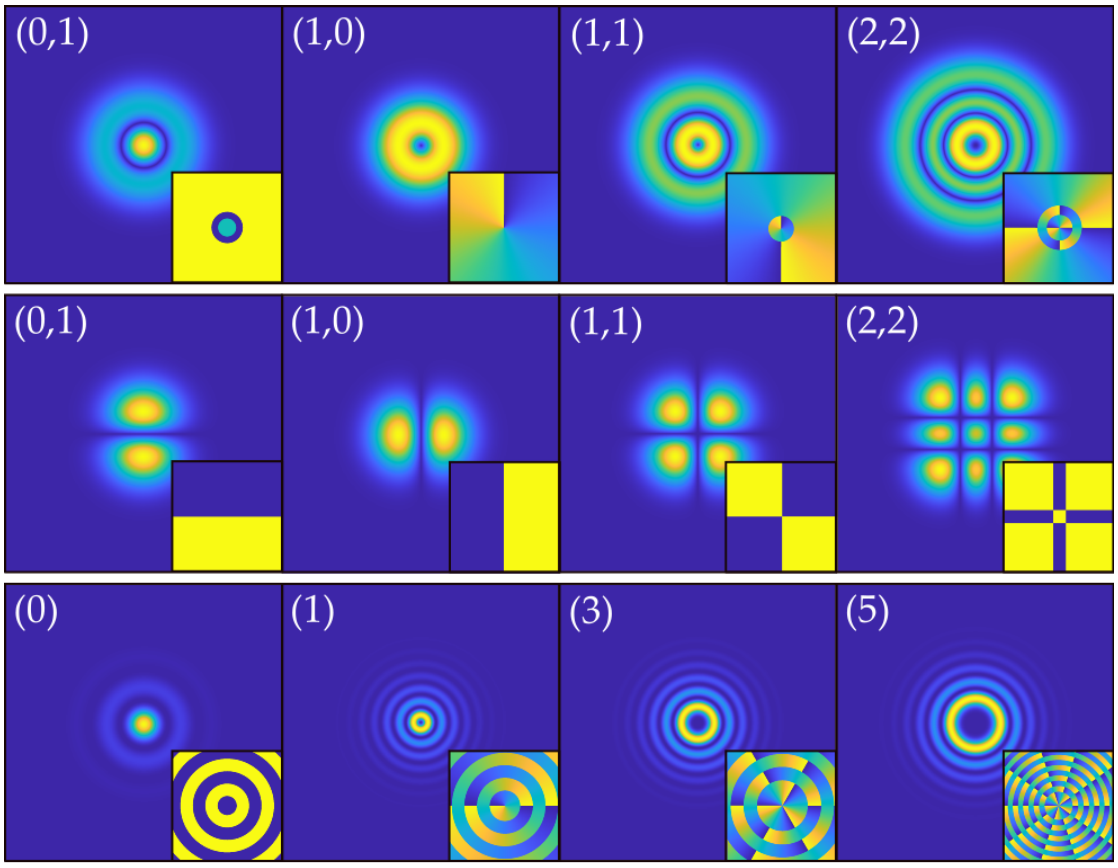


FIGURE 2.1: Intensity patterns with inset phase of Laguerre-Gaussian, Hermite-Gaussian and Bessel-Gaussian modes of various orders. The first row depicts LG (ℓ, p) modes, the second row depicts HG (m, n) modes and the third row depicts BG (ℓ).

where β relates to the wave vector of the plane waves which form the mode and J_ℓ is the Bessel function of the ℓ^{th} order. Bessel-Gaussian modes exhibit non-diffracting properties during propagation [118, 119]. This means they will maintain their size as they propagate without any diffractive spreading. Another interesting property is their ability to self-reconstruct their spatial profile after encountering small sized opaque obstructions [120, 121].

The formation of Bessel modes can be thought of as a superposition of plane waves propagating as a cone as illustrated in Fig. 2.2. These plane wave interfere at a defined angle θ which determine the depth of focus z_{max} of the Bessel beam as well as the spacing between the individual rings which form part of the Bessel structure. The beam only exists within the depth of focus and upon further propagation evolving into an annular ring. This translates to the angular spectrum or the diffraction pattern in the far field, of the mode to take the form of an annular ring. It is within this region that Bessel beams exhibit their non-diffracting and self-healing properties.

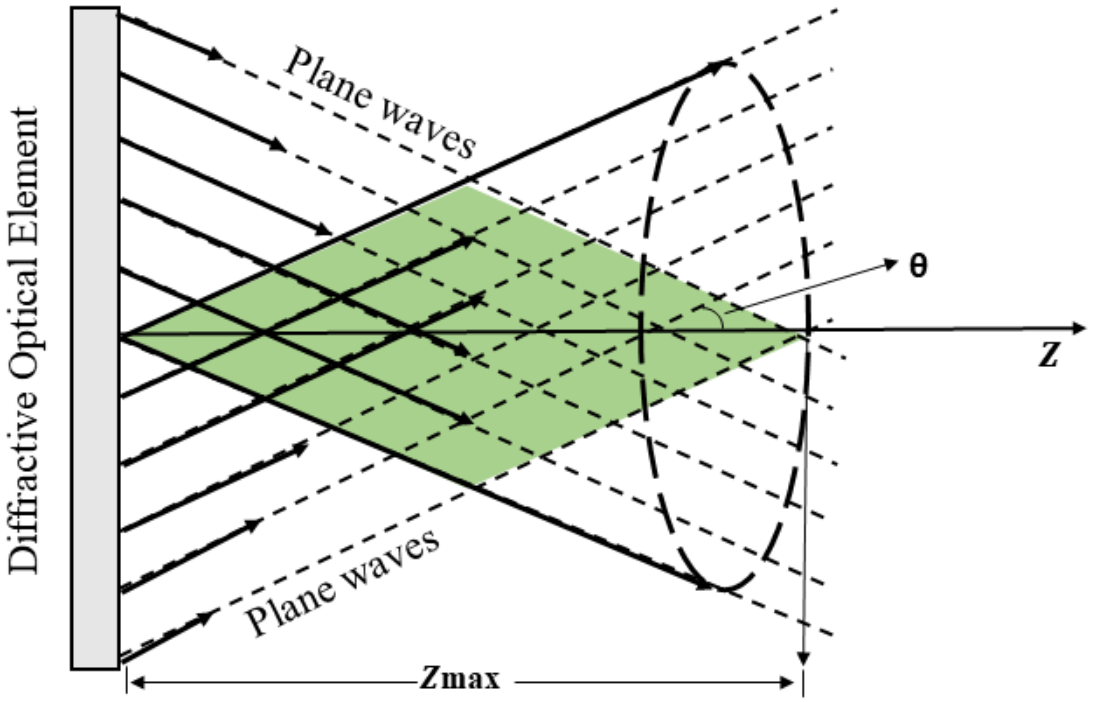


FIGURE 2.2: The formation of Bessel beams by superposition of plane waves propagating on a cone.

2.5 Creation and detection of spatial modes

The creation of customised light fields, also known as laser beam shaping, involves the redistribution of the conventional Gaussian mode into any desired complex light pattern with particular phase and intensity properties [122–125]. The earliest techniques used for the generation of these modes include manipulation inside laser cavities and making use of refractive and diffractive optical elements [125]. These techniques are not common in most laboratories as they often require precise fabrication of the elements and configured to generate specific modes. Here, we will discuss digital holographic methods which provide an alternative to these methods by allowing versatile and on demand creation of arbitrary complex fields. In addition, the envisaged optical fields do not need to exist physically, which allows generation of idealized phase patterns. The most common digital holographic devices are SLMs and DMDs, which tailor specific light modes by modulating either the phase, amplitude or both. The theoretical techniques discussed in this work are for SLMs but can easily to transferred to DMDs.

2.5.1 Digital holography

Conventional holography is based on the principle of interference between an object beam and a reference beam to create a hologram recorded on a photographic film [126].

When the hologram is illuminated with the initial reference beam, a holographic image of the desired mode can be retrieved. In the case of digital holography, the object beam does not need to physically exist but can be mathematically formulated and displayed on holographic devices such spatial light modulators for digital implementation.

Spatial light modulators are birefringent wavefront shaping devices that can modulate phase of incident light beams in order to create desired optical field patterns [127–132]. They consist of pixelated liquid crystal displays which are electrically controlled by a circuit board connected to a computer. Mathematically computed grey-scale holograms are programmed onto the SLM which alters the phase of the illuminated reference laser light according to the shade of grey present at each pixel of the hologram image. The hologram image consists of 256 grey levels which correspond to modulation in the range [0,2π]. Black represent no modulation while white (or 2π) represent full phase modulation. SLMs are however not 100% efficient. This means that not all the incident light will be modulated. As a result, the light reflected from the liquid crystal display will consist of a superposition of the modulated encoded beam and the unmodulated reference beam. To separate the modulated light from the unmodulated light, a diffraction grating is added on to the computer generated hologram, deflecting the modulated light to the first order and the unmodulated light to the zeroth order.

2.5.2 Hologram generation

Light manipulation requires full control of both its amplitude and phase in a spatial manner. SLMs are phase-only devices, which means they allow direct control of the phase while the amplitude control is achieved indirectly. Many advanced techniques allows this to be done in multiple steps through a two element approach, where one element controls the phase and the other controls the amplitude [125, 133, 134]. This approach can be mimicked using a SLMs using digital holograms that generate the desired modes in a single step [135–153]. To generate a desired beam given by $\mathbf{E_{out}}(x,y) = A_{\mathbf{out}}(x,y)\exp(i\Phi_{\mathbf{out}}(x,y))$ using a phase-only hologram $H = H(x,y)$ from a reference beam given by $\mathbf{E_{in}}(x,y) = A_{\mathbf{in}}(x,y)\exp(i\Phi_{\mathbf{in}}(x,y))$, the transformation function is needed in the form:

$$\begin{aligned} t &= \frac{E_{\mathbf{out}}(x,y)}{E_{\mathbf{in}}(x,y)} = \frac{A_{\mathbf{out}}(x,y)}{A_{\mathbf{in}}(x,y)}\exp[i(\Phi_{\mathbf{out}}(x,y) - \Phi_{\mathbf{in}}(x,y)] \\ &= A_{\mathbf{rel}}\exp[i(\Phi_{\mathbf{rel}}(x,y)] \end{aligned} \tag{2.5}$$

A phase grating can be added in the hologram in the form:

$$\Phi(x, y) = \mod (2\pi x G_x, 2\pi), \tag{2.6}$$

where G_x is the grating frequency or the inverse of the period along the x direction.

The simplest approach used to generate the holograms is simply by imparting the relative phase:

$$H(x, y) = \Phi_{\mathbf{rel}}(x, y). \tag{2.7}$$

The output mode will have the desired phase with the amplitude equal to that of the input mode. This technique is sufficient when only the phase of the output mode is needed. However, when the amplitude information is required, such as when generating $LG_{p\ell}$ modes, the amplitude information has to included in the hologram. This technique, referred to as complex amplitude modulation, seeks to find a scaling function $f(A(x, y))$ that relates the amplitude and phase variations in a form that is phase-only. The hologram will take the form:

$$H(x, y) = f(A(x, y))\Phi_{\mathbf{rel}}(x, y). \tag{2.8}$$

One way to do this is by representing the hologram as a Fourier series in the domain of f. The hologram can then be expressed as [145]:

$$H(x, y) = f(A_{\mathbf{rel}}(x, y)) \sin(\Phi_{\mathbf{rel}}(x, y)), \tag{2.9}$$

where $f(A_{\mathbf{rel}}(x, y))$ is obtained through numerical inversion of:

$$J_1[f(A_{\mathbf{rel}}(x, y))] = aA_{\mathbf{rel}}(x, y), \tag{2.10}$$

where a ranges from 0 to 0.5819, which is the maximum of the first order Bessel function $J_1(x)$. This method is colloquially referred to as the 'cookie cutter' method since the spatial shape and phase of the desired mode are determined from an input plane wave. Holograms for generating a few spatial modes are displayed in Fig 2.3.

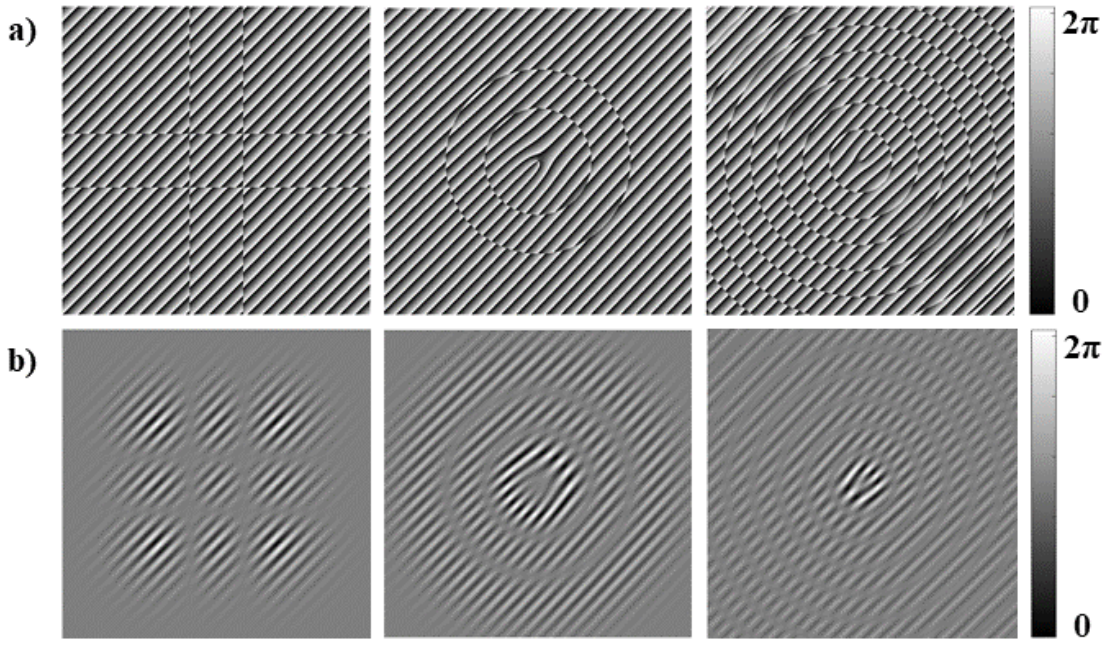


FIGURE 2.3: Examples of holograms generated by a) phase-only and b) complex amplitude modulation. The first column generates $HG_{2,2}$, second column $LG_{2,2}$ and third column BG_2.

2.5.3 Mode characterisation by modal decomposition

Equally as important to the creation of spatial modes is their measurement process. The ISO standard for measuring laser beams allows for a full modal decomposition to be performed. Modal decomposition is a powerful tool used to characterise or unravel optical fields according to its constituent modes [81, 154, 155]. This is based on the premise than any unknown optical field can be expressed as a linear combination of orthonormal basis functions. This can be mathematically represented as:

$$U(r) = \sum_{l=1}^{N} c_l \Psi_l(r), \tag{2.11}$$

where $r = (x, y)$ are the spatial coordinates, $c_l = \rho_l \exp i\Delta\Phi_l$ are the complex expansion coefficients, $\Psi_l(r)$ is the lth basis mode with amplitude ρ_l, $\Delta\Phi_l$ is the inter-modal phase difference between the mode and some reference mode (usually the fundamental mode) and N is the number of modes. The choice of the basis function Φ_l depends on the geometry of the problem, which could be LG for circular symmetry or HG for rectangular symmetry. In principle, any orthogonal set would work. All the physical parameters of the unknown mode are contained in the complex valued coefficients. Measurement of these weightings is the core of modal decomposition and is achieved by finding the inner product of the unknown field and each basis element, i.e,.

$$\rho_l{}^2 = |\langle U|\Psi_l\rangle|^2. \tag{2.12}$$

The hologram used to perform this operation is called a match or correlation filter because it measures the correlation signal between the unknown incoming mode and the function encoded on the hologram. The inner product yields an intensity on the optical axis at the Fourier plane that is proportional to the power content of each mode. To extract the amplitude of each basis element, the conjugate complex of the respective element is encoded as the transmission function [154, 156]:

$$T_l(r) = \Psi_l{}^*(r), \tag{2.13}$$

where the asterisk denotes complex conjugation. The inter-modal phase difference $\Delta\Phi_l$ is measured with respect to some reference mode Ψ_0 using two transmission functions which represent the interferometric superposition of the two modes [154]:

$$T_l{}^{\mathbf{cos}}(r) = \frac{\Psi_0{}^*(r) + \Psi_l{}^*(r)}{\sqrt{2}}. \tag{2.14}$$

$$T_l{}^{\mathbf{sin}}(r) = \frac{\Psi_0{}^*(r) + i\Psi_l{}^*(r)}{\sqrt{2}}. \tag{2.15}$$

The inter-modal phase difference $\Delta\Phi_l$ is then determined from:

$$\Delta\Phi_l = -\arctan\left[\frac{2I_l^{\mathbf{sin}} - \rho_l{}^2 - \rho_0{}^2}{2I_l^{\mathbf{cos}} - \rho_l{}^2 - \rho_0{}^2}\right] \tag{2.16}$$

All these measurements can be done simultaneously from one diffraction pattern by using spatially multiplexed holograms. In this case, each mode is assigned its own carrier frequency to separate the modes at the Fourier plane. The transmission function is expressed as [154]:

$$T(r) = \sum_{n=1}^{3N-2} T_n(r)\exp(iK_n r), \tag{2.17}$$

where K_n is the grating frequency and N is the number of holograms.

2.6 Conclusion

In this chapter, we provided theoretical background of some of the complex modes studied in the upcoming chapters, outlining their novel properties and methods of creation. For the purposes of our study, we specifically focus on digital holographic methods using SLM's to generate and characterise the modes. We describe the techniques used to calculate the holograms which are categorised as either phase-only or complex amplitude modulation. We also describe how to detect these modes using modal decomposition, which represent an unknown optical field into weighted orthogonal modes. These techniques will be applied in subsequent chapters to generation and measurement after encountering various distortions to assess their resilience.

Chapter 3

Laser beam propagation through atmospheric turbulence

This Chapter contains extracts from a publication by Cox, Mitchell A., Nokwazi Mphuthi, Isaac Nape, Nikiwe P. Mashaba, Ling Cheng, and Andrew Forbes. "Structured Light in Turbulence." arXiv:2005.14586 (2020).

3.1 Introduction

All laser systems which propagate through free-space are subjected to degradation due to atmospheric turbulence and other weather related effects. While the latter effects could easily be mitigated by transmission through ideal weather conditions, the effects of turbulence are inevitable. Turbulence occurs mainly because of typical diurnal variations that occur as the temperature fluctuates throughout the day. These temperature fluctuations in turn lead to spatial and temporal variations in the refractive index structure. We begin by discussing the most common effects of turbulence and the impact they have on laser beams. We then provide a toolkit on how turbulence can be studied in the laboratory environment. Lastly we detail the ways turbulence can be modelled in the real-world and the instruments that can be used characterise the strength of turbulence.

3.2 Atmospheric effects of turbulence

The refractive index of the atmosphere is not uniform. It consists of a multitude of eddies of different sizes, each with varying indices of refraction. As a laser beam propagates through the atmosphere, its wavefront will be distorted by these variations. The

variations are caused by the fluctuations of temperature which arise from the turbulent mixing of various thermal layers. The average size of the turbulent eddies can be specified by an inner scale, l_0, which is typically on the order of millimetres and an outer scale, L_0, which is on the order of meters [33]. The Kolmogorov model for turbulent flow is the basis for many contemporary theories of turbulence and is able to relate these temperature fluctuations to refractive index fluctuations. Kolmogorov turbulence assumes that solar heating and wind shear provides energy on large scales (the outer scale, L_0) and it is dissipated as heat by viscous action of the air to the smaller eddies (inner scale, l_0) [157]. The power spectral density of the refractive index fluctuations given by the Kolmogorov model is described by [157]

$$\Phi_n^K(\kappa) = 0.033 C_n^2 \kappa^{-11/3} \quad \text{for} \quad 1/L_0 \ll \kappa \ll 1/l_0, \tag{3.1}$$

where $\kappa = 2\pi(f_x \cdot \hat{x} + f_y \cdot \hat{y})$ is the angular spatial frequency vector and C_n^2 is the refractive index structure parameter, which is a measure of the strength of the refractive index fluctuations. Values of C_n^2 vary from 10^{-17} m$^{-2/3}$ in "weak" turbulence and up to about 10^{-13} m$^{-2/3}$ in "strong" turbulence [33].

3.2.1 Beam spreading

In the absence of turbulence, the spread of the laser beam will depend on the diameter of the transmitting aperture D. For a diffraction-limited transmitter the angular spread θ_0 of the beam in the far-field is given by $2\lambda/\pi D$, where λ is the wavelength of the beam. Through turbulence, the spread becomes much larger than θ_0 at the receiver plane due to scattering by the moving turbulent eddies. The total spread of the beams is made up of two effects; beam wander, which results from larger turbulent eddies (discussed in the following section), and beam broadening which result from eddies smaller than the transmitting aperture D. The latter, also referred to short-term beam spread depends on a parameter referred to as the lateral coherence length or the Fried parameter r_0. It is a useful alternative to C_n^2; for a plane wave (approximately a collimated Gaussian beam) in Kolmogorov turbulence, given by

$$r_0 = 1.68 \left(C_n^2 L k^2\right)^{-3/5} \tag{3.2}$$

and for a plane wave in unspecified turbulence,

$$r_0 = \left(0.423 k^2 \int_0^L C_n^2(z) dz\right)^{-3/5}, \tag{3.3}$$

where k is the wavenumber and L is the propagation path length. If the beam diameter D is much smaller than r_0, the effect of turbulence on the beam is negligible and the diameter of the spread will solely depend on θ_0. However, if the transmitting diameter is much larger than the coherence length, the diameter of the spread will depend on r_0 in the form of $\theta_0 = 2\lambda L/\pi r_0$, where λ denotes the wavelength.

3.2.2 Beam wander

When the turbulent eddies are much larger than the diameter of the beam, the beam will be randomly deflected along its path, resulting in beam wander, also known as long-term beam spread. This effect leads to a displacement of the centroid which can cause deep fading in applications such as free-space optical communication where the beam misses the receiver aperture (in extreme cases) or the detector (focal spot beam wander position). Beam wander at the receiver plane is statistically modelled by a Gaussian distribution which is characterised by a long-term average radial variance, r_c^2, as well as the size of the received beam without any averaging (the short-term beam), denoted by ω_{ST} [33]. It is intuitive to think that a smaller short-term beam which wanders will result in an average larger Gaussian shaped long-term beam, according to the central limit theorem [158]. The size of the long-term beam, ω_{LT}, is given by

$$\omega_{\mathrm{LT}}^2 = \omega_{\mathrm{ST}}^2 + r_c^2. \tag{3.4}$$

Several analytical solutions for the beam wander radial variance exist. For infinite outer scale Kolmogorov turbulence, the beam wander radial variance for a collimated beam is given by [159]

$$r_c^2 = 2.42 C_n^2 L^3 \omega_0^{-1/3}, \tag{3.5}$$

where ω_0 is the beam waist radius.

3.2.3 Scintillation

In addition to the fluctuations in beam size and position, atmospheric turbulence also induces fluctuations in intensity. This effect is called scintillation and occurs when the inhomogeneities are much smaller than the diameter of the beam. Small portions of the beam undergo interference due to diffraction and refraction as a result of the inhomogeneities. This causes the beam to alternate between light and dark patches in space and time. For a plane a wave in weak Kolmogorov turbulence, scintillation can be estimated from the Rytov variance given by [33]

$$\sigma_R^2 = 1.23 C_n^2 k^{7/6} L^{11/6}. \tag{3.6}$$

The variance due to scintillation increases as turbulence increases or as the propagation length is increased. This in turn means that long distance propagation in weak turbulence is as detrimental to the beam as short propagation in strong turbulence. Scintillation can be reduced by aperture averaging, where the receiving aperture of the beam is increased in order to statistically average the independent portions of the scintillated beam [160].

3.3 Simulating turbulence in the laboratory

Here we outline two general approaches to simulating optical turbulence using SLMs and DMDs for use in a lab environment. They have been utilised in a myriad of experiments for studying the evolution of spatial modes through turbulence [161–163]. The turbulence screens can also be used for computer simulations.

Various numerical methods have been developed to approximate the phase that is imparted on optical beams upon traversing turbulence. One such technique approximates the phase screen as a random phase function with a variance of [164]

$$\sigma^2(x, y) = \left(\frac{2\pi}{N\Delta x}\right)^2 \Phi(k_x, k_y), \tag{3.7}$$

for an $N \times N$ grid over which the screen is generated. Here Δx is the grid spacing, while k_x and k_y are the spatial frequencies over the grid and $\Phi(k_x, k_y)$ is the phase spectrum given by

$$\Phi(k_x, k_y) = 2\pi k_0^2 L \Phi_n(k_x, k_y). \tag{3.8}$$

Here $\Phi_n(k_x, k_y)$ is the refractive index power spectrum, L is the distance over which the screen is simulated for and k_0 is the wave-number (in vacuum) of the optical beam to be used. The desired phase screen can be computed from

$$\phi(x, y) = \text{Real}\left\{\mathcal{F}^{-1}\left(\ \chi(k_x, k_y)\sigma(k_x, k_y)\ \right)\right\}, \tag{3.9}$$

where $\chi(k_x, k_y)$ is a complex matrix of size $N \times N$ with random entries sampled from a normal distribution with 0 mean and a variance of 1. $\mathcal{F}^{-1}$ denotes the inverse Fourier transform, where the Fast Fourier Transform (FFT) may be used. Although here we show that the screen is extracted from the real part, it can in principal also be extracted

from the imaginary part. Furthermore, the phase spectrum must be set to zero at the origin $\Phi(0,0) = 0$ to avoid a large piston component in the final screen.

Examples of generated phase screens are shown in Fig. 3.1 (a), in order of increasing turbulence from left to right. The turbulence strength is given as the Strehl ratio (SR) which is a common but less descriptive parameter to specify turbulence strength. It is defined by the ratio of the average on-axis beam intensity with, $\langle I(\mathbf{0})\rangle$, and without, $I_0(\mathbf{0})$, turbulence. The experimental technique to measure this is discussed further on in the section.

The screens as generated do not accurately model atmospheric turbulence since they cannot perfectly represent low-order spectral components and therefore produce statistics that do not conform to the theoretical structure function. As a result, sub-harmonic methods to include low order components have been developed [165]. Example phase screens that include these lower order components are shown in Fig. 3.1 (b).

The second method generates phase screens, shown in Fig. 3.1 (c), as superpositions of Zernike polynomials following the expansion

$$\psi(r,\theta) = \sum_{j=0}^{J} a_j Z_j(r,\theta) \tag{3.10}$$

where (r,θ) are polar coordinates, J is the last index of the used modes and $Z_j(r,\theta) \equiv Z_{m,n}(r,\theta)$ denote the Zernike polynomials. Zernike polynomials are a sequence of polynomials that are orthogonal over a unit circle and commonly used to represent wave-front distortions in optical beams [166]. The modes can be written as

$$Z_{m,n}(r,\theta) = \begin{cases} \sqrt{2(n+1)} R_n^m(r) G_m(\theta) & m \neq 0 \\ R_n^0(r) & m = 0 \end{cases}, \tag{3.11}$$

where the index j can be mapped onto the double index, (m,n), for positive integers $m \leq n$ following the Noll convention [167]. The functions $R_n^m(r)$ and $G^m(\theta)$ are the radial and azimuthal factors given by

$$R_n^m(r) = \sum_{s=0}^{(n-m)/2} \frac{-1^s (n-s)!}{s!\ \left(\frac{n+m}{2}-s\right)!\ \left(\frac{n-m}{2}-s\right)!}, \tag{3.12}$$

and

$$G_m(\theta) = \begin{cases} \sin(m\theta) & j\ is\ \text{odd} \\ \cos(m\theta) & j\ is\ \text{even} \end{cases} \tag{3.13}$$

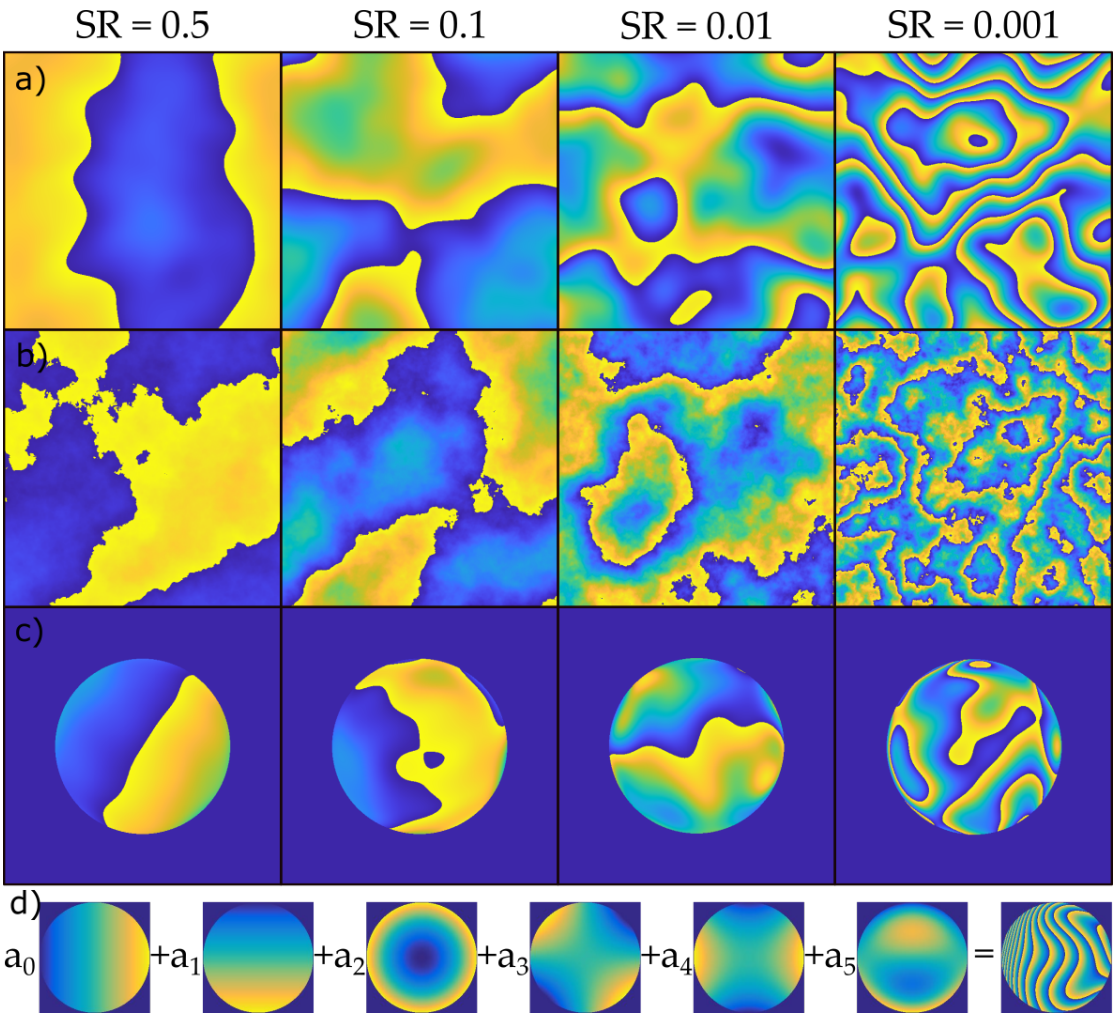


FIGURE 3.1: Random phase screens of varying turbulence strength represented by Strehl ratio. Rows from top to bottom are for the inverse power spectrum approach (a), the sub-harmonic method (b) and the Noll (Zernike) method (c). The last row illustrates the individual Zernike phase screens which make up the Noll method with indices ranging from $j = 1$ to $j = 6$ (d), although in reality up to 60 screens are required for a physically accurate result.

Examples of the first few Zernike modes in the Noll convention are shown in Fig. 3.1 (d), contributing in the construction of a phase screen. We list the first three indexes: $j = 2$ (or $(m, n) = (1, 1)$), $j = 3$ (or $(m, n) = (0, 2)$) and j = 4 (or $(m, n) = (2, 2)$), which represent tilt, defocus and astigmatism respectively. Although the indexes $j = 1$ and $j = 2$ share the same index pairs, (m, n), and therefore the same radial factor, they have differing phase factors due to the phase function, $G(\theta)$; one is an even function while the other is odd.

Further, for the Kolmogorov spectrum the coefficients, a_j, can be sampled from a normal distribution with zero mean and a variance of, $\sigma^2_{nm} = I_{mn} \times (D/r_0)^{5/3}$, where I_{mn} can be determined from the diagonal terms of the Noll matrix [167]. The phase screens are therefore generated by making random drawings from the normal distribution with the

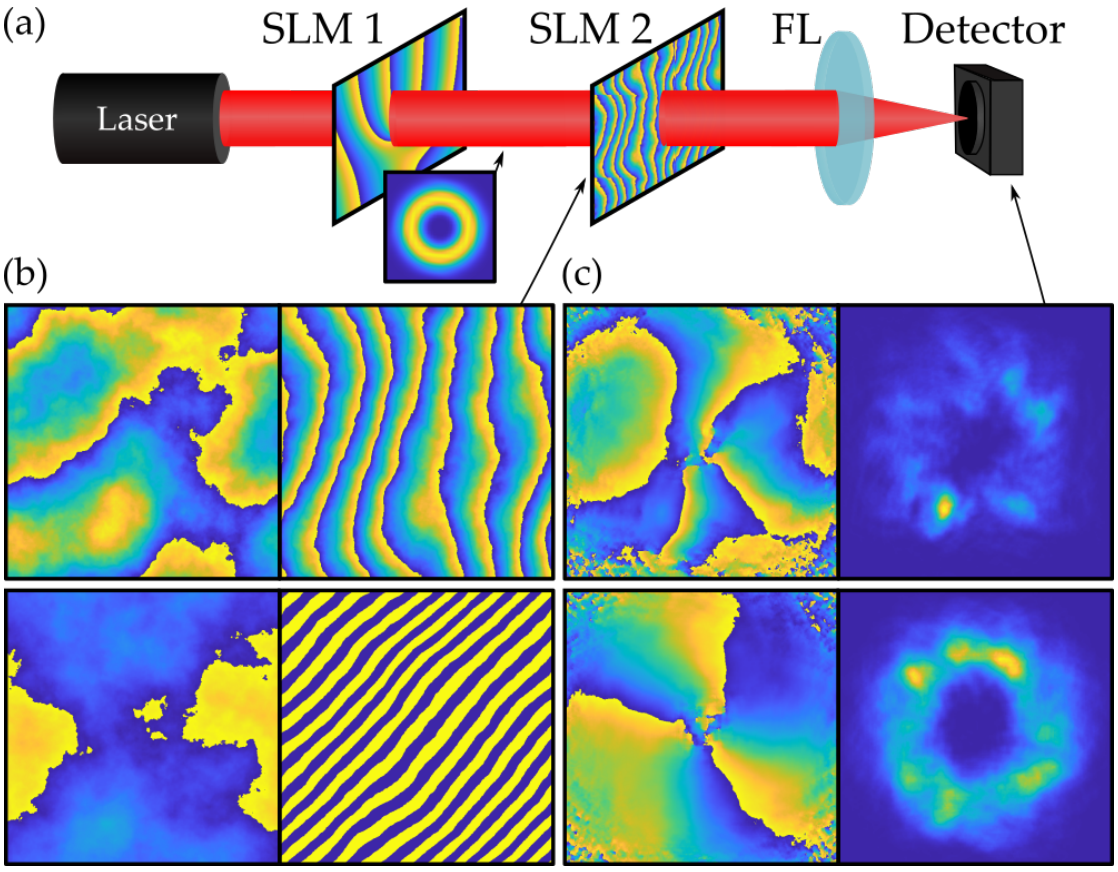


FIGURE 3.2: (a) Typical set-up for creating a mode and then aberrating it with turbulence (FL: Fourier Lens; SLM: Spatial Light Modulator). (b) Holograms for strong (top, SLM) and weak (bottom, DMD) turbulence with (right) and without (left) gratings. (c) Phase (left) and intensity (right) of $\ell = 3$ beams through the setup with the turbulence to the left.

appropriate variance to find each coefficient and using these in the summation of Eq. 3.10 to build a phase function that is representative of turbulence. Each drawing from the random distribution will produce new coefficients and therefore a new phase screen. Running these phase screens one after the other then represents changing turbulence of the same strength and following the same Kolmogorov statistics.

$$I_{mn} = \frac{0.15337(-1)^{n-m}(n+1)\Gamma(14/3)\Gamma(n-5/6)}{\Gamma(17/6)^2\Gamma(n+23/6)}. \tag{3.14}$$

This produces phase screens with statistical properties consistent with the Kolmogorov model for atmospheric turbulence.

Once the phase functions corresponding to the phase screens have been generated, the next step is to produce holograms that can be used to imprint the desired perturbation onto an optical beam. By way of example we will demonstrate this procedure for SLMs

and DMD devices. Given the phase function, $\psi(x, y)$, a hologram tailored for a phase-only device, can be calculated from [168]

$$H(x, y) = \mathrm{mod}\{\psi(x, y) + k_{\mathrm{ox}}x + k_{\mathrm{oy}}y, 2\pi\} \tag{3.15}$$

where the factors $k_{\mathrm{ox,oy}}$ are the grating frequencies in the x and y (Cartesian) directions, respectively. In this way, a structured blazed grating, with a phase depth of $[0, 2\pi]$ is generated.

Some devices allow for a modulation of up to 8π, which enables the simulation of steeper phase gradients with fewer pixels. The disadvantage of SLMs is their modulation speed which is typically tens of Hertz. The time scale at which turbulence changes is given by the Greenwood frequency, which for modest conditions is an order of magnitude higher.

For this reason DMDs are ideal: they have modulation speeds of kilohertz, allowing accurate simulation of realistically fast changing turbulence. Unfortunately, DMDs use an amplitude only hologram encoding which limits efficiency: the first diffraction order of a DMD has $< 10\%$ of the initial input power. The desired hologram can be calculated as [83]

$$H(x, y) = \frac{1}{2} + \mathrm{sign}\Big(\cos\left[k_{\mathrm{ox}}x + k_{\mathrm{oy}}y + \pi p(x, y)\right] + \cos(\ \pi w(x, y)\ )\Big), \tag{3.16}$$

where $w(x, y) = (1/\pi) \times \arcsin(A(x, y))$ and $p(x, y) = (1/\pi) \times \psi(x, y)$ corresponding to the amplitude and phase terms, respectively. Again, $\psi(x, y)$ plays the role of the phase function mapping the desired turbulence phase fluctuations. Since we only consider the phase variations, the amplitude term can simply be set to unity, i.e., $A(x, y) = 1$.

The resulting screens are binary images having zeros and ones as entries. Fig. 3.2 illustrates examples of holograms generated by SLMs and DMDs, along with the resulting beam phase and intensity. Fig. 3.2 (a) illustrates a typical experimental setup for generating and distorting the beam with turbulence. A collimated laser source is illuminated onto the modulating device encoded with a fork hologram of desired topological charge to create the vortex mode. The mode is then directed to another device imprinted with the calculated phase screen. The effect of the turbulence is then observed at the Fourier plane using a CCD detector. Examples of holograms for generating strong and weak turbulence is depicted at the top (SLM) and bottom (DMD) rows of Fig. 3.2 (b) respectively. The resultant beam phase and intensity is seen in Fig. 3.2 (c).

Now that we generated some phase screens and are able to produce holograms that can be used to modulate optical beams, how do we know if they have imparted the desired turbulence strength? The simplest way is to measure the Strehl Ratio which is given by

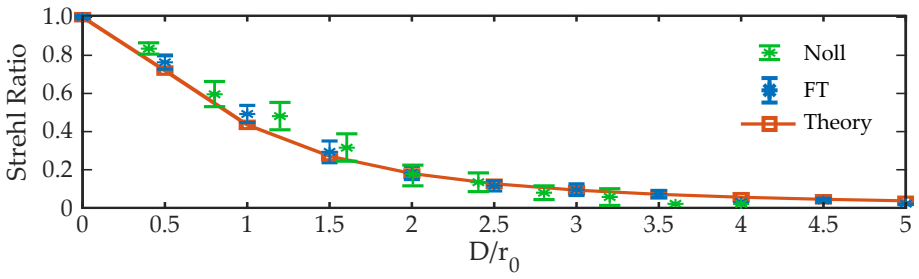


FIGURE 3.3: Experimental measurement of Strehl Ratio using turbulence screens generated using the spectrum inversion (FT) and Zernike (Noll) methods showing a close match to theory.

(for a plane wave in Kolmogorov turbulence)

$$\mathrm{SR} = \frac{\langle I(\mathbf{0})\rangle}{I_0(\mathbf{0})} \approx \frac{1}{[1+(D/r_0)^{5/3}]^{6/5}}, \tag{3.17}$$

where D is the aperture diameter. By using Eq. (3.17), it can be measured by comparing the on-axis intensity of the obstructed and unobstructed beams. The SR parameter produces a function scaling from 0 to 1, covering strong to weak turbulence, respectively. It is instructive to exploit the relation between the normalised aperture size, D/r_0, and the SR in calibrating phase screens in the lab. Since we want to generate turbulence strengths with a specific coherence length, r_0, it is ideal to calibrate the system by changing the aperture size argument, D, until the theoretical and experimental SR are equivalent for various values of D/r_0.

A schematic illustrating a typical setup for using this approach is shown in Fig. 3.2 (a) with examples of simulated and measured intensity patterns shown in Fig. 3.2 (b) and (c), respectively. In the setup, a collimated laser beam is incident on an SLM and imaged by a camera at the far-field of a Fourier lens for various turbulence strengths parameterised by D/r_0.

For each image, the on-axis intensity is recorded. The SR ratio can be calculated from these intensities and then compared to the theory. Examples of the measured SR are shown in Fig. 3.3 for a well calibrated system using the sub-harmonic spectrum inversion and Zernike (Noll) methods.

3.4 Real-world turbulence

In a real-world experimental setup one of the challenges is to accurately measure the turbulence parameters. In this section we move out of the laboratory and into the real-world, discussing how to characterise atmospheric turbulence in real-time. Before propagating a laser through terrestrial links, it is important to accurately characterise the

strength of the turbulence in order to quantify the attenuation which can be expected. This can be done by qualitative and/or quantitative means.

Qualitatively, the turbulence strength can be estimated from typical diurnal variations [5, 169, 170]. The strength of turbulence within the boundary layer is mainly affected by a diurnal cycle. The atmospheric boundary layer is the lowest part of the atmosphere that is affected by interaction with Earth's surface. During the day, solar radiation heats up the surface of the Earth causing the air above it to be warmer. When this happens, the cooler denser air will descend to displace it. The resulting vertical movement of air together with flow disturbances causes significant variations in the temperature structure. The turbulence is strongest during midday where the temperatures are highest. The air becomes more stable at night when surface cools down resulting in a temperature inversion. The cold and dense air limits density fluctuations resulting in minimal variations in the refractive index structure. This translates to weak turbulence during the night.

The turbulence strength can also be measured qualitatively through a number of techniques, the simplest of which is by transmitting a Gaussian beam through a system and measuring the turbulence strength from the beam wander effects, characterised statistically by the variance of the beam wander displacement given as [33]

$$\langle r_c^2 \rangle = \langle x^2 \rangle + \langle y^2 \rangle, \tag{3.18}$$

which denotes the mean square of the beam position on the detector. The optical turbulence parameter, C_n^2 can then be deduced from the beam wander through the relationship

$$C_n^2 = 0.328 \langle r_c^2 \rangle D^{\frac{1}{3}} L^{-3}, \tag{3.19}$$

where D is the diameter of the beam. To implement this experimentally, a Gaussian beam was sufficiently expanded (approximating a plane wave) and was propagated across the free-space link at different times of the day and the centroid position fluctuations monitored with a high frame rate camera. From these fluctuations, the beam wander displacement variance was calculated from Eq. 3.18 and the turbulence strength calculated from Eq. 3.19.

Unfortunately, this technique is only valid in weak turbulence. If the technique is not possible, or the turbulence regime is not weak, it is possible to accurately measure C_n^2 using other weather parameters such as wind speed, temperature and pressure. One

way of doing this is by using a three-dimensional wind vector instrument, called a sonic anemometer [171, 172]. A sonic anemometer is a solid-state, ultrasonic instrument which measures wind velocity in three orthogonal axes as well as the so-called sonic temperature. Sonic anemometers are commonly used for accurate wind measurements, but are sometimes used to measure near field turbulence around high towers, where optical communication links are situated. A numerical transformation is then applied to convert the resulting three wind vector components, together with temperature and pressure measurements, into an instantaneous sonic temperature, $T_s(t)$, from which the time dependent temperature structure function constant, $C_T^2(t)$, can be inferred. Using the Gladstone-Dale law it is trivial to convert this to the desired refractive index structure function, C_n^2. The advantage is that this device returns (by calculation) a time series of C_n^2 values which can be measured over a 24 hour period.

3.5 Conclusion

In this chapter, we discussed the atmospheric effects of optical turbulence on laser beam propagation. We outlined the process by which turbulence is formed and showed that it results to three major effects on the spatial properties of the beam, which are beam spreading, beam wander and scintillation. These effects induce variations in beam size, position and intensity respectively. Each effect depends on the size of the turbulence eddies distributed across the beam's cross-section in relation to the width. Turbulence eddies which are the same size of the beam width result in the beam spreading beyond vacuum diffraction, thereby reducing the irradiance at the target/receiver plane. Eddies much larger than the beam width will result in beam wandering effects where the beam centroid is displaced from its intended target or receiver. Scintillation, which is the fluctuations in beam's intensity occurs when the turbulent eddies are much smaller than the beam width.

We have also presented a toolkit on how to simulate turbulence in the laboratory environment using SLMs and DMDs. We showed how to calculate thin phase screens with desired turbulence statistics for encoding on these beam shaping devices. We discussed two approaches commonly used for calculation of turbulence phase screens. The first is a FFT based approach which utilizes a specific power spectral density to generate complex independent Gaussian random numbers with zero mean and unit variance. Random phase screens are then determined by taking the Fourier transform of the weighted power spectrum. The main drawback of this method is that it does not accurately represent low-order aberrations, which often make up a significant contribution in realistic turbulence models. This can be mitigated by using the second approach, which is based on

Zernike polynomials. The Zernike approach generates phase screens from a superposition of appropriately weighted orthogonal Zernike basis. The polynomial weightings are calculated for different turbulence strengths based on the Noll covariance matrix. We then experimentally demonstrated how the calculated phase screens can be encoded on wavefront control devices to perturb the beam at various turbulence strengths at remarkable modulation rates. Lastly, we discussed how to characterise atmospheric turbulence for real-world experiments by quantitative means. Under weak turbulence conditions, the strength of turbulence can be estimated from the statistical variance of the beam wander. This simple technique only requires a camera or photodiode to implement. Under strong turbulence conditions, one can make use of a sonic anemometer which estimates the wind velocity of sound waves as it travels through the atmosphere. Since the wind velocity depends on air density, it can be used to estimate temperature variations and therefore atmospheric turbulence. These techniques can serve as a valuable resource to allow the transition of many laboratory demonstrations into the real-world, a necessary step to push the limits in distance and information capacity. In the next chapters, we apply some of these techniques to study turbulence in the laboratory and real-world links.

Chapter 4

The resilience of orbital angular momentum and Hermite–Gaussian modes to tip/tilt aberrations

This Chapter contains extracts from a publication by Bienvenu Ndagano, Nokwazi Mphuthi, Giovanni Milione, and Andrew Forbes, "Comparing mode-crosstalk and mode-dependent loss of laterally displaced orbital angular momentum and Hermite–Gaussian modes for free-space optical communication," Opt. Lett. 42, 4175-4178 (2017).

4.1 Introduction

Free-space optical communication is the transmission of data over free-space with light [173]. It is high-speed, free from licensing and, deployable where optical fibers are not. As such, it underlies a number of burgeoning applications, such as, Facebook's *Internet.org* project which, aims to provide otherwise inaccessible and high-speed internet around the world [174].

As data speed requirements unabatedly increase, there is interest in methods with which to increase the data speed of free-space optical communication. Of particular interest is the use of spatial modes of light, referred to as OAM modes, which carry a well-defined OAM per photon [101]. OAM modes can be used as states with which to encode data, or as channels with which to carry data [51, 55, 175]. OAM modes are a subset of Laguerre-Gaussian modes ($LG_{0,\ell}$); when propagating in the z-direction, OAM modes

have an azimuthally varying phase given by $\exp(\imath\ell\phi)$ (Fig. 4.1(a)) where (r, ϕ, z) are cylindrical coordinates, which results in a characteristic intensity null along the z-xis (Fig. 4.1(b)).

Recent real-world experiments show that in practical free-space optical communication links the use of OAM modes presents a number of challenges [54, 176, 177]. A prevalent challenge is the mitigation of mode-crosstalk and mode-dependent loss caused by lateral displacement of the OAM modes at the data receiver. Mode-crosstalk and mode-dependent loss are the transfer of energy between spatial modes, and the loss of power of each spatial mode, respectively. Lateral displacement can be caused by motion of the transmitter and receiver platforms as well as atmospheric turbulence. Note that lateral displacement can occur simultaneously with angular error (tip-tilt), i.e., pointing error [178].

However, OAM modes are not the only spatial modes that can be used for free space optical communication [179–183]. The suitability of spatial modes may depend on their symmetry with respect to the free space optical communication link. For example, if rotation of the receiver was predominant then it may be suitable to use OAM modes because they are rotationally symmetric, i.e., they experience less mode-crosstalk and mode-dependent loss when rotated [184]. Yet, for links where lateral displacement is predominant, it may be suitable to use other spatial modes which are more symmetric with lateral displacement, i.e., they experience less mode-crosstalk and mode-dependent loss when laterally displaced. Therefore, it may be of interest to compare the mode-crosstalk and mode-dependent loss of laterally displaced OAM modes with that of other spatial modes.

In this chapter, the mode-crosstalk and mode-dependent loss of laterally displaced OAM modes ($LG_{0,+1}$,$LG_{0,-1}$) are experimentally compared with that of a Hermite-Gaussian (HG) mode subset ($HG_{0,1}$,$HG_{1,0}$). It is shown that for an aperture larger than the modes' waist size, some of the HG modes can experience less mode-crosstalk and mode-dependent loss when laterally displaced along a symmetry axis [93]. It is also shown that over a normal distribution of lateral displacements whose standard deviation is $2\times$ the modes' waist size, on average, the HG modes experience 66% less mode-crosstalk and 17% less mode-dependent loss than the OAM modes.

4.2 Theoretical concept

The intensities ($|HG_{m,n}|^2$) and phase profiles ($\arg[HG_{m,n}]$) of $LG_{0,+1}$, $LG_{0,-1}$, $HG_{0,1}$ and $HG_{1,0}$ are shown in Fig. 4.1.

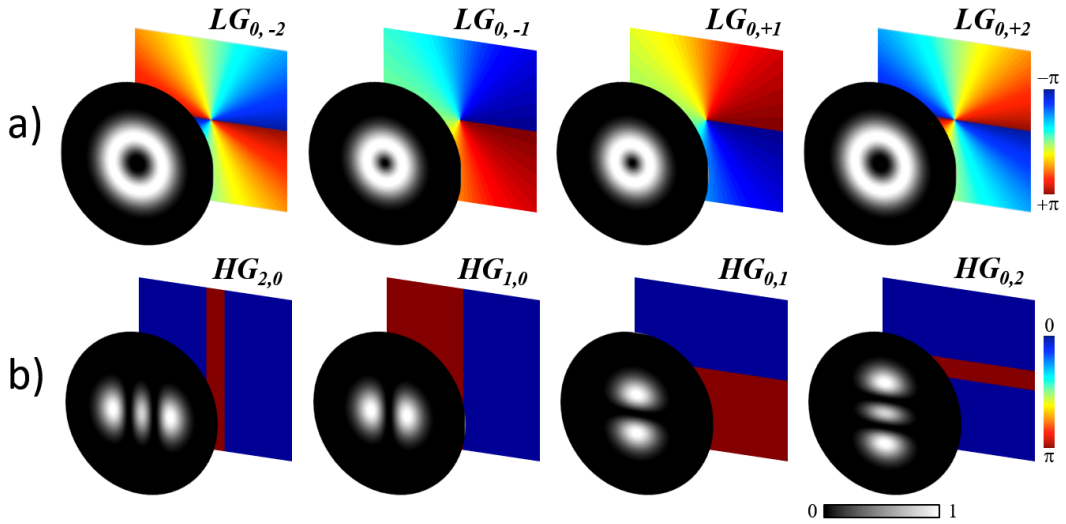


FIGURE 4.1: Intensities ($|HG_{m,n}|^2$) and phase profiles ($\arg[HG_{m,n}]$) of (a) $LG_{0,-2}$, $LG_{0,-1}$, $LG_{0,+1}$, $LG_{0,+2}$ (b) $HG_{2,0}$, $HG_{1,0}$, $HG_{0,1}$ and $HG_{0,2}$.

Consider HG modes that are generated and detected at a data transmitter (Tx) and receiver (Rx), respectively, of a free space optical communication link. They are given by $HG^{in}_{m^{in}n^{in}}$ and $HG^{out}_{m^{out}n^{out}}$, respectively. When the HG modes are laterally displaced at Rx the resulting mode-crosstalk and mode-dependent loss can be mathematically described (without normalization) by an overlap integral:

$$\int_{-\infty}^{+\infty} dx \int_{-\infty}^{+\infty} dy \; HG^{in}_{m^{in}n^{in}}(x,y)\hat{T}(\Delta\vec{r})HG^{out}_{m^{out}n^{out}}(x,y) \tag{4.1}$$

where, $\hat{T}(\Delta\vec{r})$is a displacement operator given by, $\hat{T}(\Delta\vec{r}) = \exp(i\Delta\vec{r}\cdot\hat{p}/\hbar)$ [185]. $\Delta\vec{r} = \Delta x\hat{x} + \Delta y\hat{y}$, $\hat{p} = -i\hbar((\partial/\partial x)\hat{x} + (\partial/\partial y)\hat{y})$, and $\hat{x}$ and $\hat{y}$ are unit vectors in the x and y directions, respectively. The displacement operator as applied in quantum mechanics effects displacements in phase space by transversely shifting the position of the modes from the optical axis of the receiver. The effect of the position displacement operation can be described as

$$\int_{-\infty}^{+\infty} dx \int_{-\infty}^{+\infty} dy \; HG^{in}_{m^{in}n^{in}}(x,y)HG^{out}_{m^{out}n^{out}}(x+\Delta x, y+\Delta y) \tag{4.2}$$

Now, consider a subset of HG modes given by $\{HG_{m,0}, HG_{0,n}\}$. $HG_{2,0}$, $HG_{1,0}$, $HG_{0,1}$ and $HG_{0,2}$ of this subset are shown in Fig. 4.1(b). For this subset, the arguments of the Hermite polynomials, $\arg[H_{m,0}(x)]$ and $\arg[H_{0,n}(y)]$, i.e., the phase profiles of the HG modes, are eigenfunctions of the displacement operators $\hat{T}(\Delta x\hat{x})$ and $\hat{T}(\Delta y\hat{y})$,

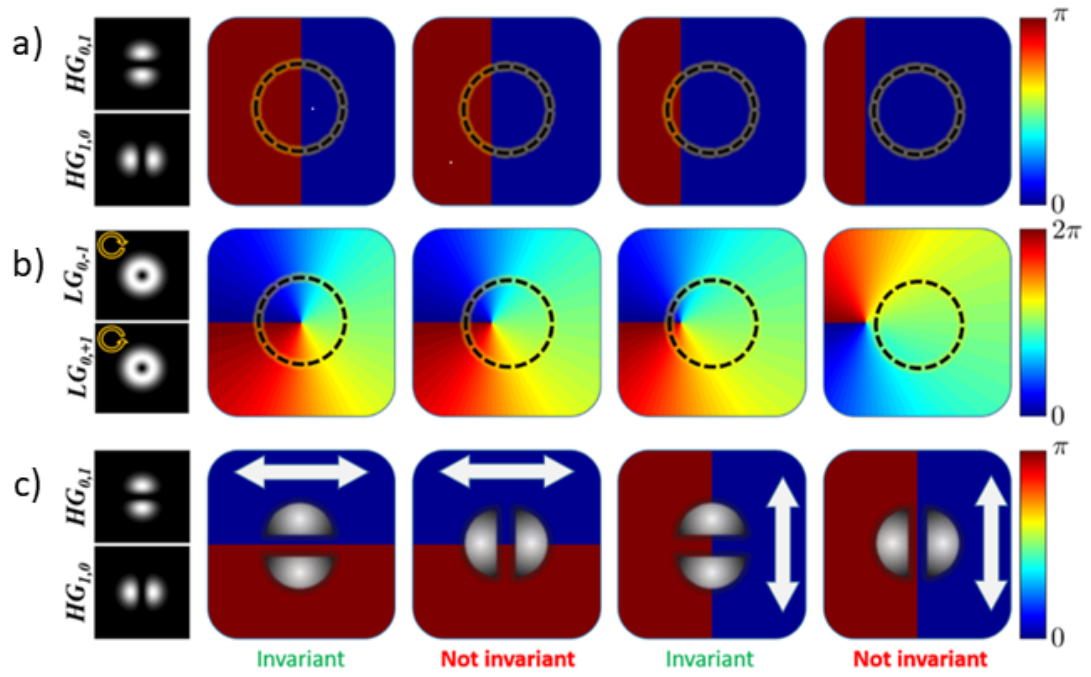


FIGURE 4.2: (a) Schematic illustration of lateral displacement along x-direction of phase profile of $HG_{1,0}$ (b) Schematic illustration of lateral displacement along x-direction of phase profile of $LG_{0,+1}$ (c) Schematic illustration of emulation of lateral displacement of reference frame of CGH at Rx. Lateral displacement along HG modes' axes of symmetry modes are indicated by white arrows.

respectively. These displacement operators laterally displaced the corresponding HG modes along directions corresponding to the HG modes' axes of symmetry. In principle, the phase profile of the modes is expected to change when laterally displaced along their axes of symmetry. Mathematically, this is given by the equations:

$$\hat{T}(\Delta x\hat{x})\arg[H_{m0}(x)] = \arg[H_{m0}(x+\Delta x)], \tag{4.3}$$

$$\hat{T}(\Delta y\hat{y})\arg[H_{0n}(y)] = \arg[H_{0n}(y+\Delta y)]. \tag{4.4}$$

Therefore, for this subset of HG modes, the overlap integral of Eq. 4.1 will be zero for some HG modes when laterally displaced in some directions. As a result, when laterally displaced, this subset of HG modes may experience less mode-crosstalk and mode-dependent loss than OAM modes.

A schematic illustration of this for $HG_{1,0}$ is shown in Fig. 4.2(a). As can be seen, $\arg[HG_{1,0}]$ changes when $HG_{1,0}$ is laterally displaced along the x-direction. However, conversely, while not shown, if $HG_{0,1}$ is laterally displaced along the x-direction, $\arg[HG_{0,1}]$ does not change. As shown in Fig. 4.2(b), this contrasts the lateral displacement of, for example, $LG_{0,+1}$ along any direction. This is of course within the physical

bounds of the detection aperture; as a result of beam divergence, apertures smaller than the spatial modes' waist sizes cause power loss in the spatial mode measured [186]. Here, it is assumed that the aperture is much larger than the spatial modes' waist sizes. The dashed circles in Fig. 4.2(a) and (b) schematically represent the sizes of the generated modes.

4.3 Experimental implementation

4.3.1 Experimental setup

The experimental setup to demonstrate the concept is shown in Fig. 4.3. The fundamental mode of a laser ($\lambda \sim 532$ nm) was expanded, collimated and, made to illuminate one half of a phase only (0-2π) liquid crystal on silicon spatial light modulator (SLM) which, served as Tx. HG and OAM modes were generated using complex amplitude modulation [81], i.e., computer generated holograms (CGHs) comprising the amplitude and phase profiles of the HG and OAM modes were displayed on that half of the SLM. Then, using a $4f$ imaging system comprising two lenses (L1 and L2), the generated spatial modes were imaged onto the other half of the SLM which, served as Rx. Using a lens (L3) and a camera, the HG and OAM modes were detected using modal decomposition [81], i.e., CGHs comprising only the phase profiles of the HG and OAM modes were displayed on that half of the SLM. Note that for the subset of HG modes, the CGHs are phase-only filters being, binary approximations to the Hermite polynomials. To emulate lateral displacement of the spatial modes at Rx, the reference frame of the CGH at Rx was laterally displaced as schematically shown in Fig. 4.2(c).

4.3.2 Results and discussion

Using the experimental setup described above, the mode-crosstalk between and, the mode-dependent loss of HG_{10} and HG_{01} and, that of $LG_{0,-1}$ and $LG_{0,+1}$ were measured as a function of lateral displacement in the x-direction. The results are shown in Fig. 4.4. Mode-crosstalk and mode-dependent loss are given, respectively, by the equations:

$$\mathcal{C}_i = 1 - \frac{S_i}{\sum_j S_j}, \tag{4.5}$$

$$\mathcal{L}_i = 1 - \frac{S_i}{S_0}, \tag{4.6}$$

where, S_i is the power measured in mode i, $\sum_j S_j$ is the power measured in all modes j when transmitting mode i and, S_0 is the power measured in mode i for no lateral

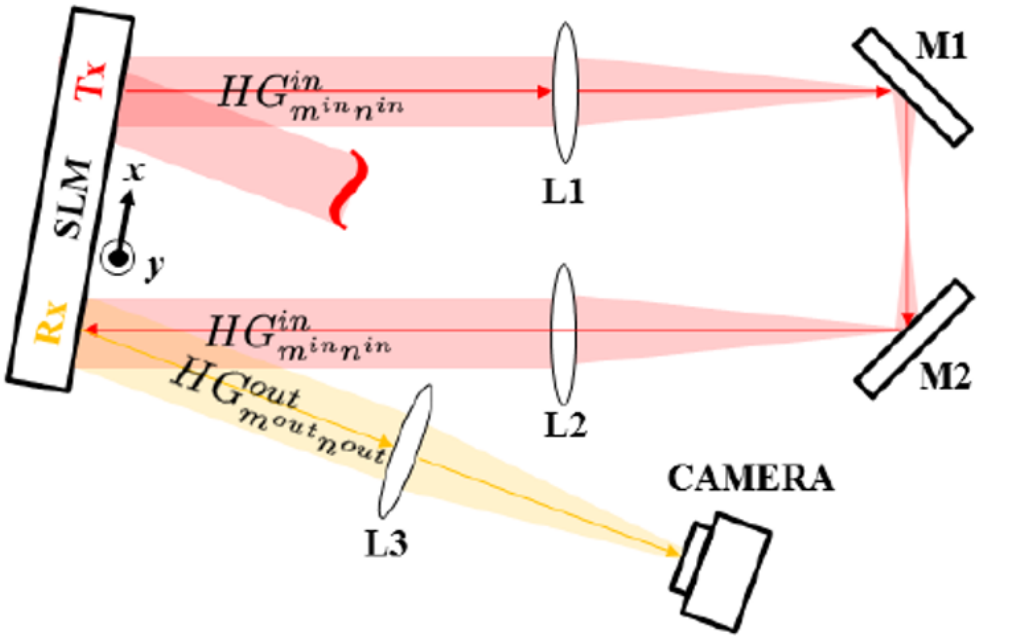


FIGURE 4.3: Experimental setup as described in the text. A collimated green laser source was expanded and illuminated on half of the SLM (Tx) to generate the HG and LG modes. A 4 f imaging system is then used to image the generated modes to the other half of the SLM (Rx) to allow detection measurements.

displacement. Comparison of HG_{10} and HG_{01} with $LG_{0,-1}$ and $LG_{0,+1}$ is 'fair' because, they have the same beam propagation factors (M^2).

As shown in Fig. 4.4(a), as lateral displacement increases, HG_{01} experiences a mode-dependent loss that is independent of lateral displacement and, less than that of HG_{10}, $LG_{0,-1}$ and $LG_{0,+1}$. This is in accordance with Eqs. 4.1 and 4.4. In principle, one would expect the mode-dependent loss to be zero. The small fluctuations observed are attributed to variation in background noise levels.

With regards to mode-crosstalk, the expectation was that HG_{10} and HG_{01} would not experience mode-crosstalk while, $LG_{0,-1}$ and $LG_{0,+1}$ would. As shown in Fig. 4.4(b), there is no mode-crosstalk from HG_{01} to HG_{10} while, the reverse statement is not true. However, this does not contradict Eqs. 4.1 and 4.4. It is believed that the non-zero mode-crosstalk is due to background noise. For a system with relatively good signal-to-noise ratio, for zero lateral displacement, $\sum_j S_j \approx S_i$. However, as lateral displacement increases, mode-dependent loss increases and, in turn, the signal becomes comparable to the noise, i.e., $\sum_{j\neq i} S_j \sim S_i$. As a consequence, the ratio on the right-hand side of Eq. 4.5 decreases, resulting in $\mathcal{C}$ increasing.

In recent real-world experiments of practical free-space optical communication links, it

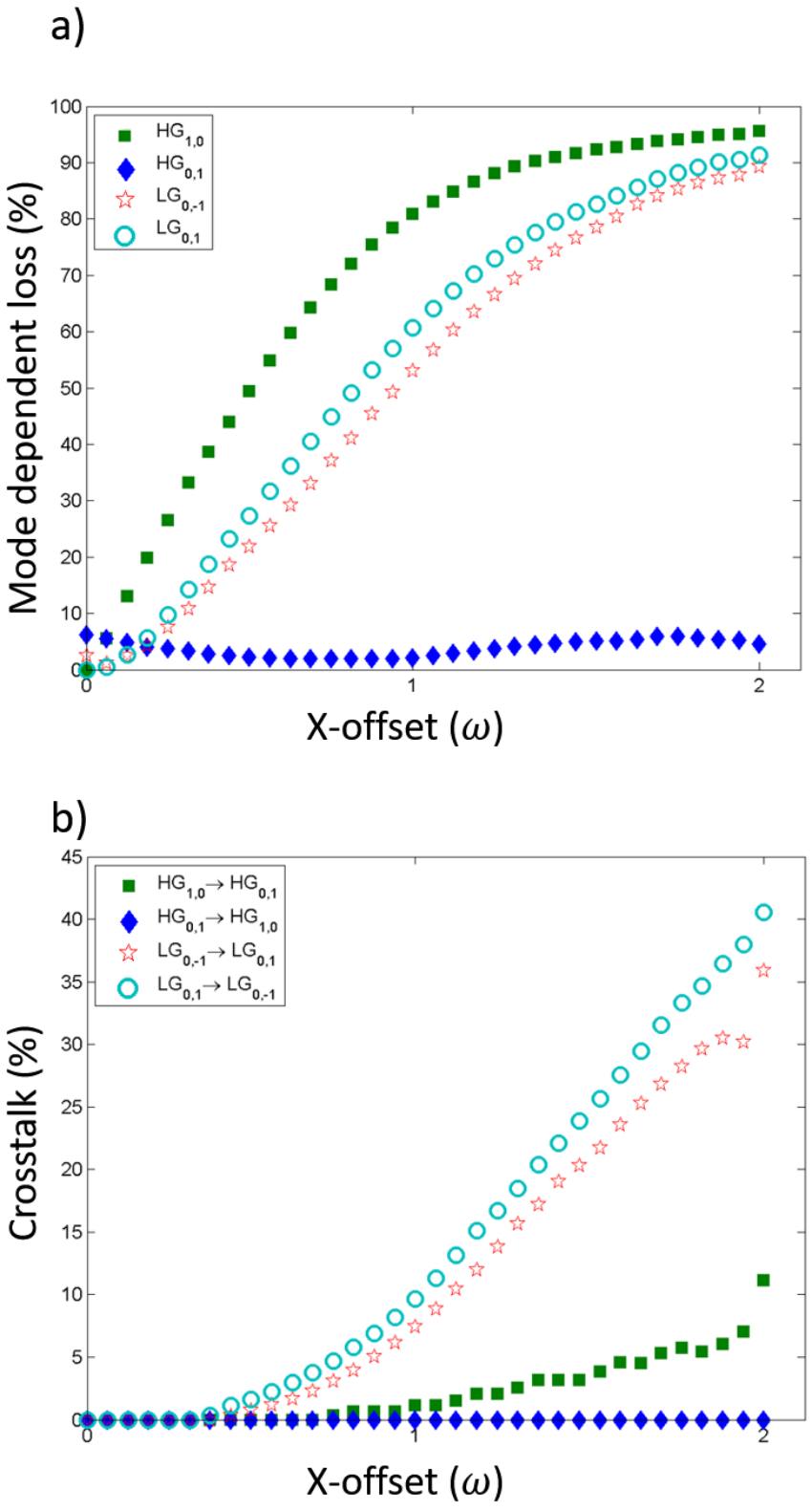


FIGURE 4.4: (a) Experimentally measured mode-dependent loss of HG_{10} and HG_{01} and, $LG_{0,-1}$ and $LG_{0,+1}$ as a function of lateral displacement along the x-direction (X-offset) in units of waist size (ω) (b) Experimentally measured mode-crosstalk between HG_{10} and HG_{01} and, between $LG_{0,-1}$ and $LG_{0,+1}$ as a function of lateral displacement along the x-direction (X-offset) in units of waist size (ω).

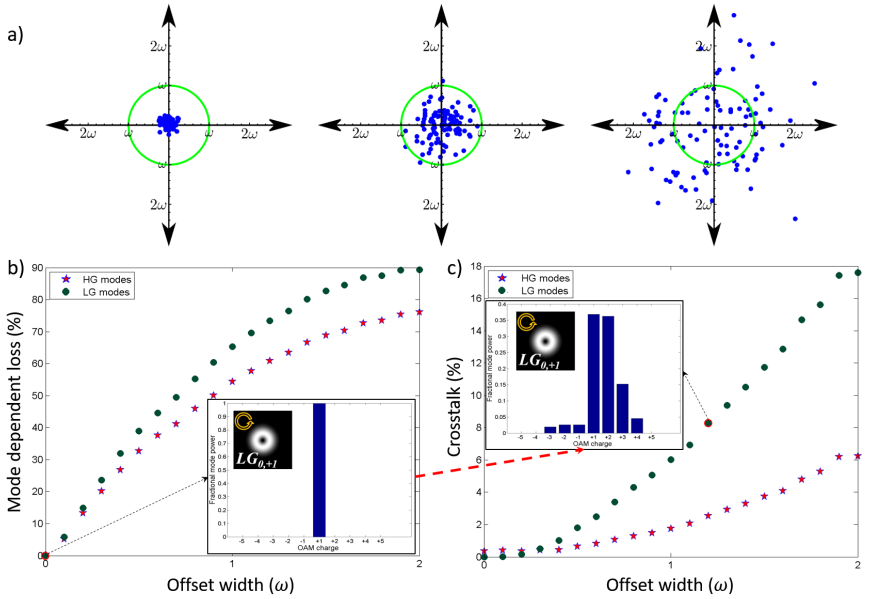


FIGURE 4.5: (a) Random lateral displacements of OAM and HG modes as denoted by blue points. Sizes of OAM and HG modes denoted by green circle (b) Experimentally measured mode-dependent loss (c) Experimentally measured mode-crosstalk averaged over 50 random lateral displacements for each pair of spatial modes as a function of σ.

was shown that OAM modes can experience random lateral displacements in all directions over time [54, 112]. To compare the influence of random lateral displacements on the mode-crosstalk between and, the mode-dependent loss of HG_{10} and HG_{01} and, that of $LG_{0,-1}$ and $LG_{0,+1}$, random lateral displacements that had a normal distribution of mean zero and, a standard deviation, given by σ, were emulated. For a given σ, a set of 50 random lateral displacements, given by X, were emulated, such that, $X \sim \mathcal{N}(0, \sigma^2)$ (Fig. 4.5(b) and (c). For each pair of spatial modes, for a given σ, mode-crosstalk and mode-dependent loss were averaged over the 50 random lateral displacements. For each pair of spatial modes, the resulting average mode-crosstalk and mode-dependent loss as a function of σ are plotted in Fig. 4.5(a). As can be seen, HG_{10} and HG_{01} can experience 66% less mode-crosstalk and 17% less mode-dependent loss than $LG_{0,-1}$ and $LG_{0,+1}$ when $\sigma = 2w$.

Interestingly, note that despite significant mode-dependent loss ($> 70\%$), the highest average mode-crosstalk is less than 20% for either pair of spatial modes. That is because mode-crosstalk is normalized with respect to the the powers of the pair. However, there may be mode-crosstalk to spatial modes other than the pair. This is shown in the insets in Figs. 4.5(a) and 4.5(b) for mode-crosstalk between OAM modes from $\ell = -5$ and $\ell = +5$, excluding $\ell = 0$, when receiving a laterally displaced $LG_{0,+1}$. As can be seen, as expected, for $\sigma = 0$, there is no mode-crosstalk. However, for $\sigma \approx 1.3\omega$, there is mode-crosstalk to OAM modes other than $LG_{0,+1}$ and $LG_{0,-1}$. The fractional power difference

between $LG_{0,-1}$ and $LG_{0,+1}$ is relatively high. Hence, the low average crosstalk value of $\sim 8\%$.

4.4 Conclusion

In conclusion, the mode-crosstalk and mode-dependent loss of laterally displaced OAM modes ($LG_{0,+1}$,$LG_{0,-1}$) were experimentally compared with that of a Hermite-Gaussian (HG) mode subset ($HG_{0,1}$,$HG_{1,0}$). It was shown, for an aperture larger than the modes' waist sizes, some of the HG modes can experience less mode-crosstalk and mode-dependent loss when laterally displaced along a symmetry axis. It was also shown, over a normal distribution of lateral displacements whose standard deviation is $2\times$ the modes' waist sizes, on average, the HG modes experienced 66% less mode-crosstalk and 17% less mode-dependent loss.

Note that the results do not contradict those of Restuccia *et al.* [187], who demonstrated that for an aperture that is smaller than the waist sizes, LG modes may have higher information capacity compared to HG modes. Here, it is assumed that the aperture is much larger than the modes' waist sizes.

Chapter 5

Investigating the self-healing of Bessel beams through aberrations and turbulence

This Chapter contains extracts from a publication by Mphuthi, Nokwazi, Roelf Botha, and Andrew Forbes. "Are Bessel beams resilient to aberrations and turbulence?." JOSA A 35, no. 6 (2018): 1021-1027.

5.1 Introduction

Since the seminal theoretical and experimental work on Bessel beams [115, 116], such beams have been extensively studied to date [118, 119, 121, 188–192], having found a myriad of applications from optical trapping [193–196], communication [197–206], quantum studies [207–212], intereferometry [213], microscopy [214, 215] and have even been produced as matter waves [216, 217]. A particular property that has been exploited is the self-healing ability of such beams [120, 218–221]. While it has been known for a long time that this property is not unique to Bessel beams [222–227], they have nevertheless become the defacto test bed for this optical phenomenon.

Traditionally the self-healing ability of such beams has been studied with opaque objects, and the reconstruction has been explained as the interference of unobstructed conical waves [228, 229], as depicted in Fig. 5.1. In this scenario the conical waves by-pass the obstruction, which in turn produces a shadow region. After the shadow region the conical waves again overlap, and by interference reproduce the original Bessel beam, albeit it with less power and over a limited range in both the transverse and propagation planes.

This reconstruction is possible only because the unobstructed conical waves are (for the most part) not influenced by the obstruction, that is, apart from some small diffraction effects, they appear to bypass the obstruction. When the obstruction is transparent, say in the form of an aberrated screen, then clearly this argument does not hold. Despite this, many studies have suggested that Bessel beams are resilient to all obstructions [230], while the literature has mixed conclusions (mostly theoretical) on the resilience of Bessel beams to turbulence [231–236].

In this chapter, we consider this hypothesis both theoretically and experimentally, showing that Bessel beams do not always self-heal from transparent obstructions, and never self-heal from turbulence where the entire beam is affected [237]. Using digital holograms written to a spatial light modulator (SLM), we programme controlled aberrations and study the influence on the self-healing. We find that the scattering always affects the Bessel beams but to a degree that varies with the severity of the aberration. Rather counter-intuitively we show that the effect can be minimised even for strong aberrations. Finally, by combining aberrations to form a simulation of atmospheric turbulence, we show that when the entire beam passes through the screen, as it would in the real-world, that the beam is always perturbed in a manner that is concomitant with the strength of the turbulence. Our results debunk the myth that Bessel beams always self-heal and provide a systematic approach to future studies in this field.

5.2 Theory

The detailed theory in this section was introduced in previous chapters but will be briefly mentioned here for the benefit of the reader. We start by outlining basic literature on the creation and detection of Bessel beams before applying them in the study, We also briefly revisit the technique of creating phase screens using aberrations to perturb the Bessel beams.

5.2.1 Self-healing property of Bessel beams

The ideal Bessel beam is an exact, propagation invariant solution to the Helmholtz equation containing an infinite amount of power. This cannot be realized physically so often approximations of these beams, known as Bessel-Gaussian beams [117], are generated in the laboratory through techniques such annular slits [121, 238, 239], axicons [240–242], holograms [190, 191, 201, 243–246], interferometers [247] and inside laser resonators [248–258]. They are also easily detected using holograms and custom optics

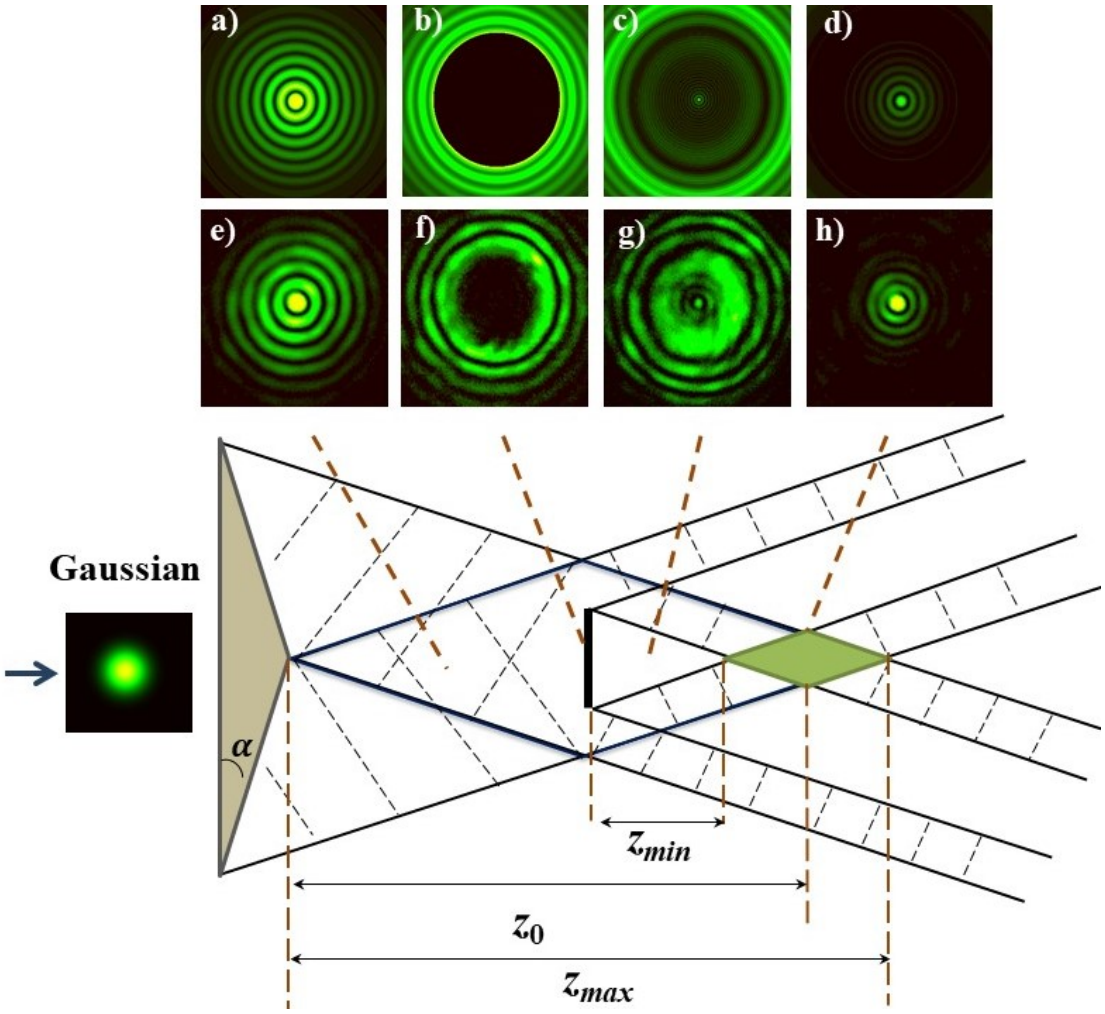


FIGURE 5.1: Self-healing principle of Bessel-Gaussian (BG) beams. Plane waves incident on an axicon of apex angle α are refracted to form conical waves which interfere to form a BG beam in the region $z_{\max}$. An opaque obstruction placed at $\frac{1}{2}z_{\max}$ blocks the waves while allowing unblocked waves to interfere at a short distance behind the obstruction, i.e., after $z_{\min}$. The inset depicts the theoretical profiles (a-e) of the beam at different distances before and after the obstruction together with corresponding experimental images (d-h). The images a and e illustrates the beam just after formation while images b and f illustrates the beam at the obstruction region. The region immediately after the obstruction is illustrated by images c and g while the self-healing region is illustrated by images e and f. The plane z_0 is the region where the beam is expected to self-heal completely.

[191, 201, 259]. At a propagation distance of $z = 0$ the complex amplitude of the Bessel-Gaussian beam can be simplified to take the form:

$$U(r, \phi, z = 0) = J_l(k_r r) \exp\left(\frac{r^2}{w_0^2}\right) \exp(il\phi) \tag{5.1}$$

where J_l denotes the l-th order Bessel function of the first kind, k_r is the radial component of the wavevector with wavenumber $k = \frac{2\pi}{\lambda}$ and w_0 being the waist of the Gaussian beam. The radial and longitudinal wave vectors are related by $k^2 = k_r^2 + k_z^2$. As previously stated, BG beams are geometrically formed by a superposition of coherent plane waves lying on a cone. The principle behind the self-healing property is illustrated in Fig. 5.1, where the conical plane waves are seen to be blocked by an opaque obstruction placed at $\frac{1}{2}z_{max}$. The shadow region, z_{min} depends on the obstruction size. The self-healing occurs behind z_{min}, where the unobstructed plane waves are seen to interfere. We can analytically determine the amplitude of the field transmitted at a particular distance z in free-space by using the known solutions to the wave equation for this function [117], and from the obstruction by using the angular spectrum method or by using suitable geometric approximations [228, 229]. Here, we apply the angular spectrum approach to our numerical simulations. An example of this is shown in the insets of Fig. 5.1 where we show a comparison of the experimental and theoretical self-healing.

5.3 Experimental implementation

5.3.1 Experimental setup

To study the self-healing of BG beams after encountering a transparent obstruction we used the experimental setup outlined in Fig. 5.2. An Argon-ion laser operating at a wavelength of 514 nm was collimated to produce a Gaussian beam of radius $w_0 = 0.6$ mm, which was directed to the SLM (Holoeye PLUTO-2-VIS-056, with 1920 $\times$1080 pixels of pitch 8 μm). The SLM screen was equally divided into two parts, one for the generation of the desired beam and the other for digitally implementing the perturbation (obstruction).

A digital axicon was encoded on the first half of the SLM for the creation of the BG beam while the obstruction side was encoded with aberration masks of a desired radius, or finally the turbulence phase mask. The obstruction in the shape of disk was placed at an effective distance of $\frac{1}{2}z_{max}$ (by imaging the created beam to this plane) to ensure that the obstruction was at the centre of the Bessel region. The diameter of the obstruction was chosen to be $\frac{2}{3}w_0$, corresponding to the chosen Zernike unit circle. This was to

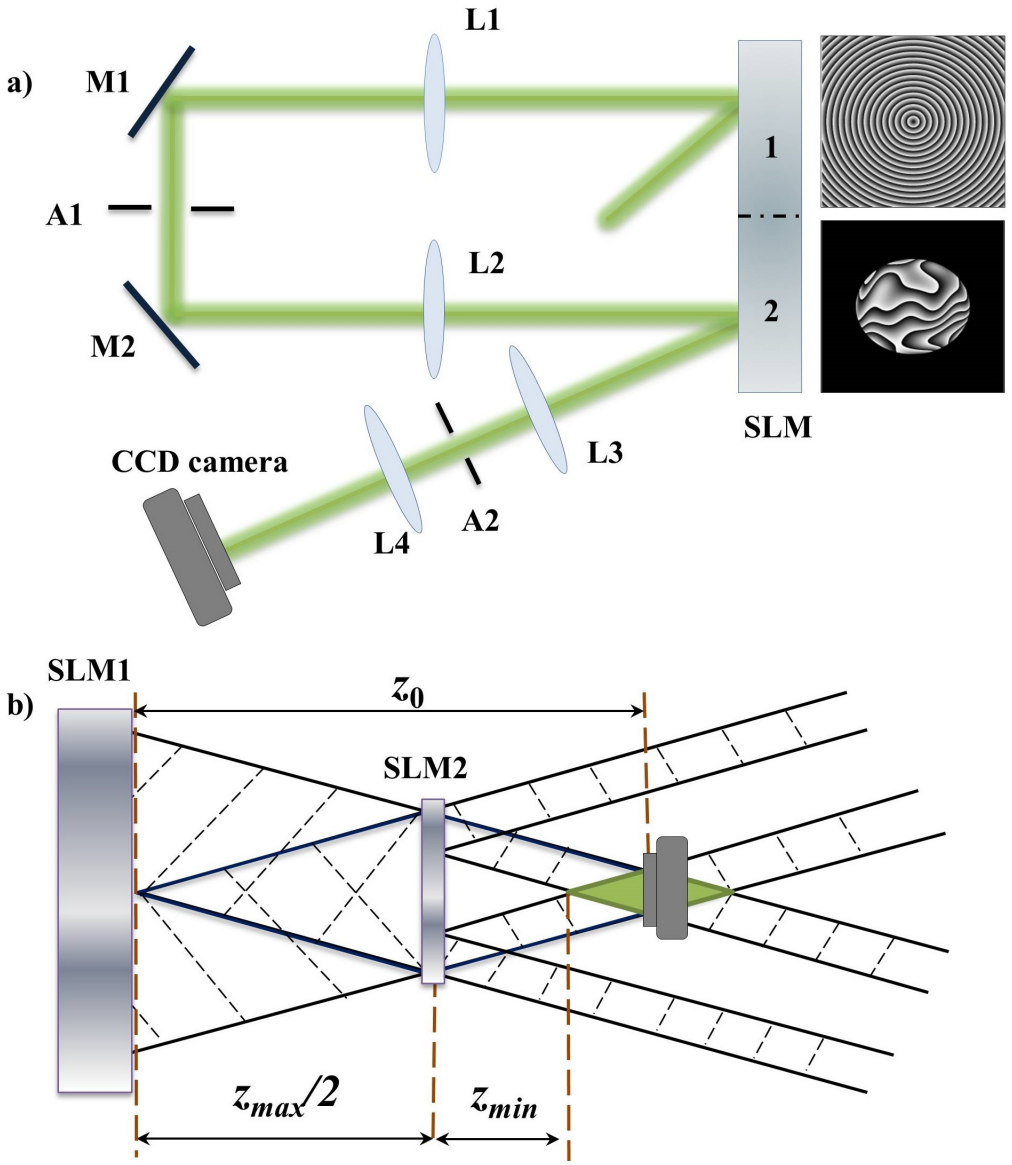


FIGURE 5.2: (a) Schematic of the experimental setup used to study the self-healing of BG beams after encountering a phase-changing obstruction. A collimated Argon-ion laser source is used to generate a BG from an axicon encoded on one half of the SLM screen (labelled as 1) while the second half (labelled as 2) was encoded with the obstruction. The distance between SLM1 and SLM2 was $\frac{1}{2}z_{max}$, thereby placing the obstruction in the middle of z_{max}. (b) A conceptual illustration of the core optical planes, showing the position of the two phase screens of the SLM.

ensure that the polynomials remain valid over the definition radius. Aperture A1 was placed at the focal plane of L2 ($f = 200$ mm) to ensure that only the desired first order was imaged onto second part of the SLM. The resulting beam was allowed to propagate and the self-healing observed at different propagation distances after the obstruction by detection on a CCD camera (PointGrey), with most measurements to be reported at the distance $z = z_0$ as shown in Fig. 5.2. A blazed grating was applied to all masks in order to separate the desired first diffraction order from the others, which were filtered by Lenses L3 and L4 ($f = 250$ mm) together with an aperture.

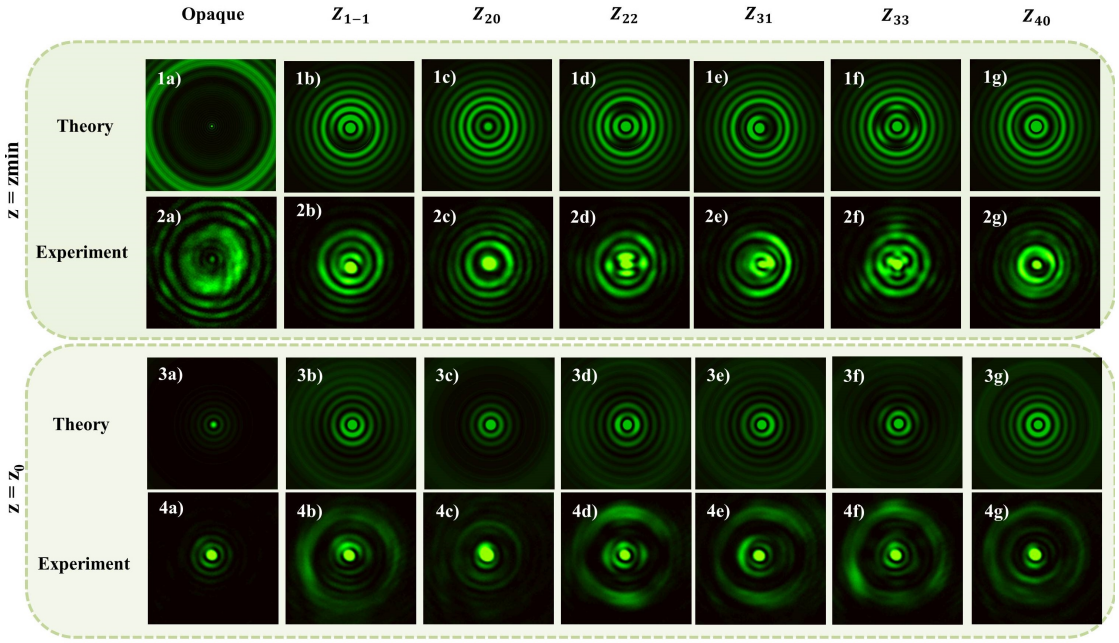


FIGURE 5.3: Theoretical and experimental images depicting the evolution of the BG beam after encountering different aberrations.The columns (a-g) represent different obstructions while the rows represent different observation planes within zmax. Column (a) depicts the reference case of an opaque disk obstruction, while columns (b,c,d,e,f and g) depict tilt, defocus, astigmatism, coma, trefoil and spherical aberrations with a magnitude coefficient of unity ($a_{n,m} = 1$) respectively. Rows 1 (theoretical) and 2 (experimental) illustrates the influence of the obstruction at the shadow region(zmin),while row 3 (theoretical) and 4 (experimental) illustrates how the beam has evolved at the self-healing region(z_0).

5.3.2 Aberration results

Fig 5.3 depicts some examples of the evolution of the beam after encountering various primary aberrations, where the first two rows display the beam at the shadow region and the last two rows display the self-healing region, along with their corresponding theoretical predictions. Measurements were first taken for the reference case of an opaque obstruction and shown in column 1. As expected, the beam is seen to self-heal at z_0, where the beam regenerates a certain portion of its initial intensity profile. This is in

agreement with previous analytical predictions which have stated that the beam will not reconstruct to its initial size [225].

To investigate phase perturbations, aberrations were encoded inside the obstruction and the effect on the resulting self-healing observed at both the z_{min} and z_0 planes and shown in Fig. 5.3. In this case, the disturbance of the beam due to the aberrations is more evident at the shadow region for all aberrations types. For the case of tilt (Z_{1-1}), the beam centroid is seen to be laterally displaced in the vertical direction and is still evident at the self-healing region. Not surprisingly, we find that the aberration type influences the manner of the self-healing and visually it appears that the asymmetric aberrations have a more pronounced affect on the ability to self-heal. For example, the triangular pattern due to trefoil (Z_{33}) remains distinctive even at z_0.

To investigate how the strength of a given aberration influences the self-healing property, we performed a correlation of the perturbed and unperturbed intensity profiles at the self-healing plane ($z = z_0$) as a function of the aberration strength, with the results shown in Fig. 5.4 for astigmatism, trefoil and spherical aberrations. The aberration strength is quantified as the variance or the coefficient of the aberrations. These aberrations were chosen as representations of even, odd and radial aberrations, respectively.

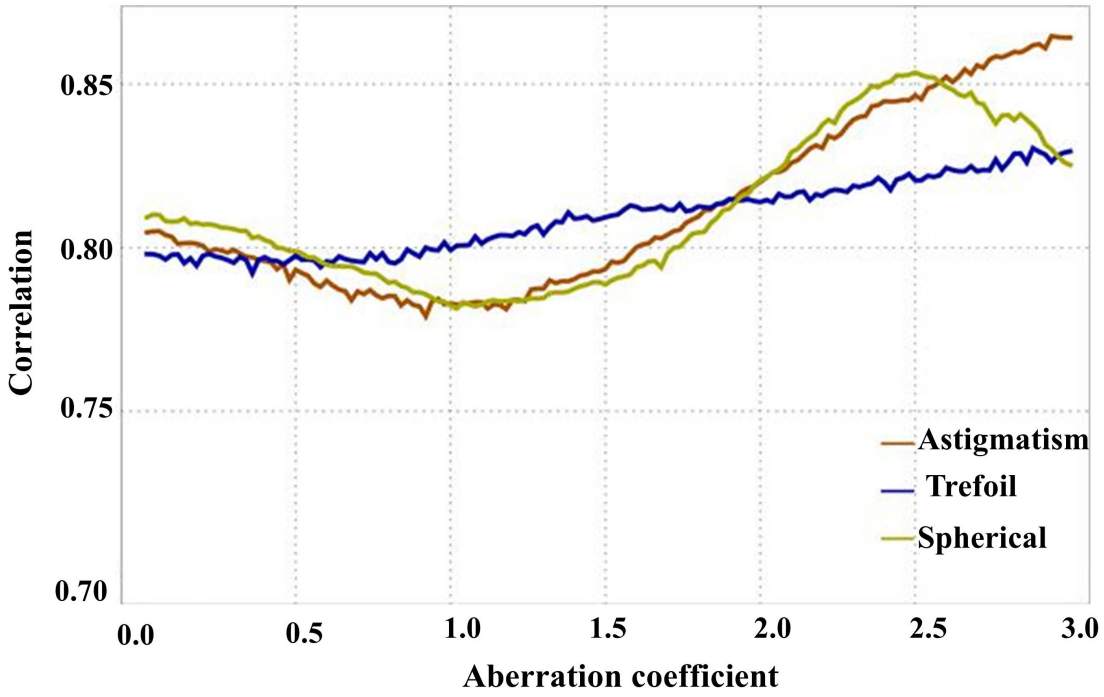


FIGURE 5.4: Correlation of the perturbed beam against a reference unperturbed beam at the plane $z = z_0$, plotted as a function of aberration strength, for odd and even aberrations as well as aberrations with no azimuthal dependence(ie m=0).

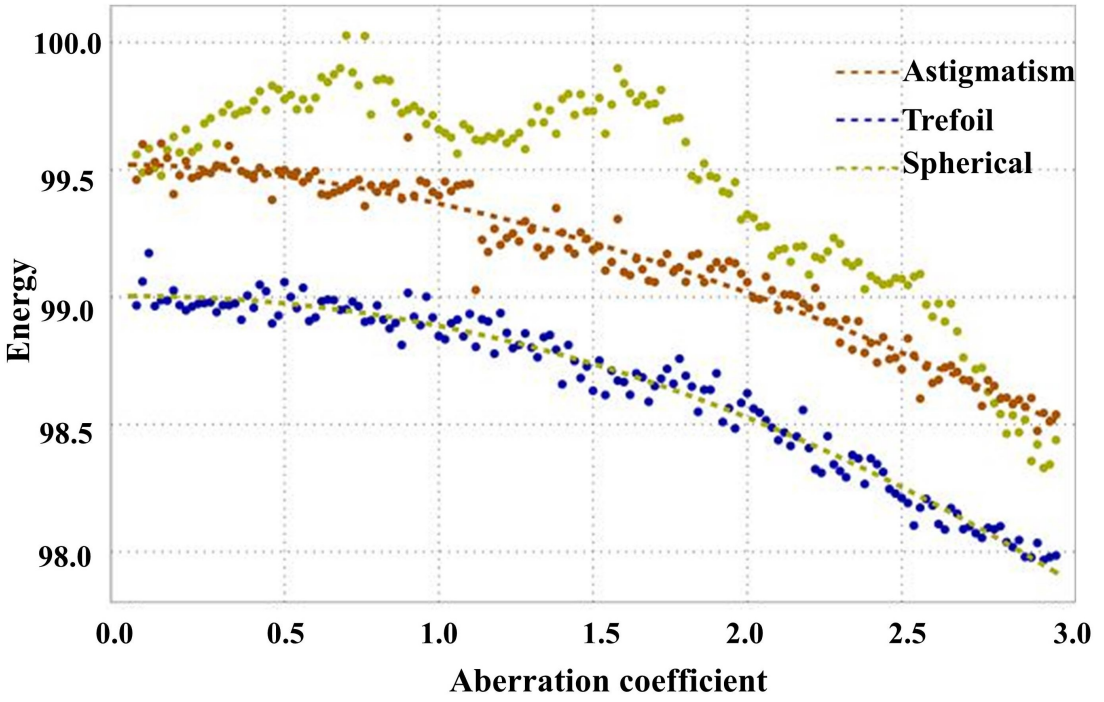


FIGURE 5.5: Relationship between beam energy and aberration strength. The measurements are shown for astigmatism, trefoil and spherical aberrations for the same aberration strengths as Figure. 5.4. It is clear that energy decreases with an increase in aberration strength for all the displayed aberrations. The dotted lines are estimated based on a least-squared fit on the measurements.

Intensity correlations serve as a measure of beam quality with values between 0 and 1, denoting poor and high beam quality respectively. In this case, a high quality beam is expected for an undisturbed beam while poor quality will characterise a beam so greatly disturbed that it no longer resembles the reference beam. Initially, with no aberrations programmed, the beam is unperturbed. As aberrations are introduced, the beam quality begins to deteriorate as demonstrated by the declining correlation values in Fig. 5.4. This decline is a result of the aberration distorting the conical waves, thereby prohibiting full reconstruction. Intriguingly, after aberration strengths of 1 and above (by coefficient value), an improvement in the self-healing is noted, where the beam quality starts to increase and thereafter converging for higher coefficients. One can understand this result by observing Fig. 5.5, which illustrates the relationship between peak energy and aberration strength at the plane $z = z_0$. From this it can be seen that the peak energy decreases as the aberration strength increases. This decrease in energy can be attributed to diffraction spreading that occurs as the aberration strength is increased, similar to scattering. Diffraction redistributes the energy outwardly away from the beam centroid where conical reconstruction occurs. This effect is graphically illustrated in Fig. 5.6, where diffraction effects are seen to increase with trefoil aberration strength.

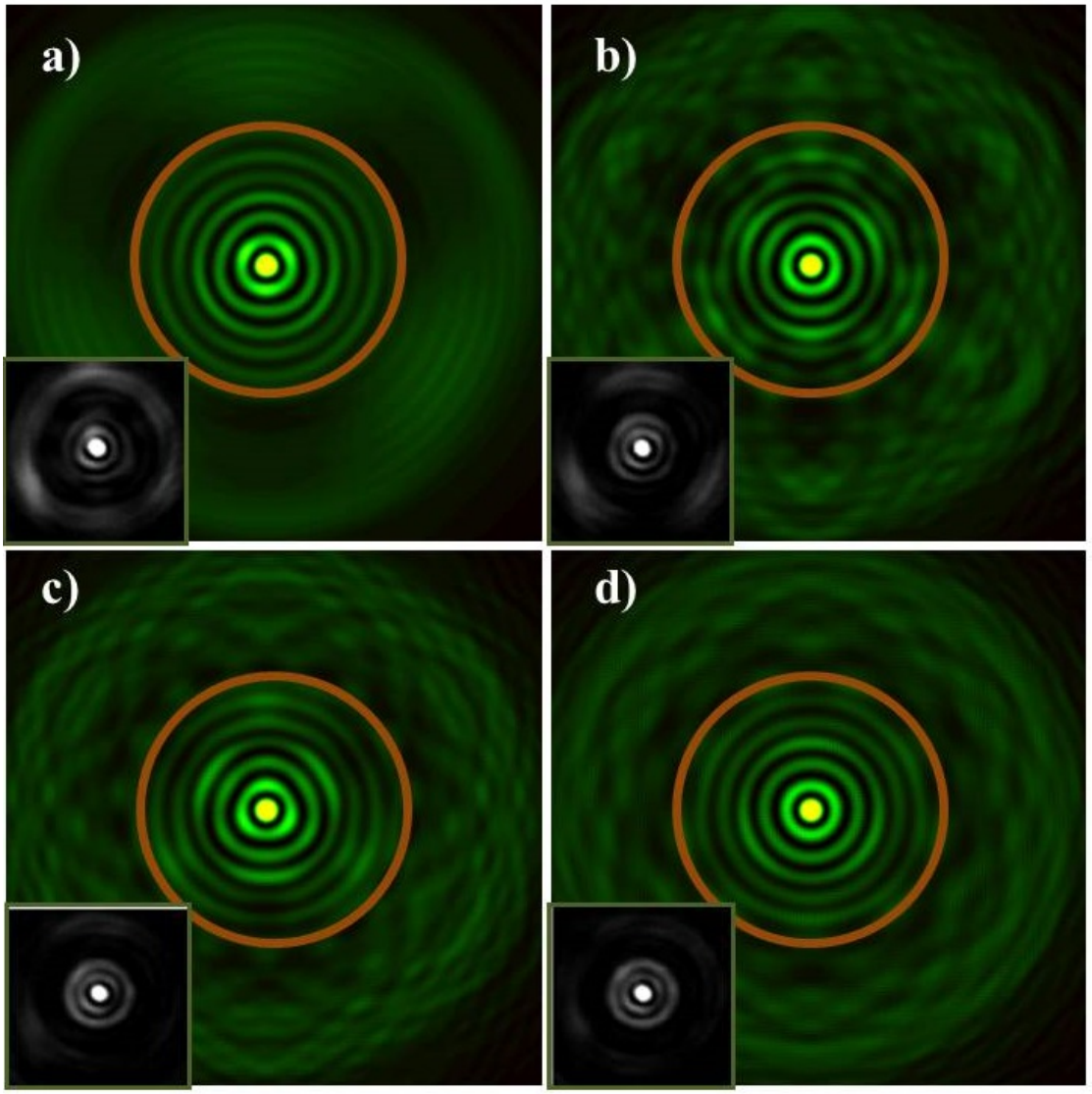


FIGURE 5.6: Theoretical and experimental(insets) images of Bessel beams at the self-healing plane after encountering trefoil of magnitude, $a_{3,3}$, of (a) 1, (b) 5, (c) 10 and (d) 20. The circles indicate the region of the beam visible to the detector. self-healing is seen to improve with increasing aberration strength around the centre of the beam.

The diffraction effects outside the circles increase with aberration strength but the quality of the beam inside the circle is seen to improve. It is therefore evident that the greater the distortion, the more the beam seems to be diffracted. This is because large aberrations will cause significant deviations from a spherical wavefront, thereby causing the beam to spread, consequently weakening the detectable overlap with the original unperturbed conical waves. The result is the illusion of a weak aberration acting on the beam.

5.3.3 Turbulence results

The turbulence phase screens were created by summing the weighted aberrations as described in section 3.3. Rather than disturbing a small part of the beam, the turbulence was encoded to disturb the entire beam as would be the case in a real atmospheric propagation. The strength of the turbulence is denoted as the normalised coefficient D/r_0, with large values indicating strong turbulence. In Fig. 5.7 we show the results of the beam initially and at the self-healing plane for D/r_0 values of 3, 10 and 20, representing weak, moderate and strong turbulence, respectively. In all these cases one finds that the beam is seen to deteriorate with propagation distance concomitant with the strength of the turbulence, i.e., no self-healing at all, which can be understood from the fact that all conical waves are disturbed and so there is no by-passing of the "obstacle".

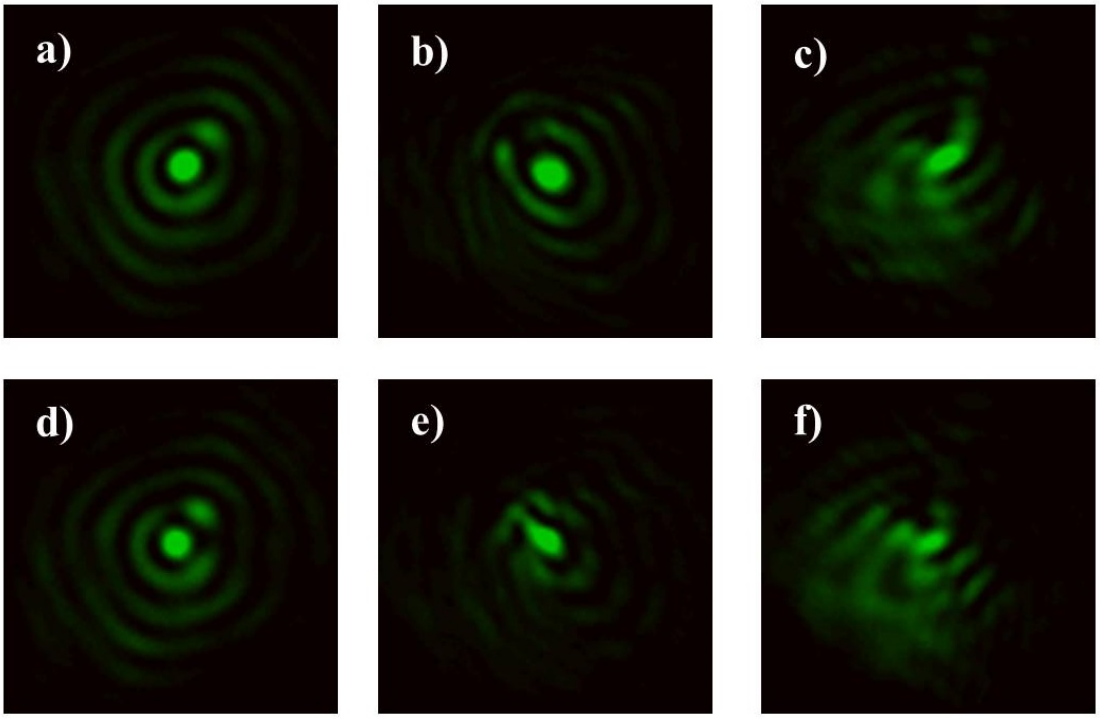


FIGURE 5.7: Experimental images of the BG beams after encountering turbulence. (a) - (c) shows the BG beam immediately behind the turbulence screen while (d) - (f) shows the BG beam at $z = z_0$. In all plots the turbulence increases from left to right with D/r_0 values of 3, 10 and 20.

5.4 Discussion

It is undeniable that Bessel beams present certain advantages over other beam types used in free-space optical communications, in terms of power delivery [233, 235] and

individual channel efficiency [236]. However, in order to claim resilience through phase perturbations, the Bessel beam has to self-heal after encountering random phase errors. The self-healing aspect can be demonstrated in the form of intensity similarity checks between the beam before and after a disturbance has occurred. It is visually evident from Figure 5.3 that obstructions in the form aberrations do not lead to absolute self-healing as remnants of the disturbance are seen at the self -healing region. This result clearly contradicts [230] which claim that Bessel beams are able to self-heal after encountering phase disruptions. The discrepancies can be attributed to the form and size of the obstruction used. In [230] the obstruction is a combination an amplitude and a phase obstacle of minute size ($d = 4.8/k_r$). In this case, the conical waves blocked by the amplitude part of the obstacle do not get to interact with the phase-changing obstacle. Instead, what is seen behind the obstacle is a hollow centre as a result of the opaque disk with no influence from the phase perturbation. The influence of the phase object only becomes noticeable after further propagation where there is interference of the undisturbed plane waves with the phase obstacle. The self-healing therefore occurs as a result of the amplitude perturbation introduced before the phase object. However, in our study, where the size of the obstacle is significantly larger and the disturbance is only phase-changing, we see that self-healing of the BG beam is not always guaranteed.

The self-healing process has always been based on the intuition that undisturbed conical waves will interfere to reform the BG beam. This has previously been demonstrated for opaque obstructions of finite size, but here we show that this is not in general true for arbitrary phase obstructions. As a caveat we note that the influence of an aberration on the resulting beam is an interplay between the aberration strength and the distance at which the observation takes place, where under some conditions it is possible for the self-healing to again improve with an increase in the aberration. We have also shown that it is impossible for the beam to self-heal when the disturbance covers the entire beam, as is the case with turbulence. Here the beam is seen to deteriorate with propagation distance. It is important to note that this does not necessarily contradict previous work in [232] and [234] which have demonstrated the resilience of partially coherent and Hankel- Bessel beams. The concept of resilience in those cases, refers to the rate at which the beam quality factor degrades as well as the beam's ability to focus in turbulence channels. The aforementioned merits do not extend to the self-healing aspect when the beam is subjected to phase errors. Despite this realization, obstructed Bessel beams can still be efficiently utilised for optical communication and imaging applications as the lost information can be recovered, even after significant distortions. This was demonstrated for obstructed pulsed Bessel beams , using adapted image-processing procedures to restore losses in contrast and spatial frequencies [260].

5.5 Conclusion

In this chapter, we have shown that the notion of Bessel beam self-healing under phase perturbations does not always hold true. This has been demonstrated by disturbing a BG beam with transparent obstructions in the form of Zernike aberrations. We have shown that in such a case, the influence of the perturbation is noticeable both in the shadow and self-healing regions, therefore we cannot affirm complete self-healing as in the case with opaque obstructions. On the other hand, we can reduce the effects of the aberrations by scattering the aberrated energy to the outskirts of the beam in order to minimize its influence on the beam seen by the detector. Moreover, when the entire beam is disturbed, as in real life atmospheric turbulence, no self-healing can occur. All impinging conical waves become disturbed, diminishing any chance of self-healing. Therefore, contrary to some suggestions, Bessel beams are not resilient to atmospheric turbulence. In addition to spatial self-reconstruction, this study can be extended to investigate spatio-temporal self-reconstruction of pulsed Bessel beams obstructed by dispersive obstacles to illustrate the same concept.

Chapter 6

Propagation of shape-invariant Bessel beams through real world turbulence

This Chapter contains extracts from a publication by Mphuthi, Nokwazi, Lucas Gailele, Igor Litvin, Angela Dudley, Roelf Botha, and Andrew Forbes. "Free-space optical communication link with shape-invariant orbital angular momentum Bessel beams." Applied Optics 58, no. 16 (2019): 4258-4264.

6.1 Introduction

The transmission of data through multiple independent channels has gone a long way into alleviating the ever-increasing data traffic in modern telecommunication networks [261, 262]. By utilizing independent properties of light, such as wavelength, polarisation and spatial profile as carriers of information, we are able to improve data bandwidth and channel capacity in free-space optical communication systems. While it is established that OAM modes are not the only spatial modes which can be utilized for free-space optical communication, they however remain the mode of choice for many Mode Division Multiplexing (MDM) links, reaching up to terabit capacity in the last decade [55, 175, 263, 264]. Now OAM needs a carrier radial mode, a fact often ignored in the creation of OAM beams (traditionally created by modulating a Gaussian mode with a helical phase). Radial mode control of OAM modes can be accomplished with the full Laguerre-Gaussian mode set or the Bessel-Gaussian mode set. The properties of Bessel beams makes them a interesting mode of choice for free-space optical communication applications [183, 198–200, 236, 265, 266]. The limitation of these beams mainly lies in the fact that they are

diffraction-free for a limited propagation distance, thereafter becoming an annular ring. The lack of shape-invariance, changing from a Bessel structure to an annular ring, is a major drawback for long-range applications such as free-space optical communications. This can be overcome by using long range Bessel beams that are shape invariant during propagation [267]. These beams have longitudinally dependent cone angles which allow the Bessel-like shape to be preserved as the beam propagates, can easily be created in a single hologram and posses self-healing abilities as usual Bessel beams [268].

Here we experimentally create these beams with Spatial Light Modulators, imbue them with OAM, and then apply them to an optical communication link in free-space. We investigate the effects of atmospheric turbulence on modal cross-talk under a variety of real-world conditions across our 150 m link. In the presence of turbulence, the OAM spectrum is known to spread [53, 269–273], which we study here with Bessel-like OAM beams. We characterize the link performance and in particular the turbulence strength under different weather conditions and various times of day. Our results show successful generation and detection of shape-invariant Bessel beams across a free-space link with turbulence-induced cross-talk.

6.2 Shape-invariant Bessel beams

Here we briefly outline the concept and theory of shape-invariant Bessel-like beams for the benefit of the reader before applying it to our case study. Classical propagating Bessel-Gaussian modes can be described by Eq. 2.4. At a propagation distance $z = 0$, this solution reduces to take the form:

$$U(r, \phi, z = 0) = J_l(\beta r) \exp\left(\frac{r^2}{w_0^2}\right) \exp(il\phi), \tag{6.1}$$

The β factor is given by $\beta = k \sin\theta$, where θ is the angle at which the plane waves interfere as illustrated in Fig. 2.2. By engineering the cone angle to decrease with propagation distance, the depth of focus can be enlarged and the shape of the Bessel beam preserved. Such shape-invariant Bessel beams can be generated by a phase-only approach with a transmission function given by [267]

$$\Phi(r) = \exp[ik(ar^n + br^m)], \tag{6.2}$$

where a, b, n and m are the design parameters of the phase element. By employing the stationary phase approximation we can calculate the cone angles such that the angle

$n = 1$, $m = 2$	$n = 2$, $m = 3$	$n = 1$, $m = 3$
$\alpha_c(z) = \frac{r_1 a}{az - r_1}$	$\alpha_c(z) = \frac{r_1}{12az^2}(1 + 10az + F(a,z))$ $F(a,z) = \sqrt{1 + 20az + 4a^2z^2}$	$\alpha_c(z) = \frac{r_1}{6az^2}(r_1 + 4az + G(a,w,z))$ $G(a,w,z) = \sqrt{r_1^2 + 8ar_1z + 4a^2z^2}$

TABLE 6.1: Solutions for calculating particular cone angles for given n and m values. The cone angles are dependent on the propagation distance z and element parameters a and r_1.

of arrival of the conical waves at any transverse plane is identical and decreases with distance. Mapping rays from a source plane r_0 to some screen plane r_s at some z distance results in an eikonal equation of the form

$$anr_0^{n-1} + bmr_0^{m-1} + \frac{r_0}{z} - \frac{r_s}{z} = 0. \tag{6.3}$$

If the aperture of the optic is denoted as r_1, then the phase element parameters required to generate a Bessel-like beam must satisfy

$$b = -a\left(\frac{n}{m}\right) r_1^{n-m}. \tag{6.4}$$

The general solution to finding the unknown cone angles, α_c, is therefore found from

$$\begin{aligned} &\alpha_c + an(r_1)^{n-m}(z\alpha_c)^{m-1} \\ &+ an(-r_1)^{n-m}(-r_1 + 2z\alpha_c)^{m-1} + (-r_1 + 2z\alpha_c)^{n-1} \\ &- an(z\alpha_c)^{n-1} = 0. \end{aligned} \tag{6.5}$$

Table 6.1 lists cone angle solutions to the most common optical elements with $n = 1$, $m = 2$ (an axicon-lens doublet), $n = 2$, $m = 3$ (aberrated lens) and $n = 1$, $m = 3$ (aberrated axicon). The powers n and m values are arbitrarily chosen and present no significant relevance other than simplicity in the implementation process.

When the aforementioned design procedure is followed the result is a shape-invariant Bessel structure from the near to the far field as demonstrated in Fig. 6.1. This is advantageous for optical communication as the far-field signal near the origin of the beam (where the detector is found) can be made larger than would be the case for a conventional Bessel beam that transforms into an annular ring. However, the drawback is that the Bessel structure is no longer non-diffracting, instead diverging with propagation distance. Upon imparting orbital angular momentum to the beam, we can represent the beam as

$$U(r, \phi, z) = J_l(k\alpha_c(z)r) \exp\left(\frac{r^2}{w_0^2}\right) \exp(il\phi). \tag{6.6}$$

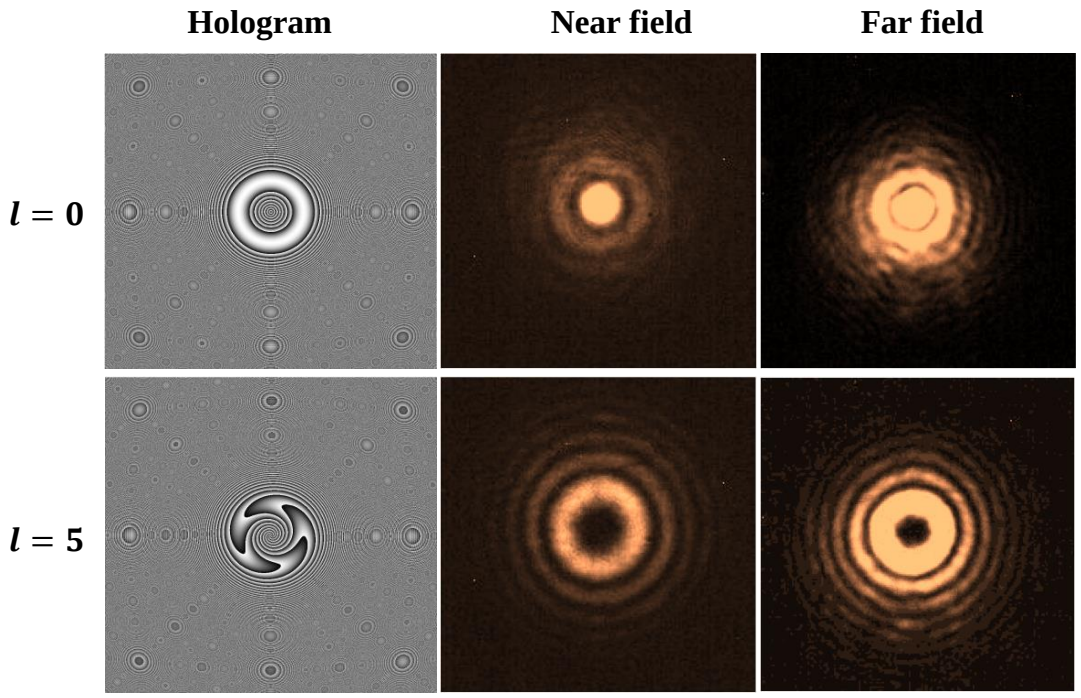


FIGURE 6.1: Holograms for generating zero and high-order shape-invariant Bessel beams with their respective intensity profiles at the near and far-field planes.

Examples of holograms used to generate Bessel-like beams of any order with their resulting intensity profiles are shown in Fig. 6.1. The holograms should be calculated to have grey-scale values ranging from 0 to 2π to allow phase shift modulation by the Spatial Light Modulator (SLM).

6.3 Experimental implementation

6.3.1 Experimental setup

To investigate the feasibility of using shape-invariant Bessel beams for free-space optical communication, we generated and propagated the beam through a real-world 150 m link with atmospheric turbulence, as illustrated in Fig. 6.2. A Gaussian beam of radius $w_0 = 0.8$ mm from a Helium-Neon laser, operating at a wavelength of 632.8 nm, was expanded using lenses L1 ($f = 50$ mm) and L2 ($f = 150$ mm) and incident on a Spatial light Modulator (Holoeye PLUTO, with 1920 $\times$1080 pixels of pitch 8 μm). The SLM was encoded with the phase function given by Eq. 6.2, with parameters chosen as a

= 0.58 μm, $n = 1$, $m = 2$ and $r_1 = 5$ mm. The choice of parameters determines the radial spacing of the rings, otherwise known as the k_r factor in traditional Bessel beams, as well the distance which the beam can propagate. Using lenses L3 and L4, both having a focal length of 100 mm, we filtered the desired first order using an aperture A positioned at the focal length of L3. In order to minimize divergence, a 5× Galilean beam expander was used to increase the beam further to a radius of $w_0 \approx 15$ mm before propagating 75 m in an outdoor link to a retro-reflector located at about 75 m from the lab. The beam was reflected back on the same path to make up a total link distance of $L = 150$ m. A 200 mm concave mirror was used to focus the beam upon its return. The beam was then directed towards a second SLM for detection measurements. The second SLM served as a correlation filter where modal decomposition measurements were performed to measure the modal crosstalk [81]. Modal decomposition allows unravelling of an unknown field into its constitution parts. For higher-order Bessel beams, this means unpacking information contained in both the OAM l and the radial k_r index [190, 191]. The field can be expanded into the basis of angular harmonics, which are orthonormal over the azimuthal plane. The coefficients will determine the amplitude and the intermodal phase of the unknown field relative to other modes. This is done experimentally by programming the conjugate of the mode as the correlation filter. The inner product (on-axis intensity) of the unknown field and the correlation filter, observed at the Fourier plane, reveals the power content of each mode.

6.3.2 Link Characterisation

In any communication link, a link budget analysis is crucial in order to characterise the link under operating conditions. Characterisation is done by quantifying the beam's attenuation as a result of atmospheric, optical and geometric losses. As the beam propagates through the atmosphere, it will incur losses due to atmospheric absorption and scattering, different weather conditions (such as rain) and optical turbulence as a result of beam wandering and scintillation. Absorption and scattering of molecules and aerosols will result in wavelength dependent energy losses, thereby affecting the beam's transmission through the atmosphere. These losses can be calculated from the Kruse model, which takes into account the meteorological visibility parameter V to give a rough estimate of the losses. The Kruse model is given by [274]

$$L_{\text{atm}}[dB/km] = \frac{17}{V}\left(\frac{0.55}{\lambda}\right)^{q}, \tag{6.7}$$

where q is given by

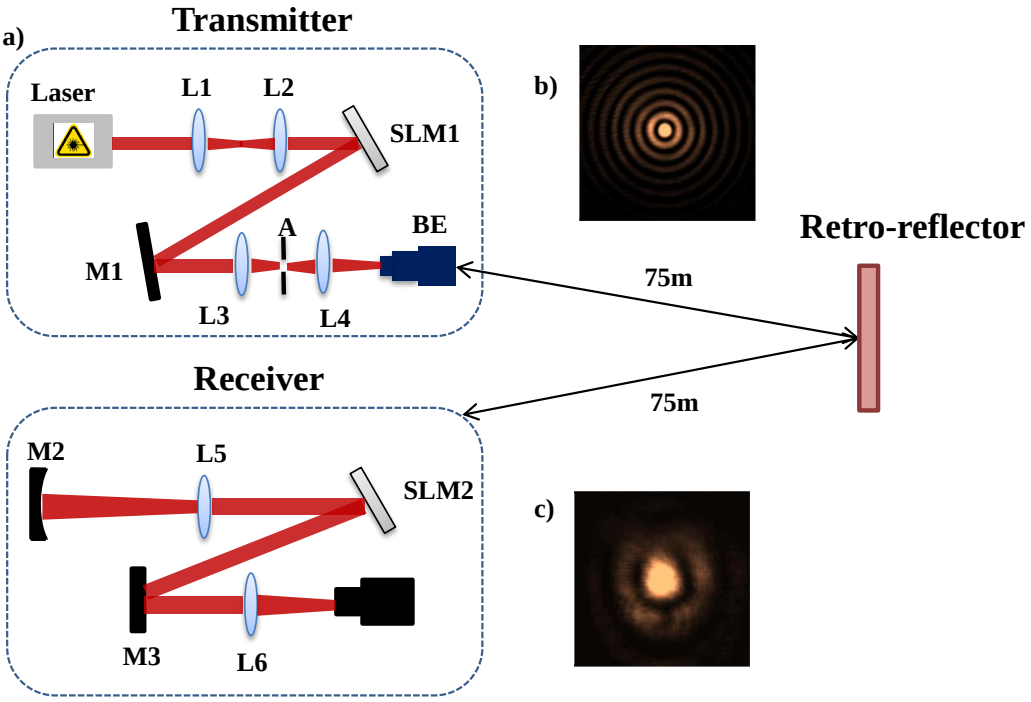


FIGURE 6.2: Experimental setup of the 150 m free-space link used to generate and measure shape-invariant Bessel beams. a) An expanded HeNe laser source illuminates an SLM encoded with a phase-only element to generate the beam. The beam is propagated through real turbulence, reflected off a retro-reflector back to a measuring SLM encoded with de-multiplexing holograms. The intensity profile of the beam before it leaves and when it returns are depicted in b) and c) respectively.

$$q = \begin{cases} 1.6 & \text{if } V > 50km \\ 1.3 & \text{if } 6 < V < 50 \\ 0.585V^{\frac{1}{3}} & \text{if } V < 6 \end{cases}$$

and λ is the wavelength in nm

The site location where the experiment was conducted often sees rainy weather conditions. Rain induces losses independent of wavelength in optical communication systems. The modelling of rain attenuation is mainly done by empirical methods. The model is given by [275]

$$L_{\text{rain}}[dB/km] = k_1 R^{k_2}, \tag{6.8}$$

where R is the rainfall rate measured in mm/hr and k_1 and k_2 are constants that depend on the size of the rain drops and the rain temperature. The rain constants were

obtained from the South African Weather Service for the location where the experiment was conducted. Rain losses can often be compensated by using high powered lasers.

Optical turbulence losses are inevitable in any free-space link and are mostly due to the effects of beam wander and scintillation. From the Rytov's analysis, we can determine a relationship between the variance and the optical turbulence parameter [276]. The attenuation due to turbulence is given by [277]

$$L_{\text{turb}}[dB] = 2\sqrt{23.17 C_n^2 k^{\frac{7}{6}} L^{\frac{11}{6}}}, \tag{6.9}$$

where C_n^2 is the optical turbulence parameter which represents the strength of turbulence and L is the propagation path length. The turbulence strength, was deducted from beam wandering effects as shown in section 3.4. The minimum measured value for the optical turbulence parameter (measured at night) was 3.21×10^{-14} m$^{-2/3}$ where the humidity was at its peak at 50%, the temperature was 289 K and the wind speed was 1.2 m/s. The maximum value for the optical turbulence parameter (measured during the day) was 1.35×10^{-13} m$^{-2/3}$ with 22% humidity, 27.3 ° C and a wind speed of 2.3 m/s. The standard deviation for the optical turbulence parameter is 9.46×10^{-14} m$^{-2/3}$ which is close to 1×10^{-13} m$^{-2/3}$. General guidelines suggest strong turbulence at values of $C_n^2 \approx 10^{-13}$ or more, weak turbulence from $C_n^2 \approx 10^{-17}$ and less, with moderate in between [33]. From the measured turbulence parameters, we calculated the Strehl ratio of the beam at different times of the day. The results are displayed in Fig. 6.3. The best quality was observed during the day when the turbulence is weakest. The results confirm typical diurnal variations during different times of the day.

Geometric losses make up the biggest contribution in all free-space optical communication systems under clear weather conditions. Geometric losses can be calculated by [278]

$$L_{\text{geo}} = -10 \log\left(\frac{D_{\mathbf{Rx}}}{D_{\mathbf{Tx}} + \theta L}\right)^2, \tag{6.10}$$

where D_{Rx} is the diameter of the receiver, D_{Tx} is the diameter of the transmitter and θ, measured in *mrad*, is the divergence of the transmitted beam. Since the geometric losses largely depend on the divergence angle, the transmit beam size was enlarged to minimize diffraction effects as the beam propagates. From the calculated losses, the link budget analysis can then be calculated as

$$P_{\mathbf{Rx}}[W] = \frac{P_{\mathbf{Tx}} G_{\mathbf{Tx}} G_{\mathbf{Rx}} \left(\frac{\lambda}{4\pi z}\right)^2}{L_{\text{sys}}, L_{\text{turb}}, L_{\text{atm}}, L_{\text{rain}}, L_{\text{geo}}}, \tag{6.11}$$

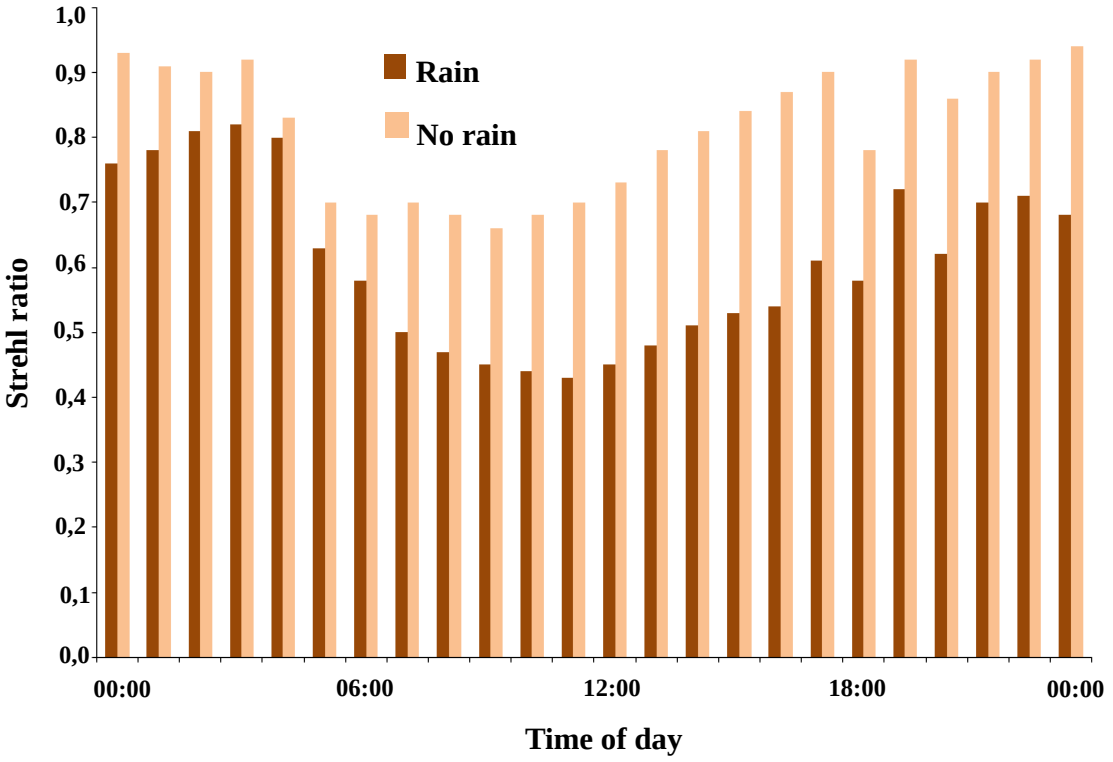


FIGURE 6.3: Strehl ratio at different times of the day. The turbulence strength is strongest at midday, and this is where the image quality is mostly deteriorated. Rainy weather conditions further degrade the image quality when compared to non-rainy weather.

where P_{Tx} is the total power transmitted through the system after the all the losses from each optical component has been eliminated. G_{Tx} and G_{Rx} denote the antenna gain for the transmitter and receiver respectively, while L_{sys} are system-dependent losses which include losses due to link misalignment, telescope losses etc. The total power received at the detector of any free space communication system is therefore given by

$$P_{\mathbf{Rx}} = P_{\mathbf{Tx}} - L_{\mathrm{sys}} - L_{\mathrm{turb}} - L_{\mathrm{atm}} - L_{\mathrm{rain}} - L_{\mathrm{geo}}. \tag{6.12}$$

Table 6.2 lists the parameters used to perform the link budget analysis. The system was set up such that both the Gaussian and Bessel-like beams had equivalent divergences and comparable transmission and receiver losses. Further, as both where expanded to have a Rayleigh length well beyond the link distance ($z_r \approx 10L$), the beams appeared collimated and thus "plane-wave-like". As such, the atmospheric components of the link budget, which are not beam specific, could be calculated assuming simpler plane wave formulations. The losses incurred in the communication link were measured at -24 dB, with geometric losses making up the biggest contribution to this value. The received

Parameters	Value
Transmitter aperture diameter	50.8 mm
Receiver aperture diameter	152.4 mm
Wavelength	632.8 nm
Link range	150 m
Height above ground	9 m
Laser power	17 dBm
Number of lenses	8
Number of mirrors	11
Camera sensitivity	-40 dBm
Receiver focal length	1.5 m
Transmitter power	13.6 dBm

TABLE 6.2: Free-space link parameters.

power was measured to be 12.5 dBm. This ultimately places the strength of the received signal above the sensitivity of the detector, which is -40 dBm.

6.3.3 Crosstalk Results

The conventional method of performing crosstalk measurements is through multiplexing and de-multiplexing. This refers to a process of propagating multiple orthogonal l modes along the same beam axis and spatially separating them at the receiver end by assigning a different carrier frequency to each mode. The crosstalk matrix therefore illustrates the transfer of power between the spatial modes before and after propagation through atmospheric turbulence as depicted in Fig. 6.4. The modes chosen for the demonstration range from $l = -5$ to $l = 5$. The Bessel beam results were compared with helical Gaussian beam results of the same OAM values. Column a) and b) represent the crosstalk measurements for shape-invariant Bessel beams and Gaussian beams respectively, while column c) depicts the normalized power spectrum of mode $l = 2$, for both the Bessel and Gaussian modes. The rows distinguish the different turbulence conditions on which the measurements were taken. The power spectrum was normalized to unity for all the cases.

Before turbulence, negligible inter-modal crosstalk is observed for both the Bessel-like and Gaussian cases as seen on the first row in Fig. 6.4. The normalized power spectrum for the chosen single mode shows most of the energy going into the generated mode and a negligible amount going to other modes as expected. When the beams are propagated through turbulence, we can observe a transfer of power between the modes depending on the turbulence strength. Although the power going into the measured mode has decreased by approximately half under weak turbulence, the weight of the power going into this mode is higher, thereby making it easy to distinguish the mode that was

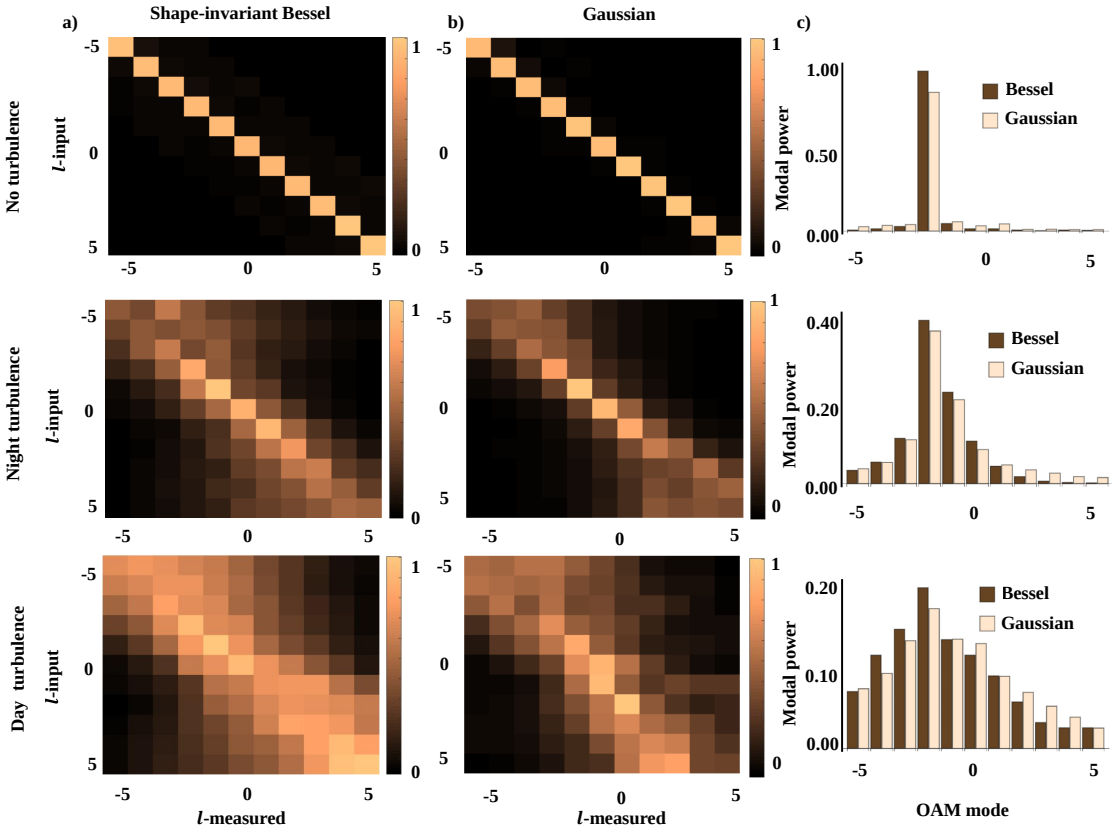


FIGURE 6.4: Experimental results showing inter-modal crosstalk. Shape-invariant BB modes (a) are compared with Gaussian modes (b) under difference turbulence conditions(depicted as rows). (c) illustrates the normalized power spectrum for mode $l = 2$. The turbulence strength during the day and night was estimated to be 3.21×10^{-14} $\mathrm{m}^{-2/3}$ and 1.35×10^{-13} $\mathrm{m}^{-2/3}$ respectively.

sent. This is particularly true for lower order modes compared to their higher order counterparts. This is not the case for high turbulence, where all the modes are seen to lose their orthogonality and it becomes difficult to identify the sent mode. There is no significant difference between the behaviour of shape-invariant Bessel beams and Gaussian beams under the different turbulence conditions.

In addition to using OAM as a information carrier, one might question the plausibility of using radial modes as an independent channel to transmit information. It is important to recall that shape-invariant Bessel beams have longitudinally dependent cone angles, which vary with distance. This means that if we take the power spectrum of beams with different cone angles, we can expect a peak at the cone angle value coinciding with the measuring distance and a somewhat normal distribution around neighbouring cone angles (Fig. 6.5). Since the receiver plane is always at a fixed distance, this limits the carrier to a single channel.

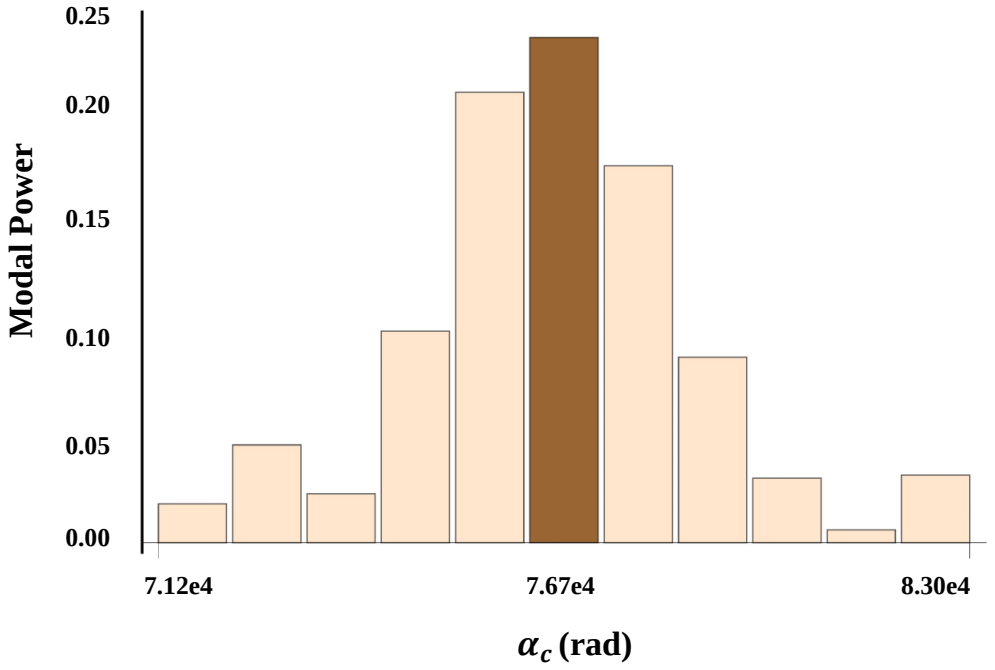


FIGURE 6.5: Power spectrum for radial modes of different cone angles. The mode at the centre of the spectrum represents the mode with a cone angle corresponding to a measurement distance of $z = 210$ cm.

6.4 Discussion and Conclusion

Shape-invariant Bessel beams were generated and propagated for 150 m through real turbulence. The performance of the link was evaluated by performing a link budget analysis, which included characterisation of the turbulence strength at different times of the day. It was seen that the refractive index structure C_n^2 followed typical diurnal variations at different times of the day, where the strongest turbulence was measured during day and the weakest measured at night. The beam was generated using a phase-only element encoded on a Spatial Light Modulator. Parameters of the generating phase element were carefully chosen to allow the beam to retain its Bessel-like structure across the link. Eleven holograms containing OAM beams ranging from $l = -5$ to $+5$ were co-propagated across the link and measured at the receiver plane. The effects of turbulence on the beam were studied by observing any crosstalk between the modes. It was seen from Fig. 6.4 that shape-invariant beams carrying OAM form an orthogonal basis, as there was no transfer of power between the modes when there is no atmospheric turbulence. However, since free-space links are always synonymous with turbulence effects, it was imperative to study the effects this will pose on the channels at different times of the day as turbulence changes. Atmospheric turbulence compromises the orthogonality of

the modes and power is redistributed to neighbouring modes. Power loss and redistribution is higher during the day when fluctuations in index of refraction are higher. In such cases, it becomes arduous to discriminate the modes from each other. This has been the major challenge in all free-space links and adaptive optics often have to be employed to compensate for the effects of atmospheric turbulence. Adaptive solutions are feasible and effective in weak to moderate turbulence where phase-only distortions are dominant, but less effective in strong turbulence where scintillation becomes problematic [279].

From discernment of the beam structure as it returns to the receiver shown in Fig. 6.2 (inset c), it is logical for one to question the significance of the shape-invariant beam over LG beams of the same radial index. The answer to this is two-fold. Firstly, previous literature has demonstrated the advantages of Bessel beams over other OAM modes for free-space optical communications, with respect to channel capacity and power efficiency [233, 235]. Secondly, shape-invariant Bessel beams can provide an added benefit in that they allow much longer reconstruction distances compared to the traditional Bessel beams [268]. While one might expect the Bessel-like beam to outperform the Gaussian beam, the performance between the two beams in this case can be seen to be comparable. This is because both beams are equally adversely affected by phase distortions when using OAM as the information carrier, confirming that the self-healing property does not translate into phase correction, confirming previous laboratory simulations using Bessel beams [237]. However, in the presence of physical obstacles, the Bessel beam would surely outperform the Gaussian as self-healing would be possible for perturbations smaller than the beam size. Further, the additional radial index allows another coding dimension (as we have shown), and so have found additional benefits in free-space communication systems [233, 235]. Thus our study indicates that as OAM carriers the two beams are more or less equivalent, but since Bessel-like beams have additional benefits they would have scope to excel beyond their simpler Gaussian counterparts.

In summary, we have demonstrated the applicability of shape-invariant beams in free-space optical communications by studying their inter-modal crosstalk when propagated through turbulence. It was shown that there is power transfer when the modes are propagated through turbulence, and the power distribution depends on the strength of atmospheric turbulence. These beams therefore can be appended to the list of OAM beams which can be used to transmit information through multiple channels. Future work can be focused on a study of the self-healing behaviour of these beams for long transmission links and engineering low divergence beams for more efficient transmission.

Chapter 7

Conclusion

The propagation of laser beams through free-space remains a topical research area. While the study of spatial modes through turbulence is not new, there are various facets which remain unexplored. It is therefore important to relate the findings in this thesis to current research in an effort to fill knowledge gaps which might exist. In Chapter 1, we provided a brief literature on the use of spatial modes for free-space propagation applications. We outlined the challenges associated with such applications and the key role of spatial modes in this regard. The limitation of each application strongly depends on the range of propagation. Long-haul applications are mostly affected by turbulence induced divergence which ultimately reduces the power delivered to a target. In free-space optical communication systems, turbulence induces effects such as deep fading, power transfer from one mode to another and overall signal attenuation.

In Chapter 2, we provided a theoretical background of the spatial modes studied in subsequent chapters. We also described the methods used for generation and measurement of these modes. While we acknowledge the existence of other techniques, we only discussed techniques most common in laboratories. We made use of Spatial Light Modulators for the creation and characterisation of the modes due to their versatility and can be re-configurable to allow creation of any mode desired. We also described how to calculate interference holograms for generation of the modes. The techniques allow arbitrary control of either phase or both the amplitude and the phase. We lastly described how to characterise the modes using the modal decomposition technique. This technique allows unpacking of a unknown mode into appropriately weighted modes. Measurement of these modal weights is the core of the modal decomposition technique.

Chapter 3 discussed the effects of atmospheric turbulence of laser beams. We discussed the most prevalent wavefront distortions resulting from the variation of the refractive index structure of air. The type of distortions depend on the size of the turbulent eddies

present in the atmosphere with respect to the beam size. Large turbulent eddies result in the deflection of the centroid position at the receiver. On the other hand, eddies smaller than the beam size cause the beam to broaden beyond vacuum diffraction as it propagates. The third effect, known as scintillation, occurs when the eddies are the same size as the beam and results in intensity fluctuations of the beam at the receiver plane. All these effects have a detrimental effect on the free-space propagation of laser beams thereby compromising the optical performance of such systems. We also provided a toolkit on how to simulate and characterise turbulence in the laboratory environment and real world turbulence links respectively. To simulate the turbulence phase screens, we detailed two approaches, one based on Fast Fourier Transform and the other based on Zernike basis functions. The former approach estimates the turbulence phase from the theoretical power spectrum while the latter represents the phase as a weighted sum of Zernike aberrations. The former approach often leads to large errors due to under-sampling of low frequency components such as tip and tilt. Lastly, we described how to characterise atmospheric turbulence in real world terrestrial links. The refractive index parameter can be estimated from beam wandering measurements or by using a wind velocity instrument known as an anenometer. We use the former technique to characterise a free space-link which we use to study shape-invariant Bessel modes in Chapter 6.

Beam wandering effects often lead to tip and tilt errors, which manifests itself as pointing errors in optical systems. The distortions due to beam wander are often so substantial than adaptive optics are required to compensate for their effect. In Chapter 4, we studied the effect of these errors on Hermite-Gaussian and Laguerre-Gaussian modes by comparing the mode crosstalk and mode dependent losses between the two types of modes. We used the modal decomposition technique to measure the modes after being subjected to lateral and randomly distributed displacements. We observed theoretically and experimentally that Hermite-Gaussian modes experience less modal crosstalk and mode dependent losses when laterally displaced along the optical axis of the receiver with aperture size larger than the modes waist sizes. This remains true when the displacements are randomly distributed in all directions. This is attributed to the rectangular symmetry of the Hermite-Gaussian modes which coincide with the lateral displacement direction.

In Chapter 5, we superseded the theory which suggest that Bessel-Gaussian modes are resilient to all forms of obstructions, including phase-changing obstructions such as aberrations and atmospheric turbulence. This was done by studying the self-healing behaviour of digitally generated Bessel-Gaussian modes after being obstructed by aberrations and turbulence of different strengths. It was observed that complete self-healing did occur after encountering Zernike aberrations of minute size in comparison to the

beam size. The spatial characteristics of the aberrations remained noticeable at regions where the beam was expected to have reconstructed. Counter-intuitively, it was noticed that as the turbulence strength was increased, the mode quality improved, giving the illusion of a self-healing effect. Increasing the turbulence strength resulted in diffraction spreading which allows energy to be redistributed outwardly away from the beam centroid where self-healing was observed. However, when all the conical waves were disturbed by turbulence, no self-healing was observed. In fact, the mode was seen to deteriorate with propagation distance. The findings in this study demonstrated that the benefits of Bessel-Gaussian modes in free-space propagation applications does not extend to self-healing, where the Bessel structure gets destroyed by phase distortions.

In Chapter 6, we moved out of the laboratory and into the outside world where we studied modified Bessel-Gaussian beams and their applicability in free-space optics. These modes differ from traditional Bessel-Gaussian beam in that they can maintain their Bessel structure as they propagate without evolving into an annular ring. The modes were propagated through a characterised free-space link to study the effects of atmospheric turbulence on the mode crosstalk. This was done by sending multiplexed modes across the link and measured by modal decomposition upon their return. It was seen that the turbulence-induced crosstalk of the shape-invariant modes was comparable to that of Gaussian modes carrying the same topological charge. This is because both beams are equally adversely affected by turbulence. The Bessel structure of the modes does however provide an advantage over their Gaussian counterparts due to the self-healing property they possess. Therefore, these modes show great potential in optical communication systems, which often suffer from physical obstructions such as flying birds, trees and tall buildings which often temporarily block the light of sight transmission.

It is clear that the unique properties of spatial modes provide great potential in improving the optical performance of free-space optical systems. Our findings offer solutions to some of the challenges encountered in free-space propagation optical systems which range from obstructions internal and external to the optical systems, pointing and steering errors due to turbulence as well as wavefront distortions that reduce the overall performance of the system. While our studies make use of optical communication as a way of example due to the ease of laboratory implementation, the tools developed in this thesis can be transferred to other long-range applications which share similar optical qualities such as laser ranging. In fact, the optical communication systems can be successfully collocated with laser ranging systems with a few minor modifications in the transmit laser [280–282].

Bibliography

[1] Heinz Willebrand and Baksheesh S Ghuman. *Free space optics: enabling optical connectivity in today's networks*. SAMS publishing, 2002.

[2] Vincent WS Chan. Free-space optical communications. *Journal of Lightwave Technology*, 24(12):4750–4762, 2006.

[3] O. Bouchet, H. Sizun, C. Boisrobert, F. de Fornel, and P.N. Favennec. *Free-Space Optics: Propagation and Communication*. ISTE. Wiley, 2010. ISBN 9780470394410. URL https://books.google.co.za/books?id=df-UFVeGcRIC.

[4] Hennes Henniger and Otakar Wilfert. An introduction to free-space optical communications. *Radioengineering*, 19(2):203–212, 2010.

[5] Arun K Majumdar and Jennifer C Ricklin. *Free-space laser communications: principles and advances*, volume 2. Springer Science & Business Media, 2010.

[6] Matthew NO Sadiku, Sarhan M Musa, and Sudarshan R Nelatury. Free space optical communications: an overview. *European Scientific Journal*, 12(9), 2016.

[7] Stephen Hardy. fsona unveils 2-5-gbps free-space optical systems, Sep 2012. URL https://www.lightwaveonline.com/network-design/high-speed-networks/article/16665085/fsona-unveils-25gbps-freespace-optical-systems.

[8] Ludwig Combrinck. Satellite laser ranging. In *Sciences of Geodesy-I*, pages 301–338. Springer, 2010.

[9] PL Bender, DT Wilkinson, CO Alley, DG Currie, JE Faller, JD Mulholland, EC Siverberg, HE Plotkin, WM Kaula, and GJF MacDonald. The lunar laser ranging experiment. In *Proc. Conf. Exp. Tests Gravitation Theories*, pages 178–181, 1971.

[10] James G Williams, XX Newhall, and Jean O Dickey. Relativity parameters determined from lunar laser ranging. *Physical Review D*, 53(12):6730, 1996.

[11] James G Williams, XX Newhall, and Jean O Dickey. Lunar moments, tides, orientation, and coordinate frames. *Planetary and Space Science*, 44(10):1077–1080, 1996.

[12] F Hofmann, J Müller, and L Biskupek. Lunar laser ranging test of the nordtvedt parameter and a possible variation in the gravitational constant. *Astronomy & Astrophysics*, 522:L5, 2010.

[13] Jürgen Müller and Liliane Biskupek. Variations of the gravitational constant from lunar laser ranging data. *Classical and Quantum Gravity*, 24(17):4533, 2007.

[14] Bruno Bertotti, Ignazio Ciufolini, and Peter L Bender. New test of general relativity: Measurement of de sitter geodetic precession rate for lunar perigee. *Physical Review Letters*, 58(11):1062, 1987.

[15] James G Williams, Slava G Turyshev, and Dale H Boggs. Lunar laser ranging tests of the equivalence principle. *Classical and Quantum Gravity*, 29(18):184004, 2012.

[16] J Müller, F Hofmann, and L Biskupek. Testing various facets of the equivalence principle using lunar laser ranging. *Classical and Quantum Gravity*, 29(18):184006, 2012.

[17] Mark A Wieczorek, Bradley L Jolliff, Amir Khan, Matthew E Pritchard, Benjamin P Weiss, James G Williams, Lon L Hood, Kevin Righter, Clive R Neal, Charles K Shearer, et al. The constitution and structure of the lunar interior. *Reviews in Mineralogy and Geochemistry*, 60(1):221–364, 2006.

[18] James G Williams, Slava G Turyshev, Dale H Boggs, and J Todd Ratcliff. Lunar laser ranging science: gravitational physics and lunar interior and geodesy. *Advances in Space Research*, 37(1):67–71, 2006.

[19] JG Williams, DH Boggs, and JT Ratcliff. A larger lunar core? In *Lunar and planetary science conference*, volume 40, page 1452, 2009.

[20] AL Whipple. Dynamics of the earth-moon system. *Advances in Space Research*, 13(11):213–219, 1993.

[21] David E Smith and Donald L Turcotte. *Contributions of space geodesy to geodynamics: earth dynamics*. American Geophysical Union, 1993.

[22] C Huang, W Jin, and H Xu. The terrestrial and lunar reference frame in lunar laser ranging. *Journal of Geodesy*, 73(3):125–129, 1999.

[23] Dmitry Pavlov. Role of lunar laser ranging in realization of terrestrial, lunar, and ephemeris reference frames. *Journal of Geodesy*, 94(1):1–14, 2020.

[24] Jean Kovalevsky, Ivan I Mueller, and Barbara Kolaczek. *Reference frames: in astronomy and geophysics*, volume 154. Springer Science & Business Media, 2012.

[25] Debbie Kedar and Shlomi Arnon. Optical wireless communication through fog in the presence of pointing errors. *Applied Optics*, 42(24):4946–4954, 2003.

[26] Erich Leitgeb, Michael Gebhart, and Ulla Birnbacher. Optical networks, last mile access and applications. In *Free-Space Laser Communications*, pages 273–302. Springer, 2005.

[27] Michael Gebhart, Erich Leitgeb, Sajid Sheikh Muhammad, Benno Flecker, Christoph Chlestil, Maher Al Naboulsi, Herve Sizun, and Frederique de Fornel. Measurement of light attenuation in dense fog conditions for optical wireless links. In *SPIE's Optics & Photonics Conference*, pages 58910k–1, 2005.

[28] Haim Manor and Shlomi Arnon. Performance of an optical wireless communication system as a function of wavelength. *Applied Optics*, 42(21):4285–4294, 2003.

[29] Muhammad Saleem Awan, P Brandl, E Leitgeb, F Nadeem, L Csugai-Horvath, and R Nebuloni. Transmission of high data rate optical signals in fog and snow conditions. In *2009 1st International Conference on Wireless Communication, Vehicular Technology, Information Theory and Aerospace & Electronic Systems Technology*, pages 702–706. IEEE, 2009.

[30] Reza Nasiri Mahalati and Joseph M Kahn. Effect of fog on free-space optical links employing imaging receivers. *Optics Express*, 20(2):1649–1661, 2012.

[31] Martin Grabner and Vaclav Kvicera. Multiple scattering in rain and fog on free-space optical links. *Journal of Lightwave Technology*, 32(3):513–520, 2013.

[32] D Bykhovsky, D Elmakias, and S Arnon. Experimental evaluation of free space links in the presence of turbulence for server backplane. *Journal of Lightwave Technology*, 33(14):2923–2929, 2015.

[33] Larry C Andrews and Ronald L Phillips. *Laser beam propagation through random media*, volume 152. SPIE press Bellingham, WA, 2005.

[34] Peter Shelus. MLRS: A lunar/artificial satellite laser ranging facility at the Mcdonald observatory. *IEEE Transactions on Geoscience and Remote Sensing*, GE-23 (4):385–390, 1985. doi: 10.1109/tgrs.1985.289428.

[35] E. Samain, J. F. Mangin, C. Veillet, J. M. Torre, P. Fridelance, J. E. Chabaudie, D. Féraudy, M. Glentzlin, J. Pham Van, and M. et al. Furia. Millimetric lunar laser ranging at OCA (Observatoire de la Côte d'Azur). *Astronomy and Astrophysics Supplement Series*, 130(2):235–244, 1998. doi: 10.1051/aas:1998227.

[36] WE Carter, E Berg, and S Laurila. The University of Hawaii lunar ranging experiment geodetic-geophysics support programme. *Philosophical Transactions of the Royal Society of London. Series A, Mathematical and Physical Sciences*, 284 (1326):451–456, 1977.

[37] Thomas K Varghese, Winfield M Decker, Henry A Crooks, and Giuseppe Bianco. Matera laser ranging observatory (MLRO): an overview. *NASA. Goddard Space Flight Center*, 1993.

[38] J. B. R. Battat, T. W. Murphy, E. G. Adelberger, B. Gillespie, C. D. Hoyle, R. J. McMillan, E. L. Michelsen, K. Nordtvedt, A. E. Orin, and C. W. et al. Stubbs. The Apache point observatory lunar laser-ranging operation (APOLLO: Two years of millimeter-precision measurements of the earth-moon range. *Publications of the Astronomical Society of the Pacific*, 121(875):29–40, 2009. doi: 10.1086/596748.

[39] David A Arnold. Cross section of the apollo lunar retroreflector arrays. *Washington, DC: ILRS*, 2005.

[40] Mazin Ali Abd Ali and Miami Abdulatteef Mohammed. Effect of atmospheric attenuation on laser communications for visible and infrared wavelengths. *Al-Nahrain Journal of Science*, 16(3):133–140, 2013.

[41] Vishnu Viswanathan, Agnès Fienga, Hervé Manche, Mickael Gastineau, Clément Courde, Jean-Marie Torre, Pierre Exertier, Jacques Laskar, LLR Observers, Apache Point Astrogeo-OCA, et al. Impact of infrared lunar laser ranging on lunar dynamics. In *AAS/Division for Planetary Sciences Meeting Abstracts# 48*, volume 48, 2016.

[42] K Sekine, S Sasaki, and N Kikuchi. 10 Gbit/s four-channel wavelength-and polarisation-division multiplexing transmission over 340 km with 0.5 nm channel spacing. *Electronics Letters*, 31(1):49–50, 1995.

[43] J Renaudier, W Idler, O Bertran-Pardo, F Buchali, K Schuh, H Mardoyan, P Tran, G Charlet, and S Bigo. Long-haul WDM transmission of 448 Gbit/s polarisation-division multiplexed 16-ary quadrature amplitude modulation using coherent detection. *Electronics Letters*, 47(17):973–975, 2011.

[44] H-S Chen, Pa Van Den Boom, and AMJ Koonen. WDM 2 x 2 mode group division multiplexing system and investigation of polarisation division multiplexing. *Electronics Letters*, 47(23):1289–1290, 2011.

[45] Abd El-Naser A Mohamed, Ahmed Nabih Zaki Rashed, Mohamed SF Tabbour, and Amira M Ismail. Performance enhancement of free space optical (FSO) systems using polarized DWDM-OFDM technique under atmospheric disturbances. In *2017 13th International Computer Engineering Conference (ICENCO)*, pages 8–13. IEEE, 2017.

[46] Amit Grover, Anu Sheetal, and Vigneswaran Dhasarathan. Performance analysis of mode division multiplexing based free space optics system incorporating on–off keying and polarization shift keying under dynamic environmental conditions. *Wireless Networks*, 26:3439—-3449, 2020.

[47] Salasiah Hitam, Siti N Suhaimi, Ahmad SM Noor, Siti BA Anas, and Ratna KZ Sahbudin. Performance analysis on 16-channels wavelength division multiplexing in free space optical transmission under tropical regions environment. *Journal of Computer Science*, 8(1):145, 2012.

[48] Sushank Chaudhary, Angela Amphawan, and Kashif Nisar. Realization of free space optics with OFDM under atmospheric turbulence. *Optik*, 125(18):5196–5198, 2014.

[49] S Magidi and A Jabeena. Review on wavelength division multiplexing free space optics. *Journal of Optical Communications*, 1(1):1–14, 2018. doi: https://doi.org/10.1515/joc-2017-0197.

[50] Bindu Sharma, Veena Kumari Thapa, and Abhishek Sharma. Role of wavelength division multiplexing scheme in free space optical communication systems. *International Journal of Computer Applications*, 975:8887, 2019.

[51] Graham Gibson, Johannes Courtial, Miles J Padgett, Mikhail Vasnetsov, Valeriy Pas'ko, Stephen M Barnett, and Sonja Franke-Arnold. Free-space information transfer using light beams carrying orbital angular momentum. *Optics Express*, 12(22):5448–5456, 2004.

[52] Yoshinari Awaji, Naoya Wada, and Yasunori Toda. Demonstration of spatial mode division multiplexing using Laguerre-Gaussian mode beam in telecom-wavelength. In *2010 23rd Annual Meeting of the IEEE Photonics Society*, pages 551–552. IEEE, 2010.

[53] Mario Krenn, Robert Fickler, Matthias Fink, Johannes Handsteiner, Mehul Malik, Thomas Scheidl, Rupert Ursin, and Anton Zeilinger. Communication with

spatially modulated light through turbulent air across Vienna. *New Journal of Physics*, 16(11):113028, 2014.

[54] Mario Krenn, Johannes Handsteiner, Matthias Fink, Robert Fickler, and Anton Zeilinger. Twisted photon entanglement through turbulent air across Vienna. *Proceedings of the National Academy of Sciences*, 112(46):14197–14201, 2015.

[55] Jian Wang, Jeng-Yuan Yang, Irfan M Fazal, Nisar Ahmed, Yan Yan, Hao Huang, Yongxiong Ren, Yang Yue, Samuel Dolinar, Moshe Tur, et al. Terabit free-space data transmission employing orbital angular momentum multiplexing. *Nature Photonics*, 6(7):488, 2012.

[56] Hao Huang, Guodong Xie, Yan Yan, Nisar Ahmed, Yongxiong Ren, Yang Yue, Dvora Rogawski, Moshe J Willner, Baris I Erkmen, Kevin M Birnbaum, Samuel J Dolinar, Martin P J Lavery, Miles J Padgett, Moshe Tur, and Alan E Willner. 100 Tbit/s free-space data link enabled by three-dimensional multiplexing of orbital angular momentum, polarization, and wavelength. *Optics Letters*, 39(2):197–200, 2014. ISSN 1539-4794. doi: 10.1364/OL.39.000197.

[57] Giovanni Milione, Martin PJ Lavery, Hao Huang, Yongxiong Ren, Guodong Xie, Thien An Nguyen, Ebrahim Karimi, Lorenzo Marrucci, Daniel A Nolan, Robert R Alfano, et al. 4× 20 Gbit/s mode division multiplexing over free space using vector modes and a q-plate mode (de) multiplexer. *Optics Letters*, 40(9):1980–1983, 2015.

[58] Yixiao Zhu, Kaiheng Zou, Zhennan Zheng, and Fan Zhang. $\lambda\times$ 144 Tb/s free-space IM-DD transmission employing OAM multiplexing and PDM. *Optics Express*, 24(4):3967, 2016. ISSN 1094-4087. doi: 10.1364/OE.24.003967.

[59] Yifan Zhao, Jun Liu, Jing Du, Shuhui Li, Yan Luo, Andong Wang, Long Zhu, and Jian Wang. Experimental Demonstration of 260-meter Security Free-Space Optical Data Transmission Using 16-QAM Carrying Orbital Angular Momentum (OAM) Beams Multiplexing. In *Optical Fiber Communication Conference*, page Th1H.3, Washington, D.C., 2016. OSA. ISBN 978-1-943580-07-1. doi: 10.1364/OFC.2016.Th1H.3.

[60] Yongxiong Ren, Zhe Wang, Peicheng Liao, Long Li, Guodong Xie, Hao Huang, Zhe Zhao, Yan Yan, Nisar Ahmed, Asher Willner, Martin P. J. Lavery, Nima Ashrafi, Solyman Ashrafi, Robert Bock, Moshe Tur, Ivan B. Djordjevic, Mark A. Neifeld, and Alan E. Willner. Experimental characterization of a 400 Gbit/s orbital angular momentum multiplexed free-space optical link over 120 m. *Optics Letters*, 41(3): 622, 2016. ISSN 0146-9592. doi: 10.1364/OL.41.000622.

[61] Zhen Qu and Ivan B. Djordjevic. 500 Gb/s free-space optical transmission over strong atmospheric turbulence channels. *Optics Letters*, 41(14):3285, 2016. ISSN 0146-9592. doi: 10.1364/OL.41.003285.

[62] Jian Wang, Shuhui Li, Ming Luo, Jun Liu, Long Zhu, Chao Li, Dequan Xie, Qi Yang, Shaohua Yu, Junqiang Sun, Xinliang Zhang, William Shieh, and Alan E. Willner. N-dimentional multiplexing link with 1.036-Pbit/s transmission capacity and 112.6-bit/s/Hz spectral efficiency using OFDM-8QAM signals over 368 WDM pol-muxed 26 OAM modes. In *European Conference on Optical Communication, ECOC*. Institute of Electrical and Electronics Engineers Inc., 2014. ISBN 9782954944401. doi: 10.1109/ECOC.2014.6963934.

[63] Ziqing Wang, Robert Malaney, and Jonathan Green. Detecting orbital angular momentum of light in satellite-to-ground quantum communications. In *2019 IEEE Global Communications Conference (GLOBECOM)*, pages 1–6. IEEE, 2019.

[64] Tatsuo Shiina, Kei Yoshida, Masafumi Ito, and Yasuyuki Okamura. Long-range propagation of annular beam for lidar application. *Optics Communications*, 279 (1):159–167, 2007.

[65] Huiyun Wu, Zhenhai Sun, and Jinbao Chen. Improving performances of the optical systems with cassegrain-telescope receivers by using vortex sources and phase optimizations. *Optics & Laser Technology*, 45:132–136, 2013.

[66] Huiyun Wu, Shen Sheng, Zhisong Huang, Siqing Zhao, Hua Wang, Zhenhai Sun, and Xiegu Xu. Study on power coupling of annular vortex beam propagating through a two-cassegrain-telescope optical system in turbulent atmosphere. *Optics Express*, 21(4):4005–4016, 2013.

[67] Wenbo Sun, Yongxiang Hu, David G MacDonnell, Carl Weimer, and Rosemary R Baize. Technique to separate lidar signal and sunlight. *Optics Express*, 24(12): 12949–12954, 2016.

[68] Carl Weimer, Yong Hu, Jeff T Applegate, Mike Lieber, Wenbo Sun, and David MacDonnell. Lidars utilizing vortex laser beams. In *Ocean Sensing and Monitoring X*, volume 10631, page 106310Q. International Society for Optics and Photonics, 2018.

[69] NASA TECHPORT SUPPORT. Lidar orbital angular momentum sensor, Jun 2018. URL https://data.nasa.gov/dataset/Lidar-Orbital-Angular-Momentum-Sensor/qbdv-6rh2.

[70] Max Born and Emil Wolf. *Principles of optics: electromagnetic theory of propagation, interference and diffraction of light*. Elsevier, 2013.

[71] Herwig Kogelnik and Tingye Li. Laser beams and resonators. *Applied Optics*, 5 (10):1550–1567, 1966.

[72] M Abramowitz and I Stegun. Pocketbook of mathematical functions: Abridged edition of handbook of mathematical functions. *Frankfurt/Main: Harry Deutsch*, 1984.

[73] Anthony E Siegman. Lasers university science books. *Mill Valley, CA*, 37(208): 169, 1986.

[74] Yung-Fu Chen, TM Huang, CF Kao, CL Wang, and SC Wang. Generation of Hermite-Gaussian modes in fiber-coupled laser-diode end-pumped lasers. *IEEE Journal of Quantum Electronics*, 33(6):1025–1031, 1997.

[75] Shu-Chun Chu, Yun-Ting Chen, Ko-Fan Tsai, and Kenju Otsuka. Generation of high-order Hermite-Gaussian modes in end-pumped solid-state lasers for square vortex array laser beam generation. *Optics Express*, 20(7):7128–7141, 2012.

[76] A Forbes, S Ngcobo, T Godin, and K Ait-Ameur. Selective excitation of higher-order modes in diode-pumped solid-state laser resonators. In *Laser Resonators, Microresonators, and Beam Control XV*, volume 8600, page 86000Y. International Society for Optics and Photonics, 2013.

[77] Jun Dong, Yu He, and Shengchuang Bai. High order hermit-gaussian mode passively Q-switched nd:YVO4 microchip laser. In *Advanced Solid State Lasers*, pages ATh2A–12. Optical Society of America, 2015.

[78] Yijie Shen, Yuan Meng, Xing Fu, and Mali Gong. Wavelength-tunable Hermite-Gaussian modes and an orbital-angular-momentum-tunable vortex beam in a dual-off-axis pumped yb: CALGO laser. *Optics Letters*, 43(2):291–294, 2018.

[79] Florian Schepers, Tim Bexter, Tim Hellwig, and Carsten Fallnich. Selective Hermite–Gaussian mode excitation in a laser cavity by external pump beam shaping. *Applied Physics B*, 125(5):75, 2019.

[80] Marco W Beijersbergen, Les Allen, HELO Van der Veen, and JP Woerdman. Astigmatic laser mode converters and transfer of orbital angular momentum. *Optics Communications*, 96(1-3):123–132, 1993.

[81] Andrew Forbes, Angela Dudley, and Melanie McLaren. Creation and detection of optical modes with spatial light modulators. *Advances in Optics and Photonics*, 8 (2):200–227, 2016.

[82] Yu-Xuan Ren, Zhao-Xiang Fang, Lei Gong, Kun Huang, Yue Chen, and Rong-De Lu. Digital generation and control of Hermite–Gaussian modes with an amplitude digital micromirror device. *Journal of Optics*, 17(12):125604, 2015.

[83] Stirling Scholes, Ravin Kara, Jonathan Pinnell, Valeria Rodríguez-Fajardo, and Andrew Forbes. Structured light with digital micromirror devices: a guide to best practice. *Optical Engineering*, 59(4):041202, 2019.

[84] Mitchell A Cox, Ling Cheng, and Andrew Forbes. Digital micro-mirror devices for laser beam shaping. In *Fifth Conference on Sensors, MEMS, and Electro-Optic Systems*, volume 11043, page 110430Y. International Society for Optics and Photonics, 2019.

[85] S Sato, M Ishigure, and H Inaba. Optical trapping and rotational manipulation of microscopic particles and biological cells using higher-order mode nd: YAG laser beams. *Electronics Letters*, 27(20):1831–1832, 1991.

[86] TP Meyrath, F Schreck, JL Hanssen, C-S Chuu, and MG Raizen. A high frequency optical trap for atoms using Hermite-Gaussian beams. *Optics Express*, 13(8):2843–2851, 2005.

[87] Mike Woerdemann, Christina Alpmann, Michael Esseling, and Cornelia Denz. Advanced optical trapping by complex beam shaping. *Laser & Photonics Reviews*, 7(6):839–854, 2013.

[88] Luo Hui, Wang Bing, Yuan Yangsheng, Cui Zhifeng, and Qu Jun. Two types of particle trapping using a partially coherent elegant Hermite-Gaussian beam. *Chinese J Lasers*, 41(5):0502006, 2014.

[89] AP Porfirev and RV Skidanov. Optical trapping and manipulation of light-absorbing particles by means of a Hermite–Gaussian laser beam. *Journal of Optical Technology*, 82(9):587–591, 2015.

[90] Angela Amphawan, Sushank Chaudhary, and Tse-Kian Neo. Hermite-Gaussian mode division multiplexing for free-space optical interconnects. *Advanced Science Letters*, 21(10):3050–3053, 2015.

[91] Solyman Ashrafi, Roger Linquist, Moshe Tur, and Alan E Willner. Link analysis of using Hermite-Gaussian modes for transmitting multiple channels in a free-space optical communication system. *The Optical Society*, 2(4), 2015.

[92] Angela Amphawan, Sushank Chaudhary, Hafiza Samad, and Jihadah Ahmad. Mode division multiplexing of LG and HG modes in RO-FSO. *Proceeding of the Electrical Engineering Computer Science and Informatics*, 2(1):133–137, 2015.

[93] Bienvenu Ndagano, Nokwazi Mphuthi, Giovanni Milione, and Andrew Forbes. Comparing mode-crosstalk and mode-dependent loss of laterally displaced orbital angular momentum and Hermite–Gaussian modes for free-space optical communication. *Optics Letters*, 42(20):4175–4178, 2017.

[94] Kai Pang, Haoqian Song, Zhe Zhao, Runzhou Zhang, Hao Song, Guodong Xie, Long Li, Cong Liu, Jing Du, Andreas F Molisch, et al. 400-Gbit/s qpsk free-space optical communication link based on four-fold multiplexing of Hermite–Gaussian or Laguerre–Gaussian modes by varying both modal indices. *Optics Letters*, 43 (16):3889–3892, 2018.

[95] Sushank Chaudhary and Angela Amphawan. High-speed MDM-RO-FSO system by incorporating spiral-phased Hermite Gaussian modes. *Photonic Network Communications*, 35(3):374–380, 2018.

[96] Sara Alshwani, Ahmed M Fakhrudeen, Mohammed Nasih Ismael, Aras Al-Dawoodi, and Alaan Ghazi. Hermite-Gaussian mode in spatial division multiplexing over FSO system under different weather condition based on linear gaussian filter. *International Journal of Mechanical Engineering and Technology*, 10(1): 1095–1105, 2019.

[97] AMIT GROVER, ANU SHEETAL, et al. A cost-effective high-capacity OFDM based FSO transmission link incorporating hybrid SS-WDM-MDM of Hermite Gaussian modes. *Optoelectronics and Advanced Materials-Rapid Communications*, 14(March-April 2020):136–145, 2020.

[98] Les Allen, Marco W Beijersbergen, RJC Spreeuw, and JP Woerdman. Orbital angular momentum of light and the transformation of Laguerre-Gaussian laser modes. *Physical Review A*, 45(11):8185, 1992.

[99] Jeffrey Shapiro, Saikat Guha, and Baris Erkmen. Ultimate channel capacity of free-space optical communications. *Journal of Optical Networking*, 4(8):501–516, 2005.

[100] Zdenek Bouchal and Radek Celechovskỳ. Mixed vortex states of light as information carriers. *New Journal of Physics*, 6(1):131, 2004.

[101] Alan E Willner, Hao Huang, Yan Yan, Yongxiong Ren, Nisar Ahmed, Goudong Xie, Changjing Bao, L Li, Y Cao, Z Zhao, et al. Optical communications using orbital angular momentum beams. *Advances in Optics and Photonics*, 7(1):66–106, 2015.

[102] Ivan B Djordjevic. Deep-space and near-earth optical communications by coded orbital angular momentum (OAM) modulation. *Optics Express*, 19(15):14277–14289, 2011.

[103] Alison M Yao and Miles J Padgett. Orbital angular momentum: origins, behavior and applications. *Advances in Optics and Photonics*, 3(2):161–204, 2011.

[104] Tiehui Su, Ryan P Scott, Stevan S Djordjevic, Nicolas K Fontaine, David J Geisler, Xinran Cai, and SJB Yoo. Demonstration of free space coherent optical communication using integrated silicon photonic orbital angular momentum devices. *Optics Express*, 20(9):9396–9402, 2012.

[105] GA Turnbull, DA Robertson, GM Smith, L Allen, and MJ Padgett. The generation of free-space Laguerre-Gaussian modes at millimetre-wave frequencies by use of a spiral phaseplate. *Optics Communications*, 127(4-6):183–188, 1996.

[106] Sharon A Kennedy, Matthew J Szabo, Hilary Teslow, James Z Porterfield, and ERI Abraham. Creation of Laguerre-Gaussian laser modes using diffractive optics. *Physical Review A*, 66(4):043801, 2002.

[107] G Ruffato, M Massari, and F Romanato. Generation of high-order Laguerre–Gaussian modes by means of spiral phase plates. *Optics Letters*, 39(17):5094–5097, 2014.

[108] J Arlt, K Dholakia, L Allen, and MJ Padgett. The production of multiringed Laguerre–Gaussian modes by computer-generated holograms. *Journal of Modern Optics*, 45(6):1231–1237, 1998.

[109] Yoshiyuki Ohtake, Taro Ando, Norihiro Fukuchi, Naoya Matsumoto, Haruyasu Ito, and Tsutomu Hara. Universal generation of higher-order multiringed Laguerre-Gaussian beams by using a spatial light modulator. *Optics Letters*, 32(11):1411–1413, 2007.

[110] Naoya Matsumoto, Taro Ando, Takashi Inoue, Yoshiyuki Ohtake, Norihiro Fukuchi, and Tsutomu Hara. Generation of high-quality higher-order Laguerre-Gaussian beams using liquid-crystal-on-silicon spatial light modulators. *Journal of the Optical Society of America A*, 25(7):1642–1651, 2008.

[111] Taro Ando, Yoshiyuki Ohtake, Naoya Matsumoto, Takashi Inoue, and Norihiro Fukuchi. Mode purities of Laguerre–Gaussian beams generated via complex-amplitude modulation using phase-only spatial light modulators. *Optics Letters*, 34(1):34–36, 2009.

[112] Yu-Xuan Ren, Ming Li, Kun Huang, Jian-Guang Wu, Hong-Fang Gao, Zi-Qiang Wang, and Yin-Mei Li. Experimental generation of Laguerre-Gaussian beam using digital micromirror device. *Applied Optics*, 49(10):1838–1844, 2010.

[113] Vitaly Lerner, David Shwa, Yehonathan Drori, and Nadav Katz. Shaping Laguerre–Gaussian laser modes with binary gratings using a digital micromirror device. *Optics Letters*, 37(23):4826–4828, 2012.

[114] Mohammad Mirhosseini, Omar S Magana-Loaiza, Changchen Chen, Brandon Rodenburg, Mehul Malik, and Robert W Boyd. Rapid generation of light beams carrying orbital angular momentum. *Optics Express*, 21(25):30196–30203, 2013.

[115] J Durnin. Exact solutions for nondiffracting beams. i. the scalar theory. *Journal of the Optical Society of America A*, 4(4):651–654, 1987.

[116] J Durnin, JJ Miceli Jr, and JH Eberly. Diffraction-free beams. *Physical Review Letters*, 58(15):1499, 1987.

[117] F Gori, G Guattari, and C Padovani. Bessel-Gauss beams. *Optics Communications*, 64(6):491–495, 1987.

[118] Zdeněk Bouchal. Nondiffracting optical beams: physical properties, experiments, and applications. *Czechoslovak Journal of Physics*, 53(7):537–578, 2003.

[119] David McGloin and Kishan Dholakia. Bessel beams: diffraction in a new light. *Contemporary Physics*, 46(1):15–28, 2005.

[120] Zdenek Bouchal, J Wagner, and M Chlup. Self-reconstruction of a distorted nondiffracting beam. *Optics Communications*, 151(4-6):207–211, 1998.

[121] CA McQueen, J Arlt, and K Dholakia. An experiment to study a "nondiffracting" light beam. *American Journal of Physics*, 67(10):912–915, 1999.

[122] David L Shealy and Fred M Dickey. Laser beam shaping. *Optical Engineering*, 42 (11):3077–3079, 2003.

[123] David L Andrews. *Structured light and its applications: An introduction to phase-structured beams and nanoscale optical forces*. Academic press, 2011.

[124] Andrew Forbes. *Laser beam propagation: generation and propagation of customized light*. CRC Press, 2014.

[125] Fred M Dickey. *Laser beam shaping: theory and techniques*. CRC press, 2018.

[126] Parameswaran Hariharan. *Basics of holography*. Cambridge University Press, 2002.

[127] Uzi Efron. *Spatial light modulator technology: materials, devices, and applications*, volume 47. CRC press, 1994.

[128] Christian Kohler, Xavier Schwab, and Wolfgang Osten. Optimally tuned spatial light modulators for digital holography. *Applied Optics*, 45(5):960–967, 2006.

[129] Tobias Haist and Wolfgang Osten. Holography using pixelated spatial light modulators—part 1: theory and basic considerations. *Journal of Micro/Nanolithography, MEMS, and MOEMS*, 14(4):041310, 2015.

[130] BR Boruah. Dynamic manipulation of a laser beam using a liquid crystal spatial light modulator. *American Journal of Physics*, 77(4):331–336, 2009.

[131] Jerneja Pavlin, Nataša Vaupotič, and Mojca Čepič. Liquid crystals: a new topic in physics for undergraduates. *European Journal of Physics*, 34(3):745, 2013.

[132] Derek Huang, Henry Timmers, Adam Roberts, Niranjan Shivaram, and Arvinder S Sandhu. A low-cost spatial light modulator for use in undergraduate and graduate optics labs. *American Journal of Physics*, 80(3):211–215, 2012.

[133] Luiz Gonçalves Neto, Danny Roberge, and Yunlong Sheng. Full-range, continuous, complex modulation by the use of two coupled-mode liquid-crystal televisions. *Applied Optics*, 35(23):4567–4576, 1996.

[134] Long Zhu and Jian Wang. Arbitrary manipulation of spatial amplitude and phase using phase-only spatial light modulators. *Scientific Reports*, 4:7441, 2014.

[135] Joseph P Kirk and Alan L Jones. Phase-only complex-valued spatial filter. *Journal of the Optical Society of America*, 61(8):1023–1028, 1971.

[136] CK Hsueh and AA Sawchuk. Computer-generated double-phase holograms. *Applied Optics*, 17(24):3874–3883, 1978.

[137] Robert W Cohn and Minhua Liang. Approximating fully complex spatial modulation with pseudorandom phase-only modulation. *Applied Optics*, 33(20):4406–4415, 1994.

[138] Robert W Cohn. Pseudorandom encoding of complex-valued functions onto amplitude-coupled phase modulators. *Journal of the Optical Society of America A*, 15(4):868–883, 1998.

[139] Jeffrey A Davis, Don M Cottrell, Juan Campos, María J Yzuel, and Ignacio Moreno. Encoding amplitude information onto phase-only filters. *Applied Optics*, 38(23):5004–5013, 1999.

[140] Victor Arrizón. Complex modulation with a twisted-nematic liquid-crystal spatial light modulator: double-pixel approach. *Optics Letters*, 28(15):1359–1361, 2003.

[141] Victor Arrizón. Optimum on-axis computer-generated hologram encoded into low-resolution phase-modul ation devices. *Optics Letters*, 28(24):2521–2523, 2003.

[142] Victor Arrizón, Guadalupe Méndez, and David Sánchez-de La-Llave. Accurate encoding of arbitrary complex fields with amplitude-only liquid crystal spatial light modulators. *Optics Express*, 13(20):7913–7927, 2005.

[143] Jeffrey A Davis, Keevin Olea Valadéz, and Don M Cottrell. Encoding amplitude and phase information onto a binary phase-only spatial light modulator. *Applied Optics*, 42(11):2003–2008, 2003.

[144] Zoltán Göröcs, Gábor Erdei, Tamás Sarkadi, Ferenc Ujhelyi, Judit Reményi, Pál Koppa, and Emoke Lorincz. Hybrid multinary modulation using a phase modulating spatial light modulator and a low-pass spatial filter. *Optics Letters*, 32(16): 2336–2338, 2007.

[145] Victor Arrizón, Ulises Ruiz, Rosibel Carrada, and Luis A González. Pixelated phase computer holograms for the accurate encoding of scalar complex fields. *Journal of the Optical Society of America A*, 24(11):3500–3507, 2007.

[146] Damon WK Wong and George Chen. Redistribution of the zero order by the use of a phase checkerboard pattern in computer generated holograms. *Applied Optics*, 47(4):602–610, 2008.

[147] EG Van Putten, Ivo Micha Vellekoop, and AP Mosk. Spatial amplitude and phase modulation using commercial twisted nematic lcds. *Applied Optics*, 47(12):2076–2081, 2008.

[148] V Arrizón, U Ruiz, G Mendez, and A Apolinar-Iribe. Zero order synthetic hologram with a sinusoidal phase carrier for generation of multiple beams. *Optics Express*, 17(4):2663–2669, 2009.

[149] Jorge Albero, Pascuala García-Martínez, José Luis Martínez, and Ignacio Moreno. Second order diffractive optical elements in a spatial light modulator with large phase dynamic range. *Optics and Lasers in Engineering*, 51(2):111–115, 2013.

[150] Andrey S Ostrovsky, Carolina Rickenstorff-Parrao, and Víctor Arrizón. Generation of the "perfect" optical vortex using a liquid-crystal spatial light modulator. *Optics Letters*, 38(4):534–536, 2013.

[151] Tamás Sarkadi, Ádám Kettinger, and Pál Koppa. Spatial filters for complex wavefront modulation. *Applied Optics*, 52(22):5449–5454, 2013.

[152] Eliot Bolduc, Nicolas Bent, Enrico Santamato, Ebrahim Karimi, and Robert W Boyd. Exact solution to simultaneous intensity and phase encryption with a single phase-only hologram. *Optics Letters*, 38(18):3546–3549, 2013.

[153] Omel Mendoza-Yero, Gladys Mínguez-Vega, and Jesús Lancis. Encoding complex fields by using a phase-only optical element. *Optics Letters*, 39(7):1740–1743, 2014.

[154] Thomas Kaiser, Daniel Flamm, Siegmund Schröter, and Michael Duparré. Complete modal decomposition for optical fibers using CGH-based correlation filters. *Optics Express*, 17(11):9347–9356, 2009.

[155] Daniel Flamm, Darryl Naidoo, Christian Schulze, Andrew Forbes, and Michael Duparré. Mode analysis with a spatial light modulator as a correlation filter. *Optics Letters*, 37(13):2478–2480, 2012.

[156] Joseph W Goodman. *Introduction to Fourier optics*. Roberts and Company Publishers, 2005.

[157] François Roddier. The effects of atmospheric turbulence in optical astronomy. In *Progress in Optics*, volume 19, pages 281–376. Elsevier, 1981.

[158] R.L. Fante. Electromagnetic beam propagation in turbulent media. *Proceedings of the IEEE*, 63(12):1669–1692, 1975. ISSN 0018-9219. doi: 10.1109/PROC.1975.10035.

[159] James H. Churnside and Richard J. Lataitis. Angle-of-arrival fluctuations of a reflected beam in atmospheric turbulence. *Journal of the Optical Society of America A*, 4(7):1264, 1987. ISSN 1084-7529. doi: 10.1364/josaa.4.001264.

[160] David L Fried. Aperture averaging of scintillation. *Journal of the Optical Society of America*, 57(2):169–175, 1967.

[161] Mehul Malik, Malcolm O'Sullivan, Brandon Rodenburg, Mohammad Mirhosseini, Jonathan Leach, Martin PJ Lavery, Miles J Padgett, and Robert W Boyd. Influence of atmospheric turbulence on optical communications using orbital angular momentum for encoding. *Optics Express*, 20(12):13195–13200, 2012.

[162] S M Zhao, J Leach, L Y Gong, J Ding, and B Y Zheng. Aberration corrections for free-space optical communications in atmosphere turbulence using orbital angular momentum states. *Optics Express*, 20(1):452, 2012. ISSN 1094-4087. doi: 10.1364/OE.20.000452.

[163] Mingjian Cheng, Lixin Guo, Jiangting Li, and Yixin Zhang. Channel capacity of the OAM-based free-space optical communication links with Bessel–Gauss beams in turbulent ocean. *IEEE Photonics Journal*, 8(1):1–11, 2016.

[164] Benjamin L McGlamery. Restoration of turbulence-degraded images. *Journal of the Optical Society of America*, 57(3):293–297, 1967.

[165] R G Lane, A Glindemann, and J C Dainty. Simulations of a Kolmogorov phase screen. *Waves in Random Media*, 2(April):209, 1992. ISSN 0959-7174. doi: 10.1088/0959-7174/2/3/003.

[166] JY Wang and D Es Silva. Wave-front interpretation with zernike polynomials. *Applied optics*, 19(9):1510–1518, 1980.

[167] Robert J Noll. Zernike polynomials and atmospheric turbulence. *Journal of the Optical Society of America*, 66(3):207–211, 1976.

[168] Carmelo Rosales-Guzmán and Andrew Forbes. *How to shape light with spatial light modulators*. SPIE Press, 2017.

[169] Sherman Karp, Robert M Gagliardi, Steven E Moran, and Lawrence B Stotts. *Optical channels: fibers, clouds, water, and the atmosphere*. Springer Science & Business Media, 2013.

[170] Dirk Giggenbach, Hennes Henniger, and Florian X David. Long-term near-ground optical scintillation measurements. In *Atmospheric Propagation*, volume 4976, pages 132–140. International Society for Optics and Photonics, 2003.

[171] Yasushi Mitsuta. Sonic anemometer-thermometer for atmospheric turbulence measurements. *Springer*, 1:341–347, 1974.

[172] JC Kaimal. Sonic anemometer measurement of atmospheric turbulence. In *Proceedings of the Dynamic Flow Conference 1978 on Dynamic Measurements in Unsteady Flows*, pages 551–565. Springer, 1978.

[173] Dennis Killinger. Free space optics for laser communication through the air. *Optics and Photonics News*, 13(10):36–42, 2002.

[174] Connectivity lab, Oct 2016. URL https://info.internet.org/en/story/connectivity-lab/.

[175] Hao Huang, Guodong Xie, Yan Yan, Nisar Ahmed, Yongxiong Ren, Yang Yue, Dvora Rogawski, Moshe J Willner, Baris I Erkmen, Kevin M Birnbaum, J Dolinar, Samuel, Martin P J Lavery, Miles J Padgett, Moshe Tur, and Alan E Willner. 100 Tbit/s free-space data link enabled by three-dimensional multiplexing of orbital angular momentum, polarization, and wavelength. *Optics Letters*, 39(2):197–200, 2014.

[176] Yongxiong Ren, Zhe Wang, Peicheng Liao, Long Li, Guodong Xie, Hao Huang, Zhe Zhao, Yan Yan, Nisar Ahmed, Asher Willner, et al. Experimental characterization of a 400 Gbit/s orbital angular momentum multiplexed free-space optical link over 120 m. *Optics Letters*, 41(3):622–625, 2016.

[177] Yifan Zhao, Jun Liu, Jing Du, Shuhui Li, Yan Luo, Andong Wang, Long Zhu, and Jian Wang. Experimental demonstration of 260-meter security free-space optical data transmission using 16-qam carrying orbital angular momentum (OAM) beams multiplexing. In *Optical Fiber Communication Conference*, pages Th1H–3. Optical Society of America, 2016.

[178] Guodong Xie, Long Li, Yongxiong Ren, Hao Huang, Yan Yan, Nisar Ahmed, Zhe Zhao, Martin PJ Lavery, Nima Ashrafi, Solyman Ashrafi, et al. Performance metrics and design considerations for a free-space optical orbital-angular-momentum–multiplexed communication link. *Optica*, 2(4):357–365, 2015.

[179] Giovanni Milione, Thien An Nguyen, Jonathan Leach, Daniel A Nolan, and Robert R Alfano. Using the nonseparability of vector beams to encode information for optical communication. *Optics Letters*, 40(21):4887–4890, 2015.

[180] Giovanni Milione, Martin PJ Lavery, Hao Huang, Yongxiong Ren, Guodong Xie, Thien An Nguyen, Ebrahim Karimi, Lorenzo Marrucci, Daniel A Nolan, Robert R Alfano, et al. 4× 20 Gbit/s mode division multiplexing over free space using vector modes and a q-plate mode (de) multiplexer. *Optics Letters*, 40(9):1980–1983, 2015.

[181] Giovanni Milione, Ezra Ip, Ming-Jun Li, Jefferey Stone, Gaozhu Peng, and Ting Wang. Mode crosstalk matrix measurement of a 1 km elliptical core few-mode optical fiber. *Optics Letters*, 41(12):2755–2758, 2016.

[182] Ezra Ip, Giovanni Milione, Ming-Jun Li, Neda Cvijetic, Konstantinos Kanonakis, Jeffery Stone, Gaozhu Peng, Xesús Prieto, Carlos Montero, Vicente Moreno, et al. SDM transmission of real-time 10Gbe traffic using commercial SFP+ transceivers over 0.5 km elliptical-core few-mode fiber. *Optics Express*, 23(13):17120–17126, 2015.

[183] Abderrahmen Trichili, Carmelo Rosales-Guzmán, Angela Dudley, Bienvenu Ndagano, Amine Ben Salem, Mourad Zghal, and Andrew Forbes. Optical communication beyond orbital angular momentum. *Scientific Reports*, 6:27674, 2016.

[184] SJ Van Enk and G Nienhuis. Eigenfunction description of laser beams and orbital angular momentum of light. *Optics Communications*, 94(1-3):147–158, 1992.

[185] Jun John Sakurai, Jim Napolitano, et al. *Modern quantum mechanics*, volume 185. Pearson Harlow, 2014.

[186] Alan E Willner, Guodong Xie, Long Li, Yongxiong Ren, Yan Yan, Nisar Ahmed, Zhe Zhao, Zhe Wang, Cong Liu, Asher J Willner, et al. Design challenges and guidelines for free-space optical communication links using orbital-angular-momentum multiplexing of multiple beams. *Journal of Optics*, 18(7):074014, 2016.

[187] Sara Restuccia, Daniel Giovannini, Graham Gibson, and Miles Padgett. Comparing the information capacity of Laguerre–Gaussian and Hermite–g=Gaussian modal sets in a finite-aperture system. *Optics Express*, 24(24):27127–27136, 2016.

[188] Carl Paterson and Robin Smith. Higher-order Bessel waves produced by axicon-type computer-generated holograms. *Optics Communications*, 124(1):121–130, 1996.

[189] S Hacyan and R Jáuregui. A relativistic study of Bessel beams. *Journal of Physics B: Atomic, Molecular and Optical Physics*, 39(7):1669, 2006.

[190] Angela Dudley, Martin Lavery, Miles Padgett, and Andrew Forbes. Unraveling Bessel beams. *Optics and Photonics News*, 24(6):22–29, 2013.

[191] Angela Dudley, Thandeka Mhlanga, Martin Lavery, Andre McDonald, Filippus S Roux, Miles Padgett, and Andrew Forbes. Efficient sorting of Bessel beams. *Optics Express*, 21(1):165–171, 2013.

[192] Angela Dudley, Yanming Li, Thandeka Mhlanga, Michael Escuti, and Andrew Forbes. Generating and measuring nondiffracting vector Bessel beams. *Optics Letters*, 38(17):3429–3432, 2013.

[193] Jochen Arlt, Veneranda Garcés-Chávez, Wilson Sibbett, and Kishan Dholakia. Optical micromanipulation using a Bessel light beam. *Optics Communications*, 197(4-6):239–245, 2001.

[194] A. Ashkin, J. M. Dziedzic, J. E. Bjorkholm, and Steven Chu. Observation of a single-beam gradient force optical trap for dielectric particles. *Optics Letters*, 11 (5):288–290, May 1986.

[195] Veneranda Garcés-Chávez, Karen Volke-Sepulveda, Sabino Chávez-Cerda, Wilson Sibbett, and Kishan Dholakia. Transfer of orbital angular momentum to an optically trapped low-index particle. *Physical Review A*, 66(6):063402, 2002.

[196] V. Garcés-Chávez, D. Mcgloin, H. Melville, W. Sibbett, and K. Dholakia. Simultaneous micromanipulation in multiple planes using a self-reconstructing light beam. *Nature*, 419(6903):145–147, 2002. doi: 10.1038/nature01007.

[197] V Kollarova, T Medrik, R Celechovsky, Z Bouchal, O Wilfert, and Z Kolka. Application of nondiffracting beams to wireless optical communications. In *SPIE Proceedings*, volume 6736, page 67361C, 2007.

[198] Shuhui Li and Jian Wang. Adaptive free-space optical communications through turbulence using self-healing Bessel beams. *Scientific Reports*, 7:43233, 2017.

[199] Nisar Ahmed, Zhe Zhao, Long Li, Hao Huang, Martin PJ Lavery, Peicheng Liao, Yan Yan, Zhe Wang, Guodong Xie, Yongxiong Ren, et al. Mode-division-multiplexing of multiple Bessel-gaussian beams carrying orbital-angular-momentum for obstruction-tolerant free-space optical and millimetre-wave communication links. *Scientific Reports*, 6:22082, 2016.

[200] Shi Chen, Shuhui Li, Yifan Zhao, Jun Liu, Long Zhu, Andong Wang, Jing Du, Li Shen, and Jian Wang. Demonstration of 20-Gbit/s high-speed Bessel beam encoding/decoding link with adaptive turbulence compensation. *Optics Letters*, 41(20):4680–4683, 2016.

[201] Abderrahmen Trichili, Thandeka Mhlanga, Yaseera Ismail, Filippus S Roux, Melanie McLaren, Mourad Zghal, and Andrew Forbes. Detection of Bessel beams with digital axicons. *Optics Express*, 22(14):17553–17560, 2014.

[202] Nisar Ahmed, Martin P. J. Lavery, Hao Huang, Guodong Xie, Yongxiong Ren, Yan Yan, and Alan E. Willner. Experimental demonstration of obstruction-tolerant free-space transmission of two 50-Gbaud QPSK data channels using Bessel beams carrying orbital angular momentum. *2014 The European Conference on Optical Communication (ECOC)*, 2014. doi: 10.1109/ecoc.2014.6964157.

[203] Jing Du and Jian Wang. High-dimensional structured light coding/decoding for free-space optical communications free of obstructions. *Optics Letters*, 40(21): 4827, 2015. doi: 10.1364/ol.40.004827.

[204] Shuhui Li and Jian Wang. Adaptive free-space optical communications through turbulence using self-healing Bessel beams. *Scientific Reports*, 7(1), 2017. doi: 10.1038/srep43233.

[205] Timothy Doster and Abbie T. Watnik. Laguerre–Gauss and Bessel–Gauss beams propagation through turbulence: analysis of channel efficiency. *Applied Optics*, 55 (36):10239, 2016. doi: 10.1364/ao.55.010239.

[206] Tyan-Lin Wang, John A Gariano, and Ivan B Djordjevic. Employing Bessel-gaussian beams to improve physical-layer security in free-space optical communications. *IEEE Photonics Journal*, 10(5):1–13, 2018.

[207] R Jáuregui and S Hacyan. Quantum-mechanical properties of Bessel beams. *Physical Review A*, 71(3):033411, 2005.

[208] Melanie McLaren, Thandeka Mhlanga, Miles J Padgett, Filippus S Roux, and Andrew Forbes. Self-healing of quantum entanglement after an obstruction. *Nature Communications*, 5:ncomms4248, 2014.

[209] Héctor Cruz-Ramírez, Roberto Ramírez-Alarcón, Francisco J Morelos, Pedro A Quinto-Su, Julio C Gutiérrez-Vega, and Alfred B U'Ren. Observation of non-diffracting behavior at the single-photon level. *Optics Express*, 20(28):29761–29768, 2012.

[210] M. McLaren, M. Agnew, J. Leach, F.S. Roux, M.J. Padgett, R.W. Boyd, and A. Forbes. Entangled Bessel-Gaussian beams. *Optics Express*, 20(21):23589–23597, 2012.

[211] V. Pyragaite, A. Piskarskas, K. Regelskis, V. Smilgevicius, A. Stabinis, and S. Mikalauskas. Parametric down-conversion of higher-order Bessel optical beams in quadratic nonlinear medium. *Optics Commununications*, 240(1):191–200, 2004.

[212] Melanie McLaren, Jacquiline Romero, Miles J Padgett, Filippus S. Roux, and Andrew Forbes. Two-photon optics of Bessel-Gaussian modes. *Physical Review A*, 88:033818, 2013.

[213] Mathieu Fortin, Michel Piché, and Ermanno F. Borra. Optical tests with Bessel beam interferometry. *Optics Express*, 12(24):5887–5895, Nov 2004. doi: 10.1364/OPEX.12.005887.

[214] Florian O. Fahrbach, Philipp Simon, and Alexander Rohrbach. Microscopy with self-reconstructing beams. *Nature Photonics*, 4(11):780–785, 2010. doi: 10.1038/nphoton.2010.204.

[215] Florian O. Fahrbach, Vasily Gurchenkov, Kevin Alessandri, Pierre Nassoy, and Alexander Rohrbach. Light-sheet microscopy in thick media using scanned Bessel beams and two-photon fluorescence excitation. *Optics Express*, 21(11):13824, 2013. doi: 10.1364/oe.21.013824.

[216] C Ryu, KC Henderson, and MG Boshier. Creation of matter wave Bessel beams and observation of quantized circulation in a Bose–Einstein condensate. *New Journal of Physics*, 16(1):013046, 2014.

[217] V. Grillo, E. Karimi, G. C. Gazzadi, S. Frabboni, M. R. Dennis, and R. W. Boyd. Generation of nondiffracting electron Bessel beams. *Physical Review X*, 4 (1):011013, 2014.

[218] Giovanni Milione, Angela Dudley, Thien An Nguyen, Ougni Chakraborty, Ebrahim Karimi, Andrew Forbes, and Robert R Alfano. Measuring the self-healing of the spatially inhomogeneous states of polarization of vector Bessel beams. *Journal of Optics*, 17(3):035617, 2015.

[219] Peng Li, Yi Zhang, Sheng Liu, Huachao Cheng, Lei Han, Dongjing Wu, and Jianlin Zhao. Generation and self-healing of vector Bessel-gauss beams with variant state of polarizations upon propagation. *Optics Express*, 25(5):5821–5831, 2017.

[220] Florian O Fahrbach, Philipp Simon, and Alexander Rohrbach. Microscopy with self-reconstructing beams. *Nature Photonics*, 4(11):780, 2010.

[221] T Ersoy, B Yalizay, and S Akturk. Self-reconstruction of diffraction-free and accelerating laser beams in scattering media. *Journal of Quantitative Spectroscopy and Radiative Transfer*, 113(18):2470–2475, 2012.

[222] Rafael Piestun, Yoav Y Schechner, and Joseph Shamir. Propagation-invariant wave fields with finite energy. *Journal of the Optical Society of America A*, 17(2): 294–303, 2000.

[223] Job Mendoza-Hernández, Maximino Luis Arroyo-Carrasco, Marcelo David Iturbe-Castillo, and Sabino Chávez-Cerda. Laguerre–Gauss beams versus Bessel beams showdown: peer comparison. *Optics Letters*, 40(16):3739–3742, 2015.

[224] Andrea Aiello and Girish S Agarwal. Self-healing of Gaussian and Bessel beams: a critical comparison. *ArXiv:1501.05722*, 2015.

[225] Andrea Aiello, Girish S Agarwal, Martin Paúr, Bohumil Stoklasa, Zdeněk Hradil, Jaroslav Řeháček, Pablo de la Hoz, Gerd Leuchs, and Luis L Sánchez-Soto. Unraveling beam self-healing. *Optics Express*, 25(16):19147–19157, 2017.

[226] Andrea Aiello and Girish S Agarwal. Wave-optics description of self-healing mechanism in Bessel beams. *Optics Letters*, 39(24):6819–6822, 2014.

[227] Yalin Zhang, Donglin Ma, Xiuhua Yuan, and Zeyu Zhou. Numerical investigation of flat-topped vortex hollow beams and Bessel beams propagating in a turbulent atmosphere. *Applied Optics*, 55(32):9211–9216, 2016.

[228] Marcelino Anguiano-Morales, M Maribel Méndez-Otero, M David Iturbe-Castillo, and Sabino Chávez-Cerda. Conical dynamics of Bessel beams. *Optical Engineering*, 46(7):078001–078001, 2007.

[229] Igor A Litvin, Melanie G McLaren, and Andrew Forbes. A conical wave approach to calculating Bessel–Gauss beam reconstruction after complex obstacles. *Optics Communications*, 282(6):1078–1082, 2009.

[230] Z Bouchal. Resistance of nondiffracting vortex beam against amplitude and phase perturbations. *Optics Communications*, 210(3):155–164, 2002.

[231] Halil T Eyyuboğlu. Propagation of higher order Bessel–Gaussian beams in turbulence. *Applied Physics B*, 88(2):259–265, 2007.

[232] Kaicheng Zhu, Shaoxin Li, Ying Tang, Yan Yu, and Huiqin Tang. Study on the propagation parameters of Bessel–Gaussian beams carrying optical vortices through atmospheric turbulence. *Journal of the Optical Society of America A*, 29: 251–257, 2012.

[233] W Nelson, JP Palastro, CC Davis, and P Sprangle. Propagation of Bessel and Airy beams through atmospheric turbulence. *Journal of the Optical Society of America A*, 31(3):603–609, 2014.

[234] Yu Zhu, Xiaojun Liu, Jie Gao, Yixin Zhang, and Fengsheng Zhao. Probability density of the orbital angular momentum mode of Hankel-Bessel beams in an atmospheric turbulence. *Optics Express*, 22(7):7765–7772, 2014.

[235] Philip Birch, Iniabasi Ituen, Rupert Young, and Chris Chatwin. Long-distance Bessel beam propagation through Kolmogorov turbulence. *Journal of the Optical Society of America A*, 32(11):2066–2073, 2015.

[236] Timothy Doster and Abbie T Watnik. Laguerre–Gauss and Bessel–Gauss beams propagation through turbulence: analysis of channel efficiency. *Applied Optics*, 55 (36):10239–10246, 2016.

[237] Nokwazi Mphuthi, Roelf Botha, and Andrew Forbes. Are Bessel beams resilient to aberrations and turbulence? *Journal of the Optical Society of America A*, 35 (6):1021–1027, 2018.

[238] R. Vasilyeu, A. Dudley, N. Khilo, and A. Forbes. Generating superpositions of higher–order Bessel beams. *Optics Express*, 17(26):23389–23395, 2009.

[239] Mohamed A. Mahmoud, Mohamed Y. Shalaby, and Diaa Khalil. Propagation of Bessel beams generated using finite-width durnin ring. *Applied Optics*, 52(2): 256–263, Jan 2013. doi: 10.1364/AO.52.000256.

[240] John H McLeod. The axicon: a new type of optical element. *Journal of the Optical Society of America*, 44(8):592–597, 1954.

[241] R. M. Herman and T. A. Wiggins. Production and uses of diffractionless beams. *Journal of the Optical Society of America A*, 8(6):932–942, Jun 1991. doi: 10.1364/JOSAA.8.000932.

[242] Jochen Arlt and Kishan Dholakia. Generation of high-order Bessel beams by use of an axicon. *Optics Communications*, 177(1-6):297–301, 2000.

[243] Antti Vasara, Jari Turunen, and Ari T Friberg. Realization of general nondiffracting beams with computer-generated holograms. *Journal of the Optical Society of America A*, 6(11):1748–1754, 1989.

[244] Jeffrey A Davis, E Carcole, and Don M Cottrell. Nondiffracting interference patterns generated with programmable spatial light modulators. *Applied Optics*, 35 (4):599–602, 1996.

[245] Jeffrey A Davis, E Carcole, and Don M Cottrell. Intensity and phase measurements of nondiffracting beams generated with a magneto-optic spatial light modulator. *Applied Optics*, 35(4):593–598, 1996.

[246] David Idisi. Vector Bessel beams: generation and detection using digital axicons. *Indian Journal of Physics*, 92(4):513–518, 2018.

[247] Guy Indebetouw. Nondiffracting optical fields: some remarks on their analysis and synthesis. *Journal of the Optical Society of America A*, 6(1):150–152, 1989.

[248] James E Durnin and Joseph H Eberly. Diffraction free arrangement, December 19 1989. US Patent 4,887,885.

[249] K Uehara and H Kikuchi. Generation of nearly diffraction-free laser beams. *Applied Physics B*, 48(2):125–129, 1989.

[250] Pertti Pääkkönen and Jari Turunen. Resonators with Bessel–Gauss modes. *Optics Communications*, 156(4):359–366, 1998.

[251] Anatol N Khilo, Eugeny G Katranji, and Anatol A Ryzhevich. Axicon-based Bessel resonator: analytical description and experiment. *Journal of the Optical Society of America A*, 18(8):1986–1992, 2001.

[252] J Rogel-Salazar, GHC New, and S Chávez-Cerda. Bessel–gauss beam optical resonator. *Optics Communications*, 190(1-6):117–122, 2001.

[253] Igor A Litvin, Nikolai A Khilo, Andrew Forbes, and Vladimir N Belyi. Intra–cavity generation of Bessel–like beams with longitudinally dependent cone angles. *Optics Express*, 18(5):4701–4708, 2010.

[254] AJ Cox and Dean C Dibble. Nondiffracting beam from a spatially filtered Fabry–Perot resonator. *Journal of the Optical Society of America A*, 9(2):282–286, 1992.

[255] SM Dutra and PL Knight. On the generation of Bessel beams by spontaneous emission in a planar micro-cavity. *Optics Communications*, 117(3-4):256–261, 1995.

[256] Julio C Gutiérrez-Vega, Rodolfo Rodrıguez-Masegosa, and Sabino Chávez-Cerda. Bessel–gauss resonator with spherical output mirror: geometrical-and wave-optics analysis. *Journal of the Optical Society of America A*, 20(11):2113–2122, 2003.

[257] Peter Muys and Eefje Vandamme. Direct generation of Bessel beams. *Applied Optics*, 41(30):6375–6379, 2002.

[258] CL Tsangaris, GHC New, and J Rogel-Salazar. Unstable Bessel beam resonator. *Optics Communications*, 223(4-6):233–238, 2003.

[259] A. Dudley, Y. Li, T. Mhlanga, M. Escuti, and A. Forbes. Generating and measuring nondiffracting vector Bessel beams. *Optics Letters*, 38(17):3429–3432, 2013.

[260] Uwe Griebner, Günter Steinmeyer, Gero Stibenz, Martin Bock, Uwe Griebner, and Volker Kebbel. *Self-Reconstruction of Pulsed Optical X-Waves*, pages 299–313. Wiley Online Library, 2 edition, 2008.

[261] David J Richardson. Filling the light pipe. *Science*, 330(6002):327–328, 2010.

[262] DJ Richardson, JM Fini, and LE Nelson. Space-division multiplexing in optical fibres. *Nature Photonics*, 7(5):354, 2013.

[263] S Berdagué and P Facq. Mode division multiplexing in optical fibers. *Applied Optics*, 21(11):1950–1955, 1982.

[264] Giorgia Parca, Ali Shahpari, Valeria Carrozzo, Giorgio Maria Tosi Beleffi, and Antonio LJ Teixeira. Optical wireless transmission at 1.6-Tbit/s (16× 100 Gbit/s) for next-generation convergent urban infrastructures. *Optical Engineering*, 52(11): 116102, 2013.

[265] Shuhui Li, Shi Chen, Chunqing Gao, Alan E Willner, and Jian Wang. Atmospheric turbulence compensation in orbital angular momentum communications: Advances and perspectives. *Optics Communications*, 408:68–81, 2018.

[266] Mitchell A Cox, Ling Cheng, Carmelo Rosales-Guzmán, and Andrew Forbes. Modal diversity for robust free-space optical communications. *Physical Review Applied*, 10(2):024020, 2018.

[267] Igor A Litvin, Thandeka Mhlanga, and Andrew Forbes. Digital generation of shape-invariant Bessel-like beams. *Optics Express*, 23(6):7312–7319, 2015.

[268] I Litvin, L Burger, and A Forbes. Self-healing of Bessel-like beams with longitudinally dependent cone angles. *Journal of Optics*, 17(10):105614, 2015.

[269] Carl Paterson. Atmospheric turbulence and orbital angular momentum of single photons for optical communication. *Physical Review Letters*, 94(15):153901, 2005.

[270] C Gopaul and R Andrews. The effect of atmospheric turbulence on entangled orbital angular momentum states. *New Journal of Physics*, 9(4):94, 2007.

[271] Jaime A Anguita, Mark A Neifeld, and Bane V Vasic. Turbulence-induced channel crosstalk in an orbital angular momentum-multiplexed free-space optical link. *Applied Optics*, 47(13):2414–2429, 2008.

[272] Glenn A Tyler and Robert W Boyd. Influence of atmospheric turbulence on the propagation of quantum states of light carrying orbital angular momentum. *Optics Letters*, 34(2):142–144, 2009.

[273] Zhang Yi-Xin and Cang Ji. Effects of turbulent aberrations on probability distribution of orbital angular momentum for optical communication. *Chinese Physics Letters*, 26(7):074220, 2009.

[274] A Arockia Bazil Raj. *Free space optical communication: system design, modeling, characterization and dealing with turbulence*. Walter de Gruyter GmbH & Co KG, 2016.

[275] Hemani Kaushal and Georges Kaddoum. Optical communication in space: challenges and mitigation techniques. *IEEE Communications Surveys & Tutorials*, 19 (1):57–96, 2017.

[276] Larry C Andrews. Field guide to atmospheric optics, vol. *FG03 of SPIE Field Guides*, 2004.

[277] Lucie Dordová and Otakar Wilfert. Calculation and comparison of turbulence attenuation by different methods. *Radioengineering*, 19(1):162–167, 2010.

[278] Korhan Öztürk. *Simulation of free space optical links under different atmospheric conditions*. PhD thesis, Çankaya University, 2011.

[279] François Roddier. The effects of atmospheric turbulence in optical astronomy. In *Progress in Optics*, volume 19, pages 281–376. Elsevier, 1981.

[280] John J Degnan, Antonios Seas, Howard Donovan, and Thomas Zagwodzki. Slr2000c: An autonomous satellite laser ranging and space-to-ground optical communications facility. In *proceedings of 14th International Workshop on Laser Ranging*, 2004.

[281] Xiaoli Sun, David R Skillman, Evan D Hoffman, Dandan Mao, Jan F McGarry, Gregory A Neumann, Leva McIntire, Ronald S Zellar, Frederic M Davidson, Wai H Fong, et al. Simultaneous laser ranging and communication from an earth-based satellite laser ranging station to the lunar reconnaissance orbiter in lunar orbit.

In *Free-Space Laser Communication and Atmospheric Propagation XXV*, volume 8610, page 861003. International Society for Optics and Photonics, 2013.

[282] Xiaoli Sun, David R Skillman, Evan D Hoffman, Dandan Mao, Jan F McGarry, Leva McIntire, Ronald S Zellar, Frederic M Davidson, Wai H Fong, Michael A Krainak, et al. Free space laser communication experiments from earth to the lunar reconnaissance orbiter in lunar orbit. *Optics Express*, 21(2):1865–1871, 2013.